Development of a Prototype for the Novel Disc DIRC for $\bar{\text{P}}$ANDA

Euan Niall Cowie, MSci

Submitted in fulfilment of the requirements for the Degree of Doctor of Philosophy

School of Physics & Astronomy
College of Science & Engineering

August 2012

Abstract

The $\bar{\text{P}}$ANDA experiment is a planned experiment for the FAIR upgrade to GSI in Darmstadt, Germany. It aims to probe the nature of hadronic matter and the Strong nuclear force to unprecedented levels of accuracy and precision. A general purpose detector, covering 4π solid angle, will reside on the High Energy Storage Ring (HESR) racetrack-type accelerator. The HESR will provide a beam of variable momentum anti-Protons which impinge upon a proton target internal to the $\bar{\text{P}}$ANDA detector.

To fulfil the physics programme the detector will utilise two Čerenkov detectors based on the Detection of Internally Reflection Čerenkov radiation (DIRC) principle, one in a barrel configuration and one in an disc configuration. A proposed design for the disc configuration DIRC is the Focussing Lightguide Disc DIRC (FLDD). In addition to the novel geometry the FLDD proposes to use a unique hardware element to correct for the chromatic dispersion present in DIRC detectors. Lithium Fluoride was selected to correct for this dispersion and was found to reduce the angular spread resulting by a factor of ~ 4.7, in agreement with the predicted reduction.

A full optical simulation of a prototype accurately reproduced all of the features observed at test beam. Therefore to perform the Pion/Kaon separation required for the $\bar{\text{P}}$ANDA physics programme the design needs a detector surface split into 64 channels or a resolution of $0.78125\,mm$ per pixel.

Further study of the focussing lightguide element is required to access the full performance of the FLDD design.

Contents

List of Figures

List of Tables

Acknowledgements

I would like to thank my first supervisor over the course of my Ph.D, Dr. Bjoern Seitz, for his support, guidance and understanding throughout.

I would also like to thank my second supervisor Dr Matthias Hoek who has provided extensive technical support, help and assistance, as well as being a confidant and mentor.

Dr. Tibor Keri provided excellent support in the development and management of electronics systems without which none of the data acquisition presented herein would have been possible.

The Nuclear Physics Group within the School of Physics and Astronomy at the University of Glasgow have provided me with the technical resources required with which to carry out this thesis and to the group technicians, Mr Scott Lumsden and Mr Tony Clarkson, I am eternally grateful.

The STFC has provided me with the opportunity and funded my studies, as well as the travel which a time entails, throughout and without this it would not have been possible to begin, let alone conclude this journey.

Thanks go to my friends and family on who I have lent so heavily in last 4 years, their support has seen me through. This is especially true of my Mother and Father who have never tired of working with me as I struggled with balancing obligations to my work and to my home, and also of my girlfriend Fiona, who has been there to pick me up when I have fallen to my lowest. They showed to me the spirit required within myself to complete such a vast undertaking.

Finally to my pet hamster John, who has tirelessly worked to show me the true meaning of perseverance.

Declaration

I hereby declare that the work contained herein is my own.

Chapter 1

Introduction

The frontiers of physics are being simultaneously pushed to higher energies and new discoveries, leading to greater understanding of our physical universe. This is a challenge which requires the development of novel detectors and the use of novel technologies to successfully achieve.

An active branch of modern physics is the research into hadronic matter, any matter which interacts with the Strong force. Our understanding of hadronic matter is vital to our understanding of the material universe as it forms both the constituents of the atomic nucleus and the constituents of the nucleons themselves, quarks. Only through a complete knowledge of these constituents and the force which governs their interaction can we fully understand the universe.

The study of such a complex field requires advanced technology and detector systems to achieve the accuracy and precision required to further our understanding. One such experiment will be the $\bar{\text{P}}$ANDA detector, to be situated on the High Energy Storage Ring (HESR) at the Facility for Anti-proton and Ion Research (FAIR) upgrade to the GSI facility near Darmstadt, Germany.

A variable momentum beam of cooled anti-protons will impinge on a proton target and the resultant products will be detected by a general purpose detector with near-4π solid angle coverage. $\bar{\text{P}}$ANDA will centre on excellent calorimetry complemented by state-of-the-art tracking. Particle Identification (PID) is required to cover a large dynamic range and have excellent identification capabilities.

To this end the novel Focussing Lightguide Disc Čerenkov detector, based on the Detection of Internally Reflected Čerenkov (DIRC) principle, is proposed to be situated within the end-cap of the $\bar{\text{P}}$ANDA detector. The development and understanding of the prototype for this detector will be presented in detail in this thesis.

1.1 Physics Motivation

The nuclear force, known now to be the residual long-range component of the Strong force, was postulated as a mechanism to overcome the electromagnetic repulsion between bound protons in the nucleus, allowing the formation of nuclei beyond hydrogen. Hideki Yukawa (1935) postulated a carrier particle to mediate this force and named them Mesons, from the Greek *mesos* meaning *intermediate* as it was predicted to have a

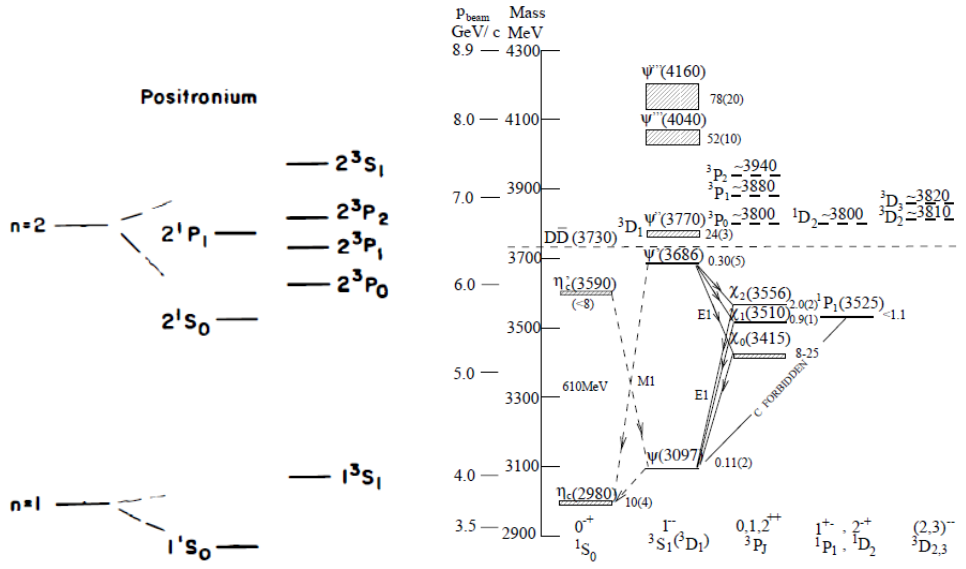

(a) Positronium energy levels. [6] (b) Charmonium energy levels. [7]

Figure 1.1: A comparison between energy levels of Positronium and Charmonium. Striking similarities such as the $^3P_{0,1,2}$ triplet state, the $^1P_1$ state being finely split from the triplet states and the structure of the S-states. These similarities lead to the hypothesis that Charmonium was a particle-antiparticle pair.

rest mass between that of the electron and proton.

The Pion was the first Strong force interacting particle discovered to display the properties required of Yukawa's meson and was subsequently found to be the primary carrier of the nuclear residual component of the Strong force. Subsequent to it's discovery a great many hadrons, particles participating in Strong force interactions, were discovered and catalogued and this lead to the development of a new model of classification of these hadrons in terms of small sub-components, known as quarks.

Every observed hadron was comprised of valence quarks, which together contribute the quantum numbers of the observed hadron. Mesons, such as the pion, comprise a quark-antiquark pair whereas Baryons, such as the proton, and anti-baryons, such as anti-protons, comprise three quarks or three antiquarks respectively. Strong evidence for the constituent-based model of hadrons can be found when looking at the energy level systems of heavy quark-antiquark pairs, Figure 1.1.

1.1.1 Charmonium

Quarkonia are meson states comprising pairs of a single quark flavour, such as the J/ψ or Υ states which consist of $c\bar{c}$ and $b\bar{b}$ respectively. The first of these very massive meson states was discovered in 1974 simultaneously at the Stanford Linear Accelerator [2] and Brookhaven National Laboratory [3] through different reaction channels:

$$e^+e^- \rightarrow \psi \rightarrow l^+l^- + \text{hadrons} \tag{1.1.1}$$

$$p + \mathrm{Be} \rightarrow J/\psi \rightarrow e^+e^- + \mathrm{other} \tag{1.1.2}$$

respectively.

Reconstructing both the centre of mass energy for the e^+e^- annihilation at SLAC and the invariant mass distribution of the e^+e^- products at BNL showed a sharp resonance at $3.1\,GeV$. This new state, named J/ψ, has been shown to have a width of only $92.9\,keV$. When compared with the resonances of mesons comprising the three lightest quark flavours, which typically have widths of order $1 - 10\,MeV$ [4], the narrowness of the J/ψ resonance was highly anomalous. This indicated that it could not be explained in terms of these three light quarks, the only quarks discovered to that point.

A new quark, carrying a new Charm quantum number, had been postulated prior to the discovery of the J/ψ to answer a separate problem regarding the non-existence of strangeness-changing neutral weak currents, i.e. interactions mediated by the electric charge-less Z^0 boson [5]. It was postulated that the J/ψ state was comprised of a $c\bar{c}$ pair. Comparison of the energy levels of the ψ and e^+e^- pair, Figure 1.1, at different J^{PC} shows clear similarities in structure, such as the appearance of a triplet state at ${}^3P_{0,1,2}{}^1$ corresponding to $J^{PC} = 0^{++}, 1^{++}, 2^{++}$. This triplet structure is also clear when the energy levels of the Υ were studied, implying it too is a composite particle comprising a fermion-antifermion pair. The J/ψ was therefore found to be a charm-anticharm *c barc* quark pair.

The Strong force is best studied in its simplest manifestations and Mesons like J/ψ are such systems. Charmonium, the generalised name for all $c\bar{c}$ states including J/ψ, is a meson system presenting attractive features for the study of the Strong force. First of these is its simplicity as a two-body system comprising a quark-antiquark pair of the same flavour. Second is the increase mass of the Charm quark relative to the Up, Down and Strange quarks. The mesons constructed of these lightest three flavours occupy a densely populated spectrum of mesons with up to 77 mesons expected in the mass region $1.5 - 2.5\,GeV$ each with widths in the order of $100s\,MeV$ [4]. The lightness of these quarks requires any theoretical treatment include relativistic effects and this results in a Strong coupling constant too large for perturbation theory to be used. Charmonium avoids both of these issues as the mass region $2.9 - 3.7\,GeV$ contains only 8 narrow, isolated Charmonium states, Figure 1.1(b), and due to the mass of the Charm quark the relativistic considerations of $c\bar{c}$ result in fewer Strong coupling problems. Third is that the Charmonium mass spectrum requires much lower E_{cms} for any detector system to access, when compared to the otherwise similarly beneficial Bottomonium, $b\bar{b}$ states such as Υ.

Above $3.7\,GeV$ further excited Charmonium states are both predicted and discovered though many unanswered questions remain, indicated by dashed lines in Figure 1.1(b). These additional states occur in a mass range above the $D\bar{D}$ production threshold. The D mesons comprise a Charm paired with and Up, Down or Strange quarks and have masses ranging from $1.867\,GeV$ to $2.573\,GeV$ and in meson-antimeson pairs have masses $> 3.7\,GeV$ [4]. These mesons obscure the Charmonium states above this mass so making the region less suited to precise study, the widths of these states are a factor of some $10\,eV$ to $10^3\,eV$ greater than those of the narrow resonances below $3.7\,GeV$ [7].

[1] Convention in Nuclear physics labels lowest energy P-states as 1P, Atomic physics, used for positronium, labels these as 2P.

Within the states below the $D\bar{D}$ threshold the singlet states $\eta_c(1S)$, $h_c(1P)$ and $\eta_c(2S)$ have the greatest uncertainty on the mass, sometimes of $> 1.0\,MeV$ [7]. Recent results from the BESIII collaboration reduce the uncertainty on $M_{h_c} \pm 0.13 \pm 0.18\,MeV$ [8]. Further limitations on the uncertainty of both the mass and width of the two η_c states will be of importance in continuing the improvement of QCD models. The prediction of the $h_c(1P)$ state, with a mass of $M_h \approx 3.525\,GeV$, was confirmed by its unambiguous discovery in 2005 [9]. Lattice QCD models predicted the hyperfine splitting between the h_c and the centroid of $\chi_c(3P)$ masses of $1.5\,MeV \leq \Delta M_{hf} \leq 3.7\,MeV$. Experimentally this was found to be $\Delta M_{hf} = 1.0 \pm 0.6 \pm 0.4\,MeV$, in agreement with theoretical prediction.

Perhaps most interesting amongst the states above the $D\bar{D}$ threshold are the so-called X, Y and Z states, observed by BELLE in 2005 [10]. These states were not observed to decay into channels predicted for excited states of the χ_{cJ}, which are predicted to decay into $D\bar{D}$ pairs. The $Z(3931)$ is tentatively identified as the excited charmonium state $\chi_{c2}(2^3P_2)$ as it agrees with predictions on mass, angular distribution of decay products and Branching ratio into $D\bar{D}$ pairs. This and many other states lying above the $D\bar{D}$ threshold are not confirmed and many of their quantum numbers are unknown. $\bar{\text{P}}$ANDA will be in an excellent position to study these states and to pin down these unknowns [1].

The study of the Charmonium spectrum gives an excellent insight into the behaviour of QCD and the successes of its simple potential model. Key topographical features such as the mass and width of the η_c state, the structure of the χ_c triplet states, the hyperfine mass splitting of the χ_c states and the h_c state and the radial excitations of the η_c and J/ψ are all clean tests of QCD model below the $D\bar{D}$ threshold. Above the threshold almost all states have questions still attached to them and any greater study of these can only improve our knowledge of this energy regime.

1.1.2 Exotic Excitations

It is predicted that the gluon "flux tube" connecting hadrons together can be excited. Doing so increases the number of degrees of freedom in the $q\bar{q}$ system. This increase may be manifest in its contribution to the quantum numbers of the observed system. In some cases the quantum numbers of the gluon, $J^P = 1^+$ or 1^-, added to those of the existing Quarkonium state will produce exotic excitations with J^{PC} states which are not possible for a simple $q\bar{q}$ system [1]. An outline of the spectrum of these exotics is shown with observed $c\bar{c}$ states in Figure 1.2.

Several light, unflavoured mesons with exotic quantum numbers have been observed by E852 [11–14] at Brookhaven National Laboratory and Crystal Barrel [15–18] at the LEAR accelerator in CERN. The initial observations of these states indicated that these states were the $\pi_1(1400)$ and its excited $\pi_1(1600)$ state. As the nomenclature implies these states carry $J = 1$ and are exotic as they have $PC = -+$, a combination not formed by a $q\bar{q}$ pair. The E852 experiment also reported seeing a candidate for the $\pi_1(2000)$ state [13, 14] carrying the same J^{PC} as the lower energy π_1 states. These states require extensive further studies but the potential successful identifications of hybrid unflavoured states indicates that looking for such hybrid states in Charmonium region is a worthwhile undertaking.

In the Charm sector there are hybrid states predicted with $J^{PC} = 1^{-+}$ and masses in the range $4.287\,GeV \leq$

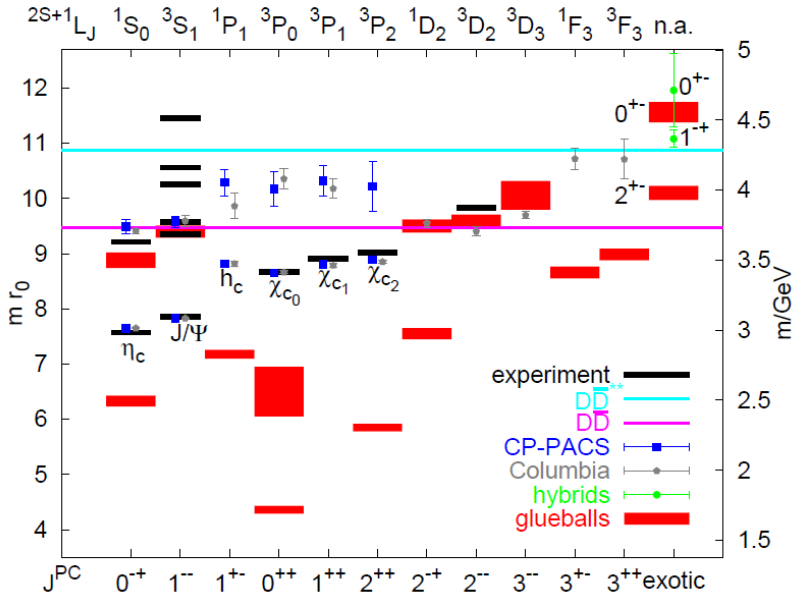

Figure 1.2: The energy levels, J^{PC} quantum numbers and spectroscopic labels of discovered Charmonium states and predicted Charmonium states, glueballs and hybrid states within the energy range for which $\bar{\text{P}}$ANDA is designed [1].

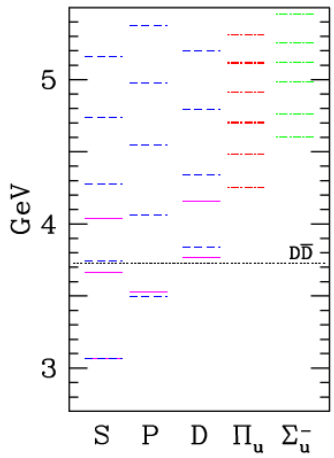

Figure 1.3: The energy level spectrum of charmonium showing conventional states, S, P and D, and predicted Hybrid states, Π_u and Σ_u^- [19].

$m(c\bar{c}g) \leq 4.390\,GeV$ [20–23], see Figure 1.3. These states are believed to be the lowest lying hybrid charmonium states, tentatively named $\tilde{\eta}_{c1}$, and occur above the $D\bar{D}$ threshold. In this region, as previously discussed in Section 1.1.1, there are predicted to be many states with varying masses and widths. The exotic quantum numbers of the $\tilde{\eta}_{c1}$ state allow for initial separation from other states in the open-charm energy region. Successful identification of charmed hybrid states would be a clear success in the current QCD models [1].

Another type of Exotic Excitation predicted by Lattice QCD models is the glueball, a state arising from gluon self-coupling, Figure 1.4. The study of glueballs is strongly linked to knowledge of the QCD vacuum and study of the states consequently impacts upon the vacuum. The masses of the glueball states are predicted

to lie between $1.730\,GeV$ and $4.740\,GeV$ [24] placing them in a similar range to the Charmonium spectrum discussed in Section 1.1.1. Experiments at LEAR [25–29] have previous attempted to find glueballs but have not managed to unambiguously identify any state. Both a successful identification or a failure to identify any glueball states will have a profound impact on our understanding of QCD and how matter is constructed.

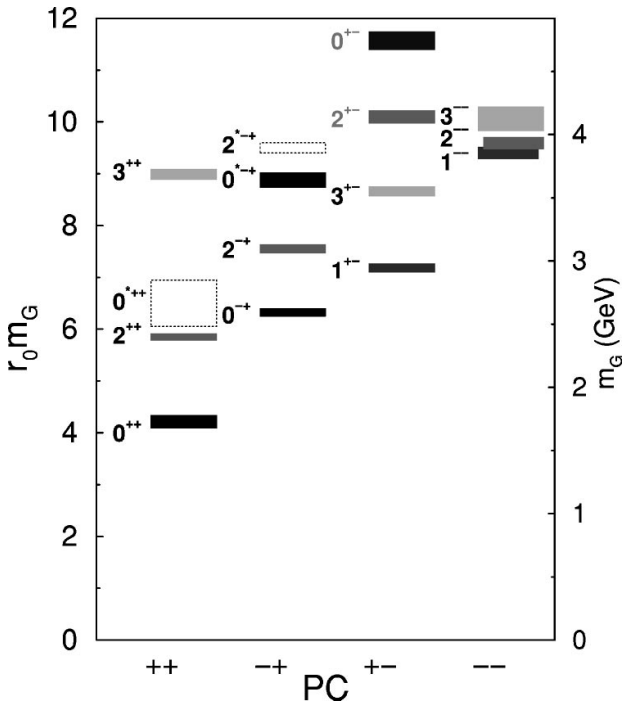

Figure 1.4: The energy levels and J^{PC} of predicted glueball states. [24]

1.1.3 $\bar{\text{P}}$ANDA Benchmark Channels

The key to all modern physics is fluid translation from theory to experiment. All of the physically interesting states in Sections 1.1.1 and 1.1.2 will decay a short time after production, the mean lifetime of J/ψ is of order $\tau \sim 10^{-20}\,s$, and so will not reach the $\bar{\text{P}}$ANDA detector system before decaying. Each state can potentially decay in to dozens of decay channels, some of which will contain a large background obscuring the desired reaction from clear study. The $\bar{\text{P}}$ANDA collaboration therefore looked to key, Benchmark, channels for their physics programme. The physics case for $\bar{\text{P}}$ANDA presents simulated studies of detector performance based on these channels [1].

Charmonium

Background from other hadronic particles is the primary background in Charmonium spectroscopy. Identification of channels which have reduced background is imperative to ensure a clean performance evaluation and the correct identification of Charmonium states. The $\bar{\text{P}}$ANDA collaboration categorised the decays of Charmonium into 4 classes: those with J/ψ in the final state; two- and three-photon decays; light hadron decays; and decays in to $D\bar{D}$ states.

Decays with a final state J/ψ: The benchmark channels for this class of decays have been focussed around

the detection of the decay $J/\psi \to e^+e^-$. The additional particles that will be detected by $\bar{\text{P}}$ANDA include π and γ, for example in the decays channels $p\bar{p} \to J/\psi\pi^+\pi^- \to e^+e^-\pi^+\pi^-$ and $p\bar{p} \to J/\psi\pi^0\pi^0 \to e^+e^-\gamma\gamma\gamma\gamma$. The positive identification of the decay particles, both charged and neutral, is crucial to performance for this decay class.

Two- and Three-Photon decays: The multi-photon decay class arises from the desire to study the $h_c(1P)$ state for reasons outline in Section 1.1.1. The initial observation of this state was carried out on the channel $p\bar{p} \to \pi^0 h_c \to \gamma\gamma\gamma\eta_c$, an electromagnetic decay from the excited h_c state. The initial Charmonium decay within this channel is $h_c \to \gamma\eta_c \to 3\gamma$ requiring the accurate identification and reconstruction of the multi-photon decay products.

Decays to light hadrons: The same initial $p\bar{p} \to h_c \to \gamma\eta_c$ decay can result in the hadronic decay $\eta_c \to \phi\phi \to 2(K^+K^-)$. This channel is an example of Charmonium states decaying into light hadronic states, which are readily produced in $p\bar{p}$ reactions. The direct production of $2(K^+K^-)$ pairs or of a single 2ϕ pair, along with a π^0, is considered primary amongst the background for this channel. The failure to identify the π^0 state by missing one of its 2γ decay products would produce the same detectable decay products as the desired reaction. Complete identification of all neutral particles, as well as the charged Kaons, should therefore obtained.

Decays into $D\bar{D}$: Two channels above the $D\bar{D}$ were benchmarked, the $p\bar{p} \to D^+D^- \to K^-\pi^+\pi^+ + c.c.$ and $p\bar{p} \to D^{*+}D^{*-} \to D^0\pi^+ + c.c. \to K^-\pi^+\pi^+ + c.c.$ channels. The simulated production energy for the $D\bar{D}$ pairs were $3.770\,GeV$ for D^+D^-, corresponding to the $\psi(3770)$ state, and $4.040\,GeV$ for the similar D^* pair. These channels both end in the production of charged light hadron states and background channels with 6 charged hadrons, kinematically similar to the $D\bar{D}$ pair decays, were also studied. Any precise study of these channels and suppression of the background events requires accurate identification of the decay products, knowledge of their momentum and energies.

Exotic Excitations

As $\bar{\text{P}}$ANDA uses an anti-proton beam impinging on a proton target and thus can directly access a full range of J^{PC} via $p\bar{p} \to XY$. This allows direct production of every hybrid and glueball state should they exist within the energy range accessible. The hybrid states of Charmonium, $c\bar{c}g$, encounter similar problems with hadronic background as the pure $c\bar{c}$ states. Glueballs, should they exist, will also have hadronic decay modes and be located over a similar energy range adding to the background.

The benchmark channel for the $\tilde{\eta}_{c1}$ hybrid state, identifiable as it has exotic $J^{PC} = 1^{-+}$, is $p\bar{p} \to \tilde{\eta}_{c1}\eta \to \chi_{c1}\pi^0\pi^0\eta$. The primary pollution for this channel is expected to be the uncertainty over direct or decay production of the final state. Other Charmonium states, such as the J/ψ, are also expected to contribute to this contamination. Identification will centre on reconstructing the invariant mass of candidate photons and accepting pairs with masses near the π^0 and η. Identification of the J/ψ using its decay e^+e^- pair, in combination with a photon not accounted for in the reconstructions of the π^0 and η, will give χ_{c1} candidates and it is then combined with the previous identifications to create candidate $\chi_{c1}\pi^0\pi^0\eta$ states. Through this careful analysis procedure it is possible to place selection criteria upon each stage of the final state

reconstruction such that it recombines to the $\tilde{\eta}_{c1}\eta$ initial state.

The $\tilde{\eta}_{c1}$ state lies above the $D\bar{D}$ threshold and as such decays into open-charm topologies are possible. The benchmark amongst these is $p\bar{p} \to \tilde{\eta}_{c1}\eta \to DD^*\eta$. Direct production of either $D\bar{D}^{*0}$ with either π^0 or η contributes to the primary background. Using the same photon invariant mass method as for the χ_{c1} decay above the π^0 and η can be reconstructed. The decay $D^0 \to K^-\pi^+\pi^0\pi^0$ will be present either from directly produced D^0 or from $\tilde{\eta}_{c1} \to D\bar{D}^*\eta$ and the invariant mass of the K and π state is constructed to give the originating $D\bar{D}^*$ pair. The final state here requires clear neutral particle identification for the decay product photons, but it also requires unambiguous charged particle separation for the $K^-\pi^+$ and conjugate states present in the detector.

1.2 The High Energy Storage Ring and $\bar{\text{P}}$ANDA Detector

The $\bar{\text{P}}$ANDA detector is required to have excellent capabilities in detection of all decay products and their properties if it is to realise the physics programme outlined in Section 1.1. The detector must provide accuracy and precision in locating decay vertices, in tracking particle trajectories, in the identification of charged and neutral particles and in measuring the energy and momentum of these decay products. Alone, however, these facets will not enable the realisation of the physics programme, and the provision of a beam of antiprotons by the High Energy Storage Ring (HESR), with an accurate and precise control over the beam momentum, is critical to the success of the experiment.

1.2.1 The HESR

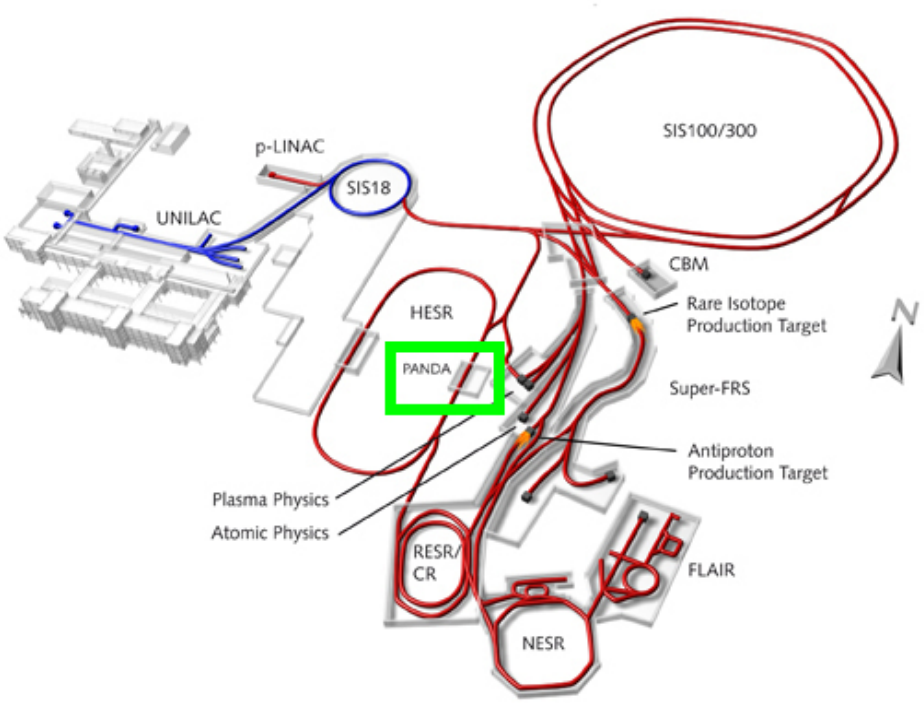

Figure 1.5: An overview of the proposed FAIR facility at GSI. The location of $\bar{\text{P}}$ANDA is highlighted.

The HESR will be one of the accelerators situated at the FAIR upgrade to GSI in Darmstadt, Germany, Figure 1.5. The accelerator will be a racetrack-type configuration with two long straight sections, housing the $\bar{\text{P}}$ANDA detector on one and the cooling systems on the other, Figure 1.6. The accelerator is designed to run in two modes, High Luminosity and High Precision, the challenge for the former being luminosities of up to $10^{32}\,cm^{-2}\,s^{-1}$ and for the latter a momentum spread in the order of $\sigma_p/p \leq 10^{-5}$. A summary of the required experimental parameters is given in Table 1.1.

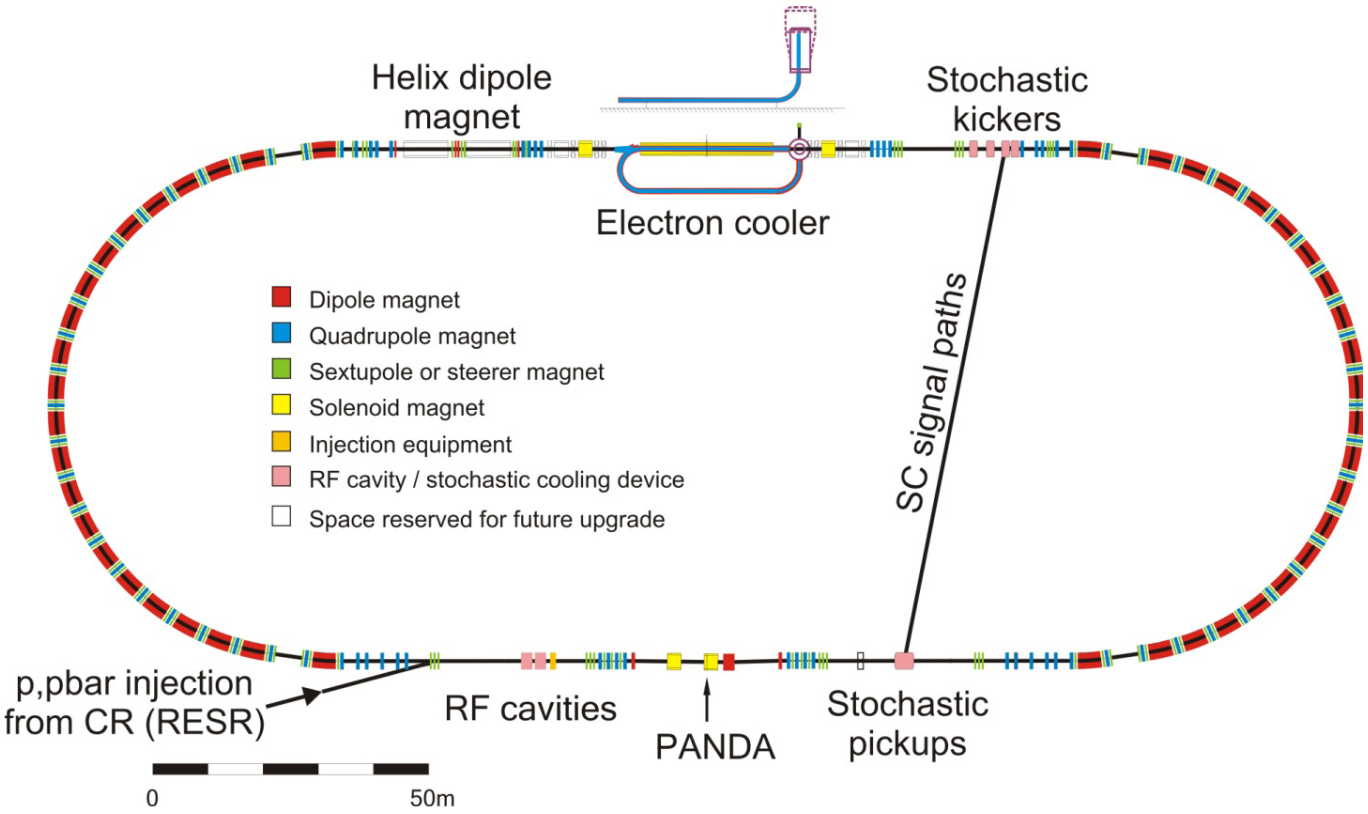

Figure 1.6: Schematic of the High Energy Storage Ring with the positions of the $\bar{\text{P}}$ANDA detector, electron cooler, bending and steering magnets.

The two operational modes will allow $\bar{\text{P}}$ANDA to both produced rare events, running in High Luminosity (HL) mode, and also to undertake fine resonance scans, using High Resolution (HR) mode. The former will be beneficial to the study of glueballs and other low yield states; the latter is of greatest use in the precision Charmonium spectroscopy that will form the backbone of the $\bar{\text{P}}$ANDA physics programme. The electron cooler is postponed until a future upgrade limiting the performance of the HR mode initially. The development of the HESR is considered to be on pace for construction within the FAIR schedule [30].

1.2.2 The $\bar{\text{P}}$ANDA Detector

The $\bar{\text{P}}$ANDA detector, Figure 1.7, will be constructed in two separate spectrometers [1]. The Target Spectrometer (TS), Figure 1.8, is furthest upstream of the two and contains the $\bar{\text{P}}$ANDA internal target. It is an asymmetric detector to account for the target interaction kinematics. It forms a complete spectrometer system with a Micro Vertex detector (MVD) - detecting the primary decay vertex, Tracking detectors -

Table 1.1: Summary table of the experimental requirements for the HESR and an overview of its two operational modes.

Experimental Requirements		
Species	Antiproton	
Mean Interaction Rate	20 MHz	
Operation Modes	High Resolution (HR)	High Luminosity (HL)
Luminosity	$2 \times 10^{31}\, cm^{-2}\, s^{-1}$	$2 \times 10^{32}\, cm^{-2}\, s^{-1}$
Particles per Bunch	10^{10}	10^{11}
RMS Momentum Spread	$\sigma_p/p \leq 2 \times 10^{-5}$	$\sigma_p/p \sim 10^{-4}$
Momentum Range	$1.5\,GeV/c$ - $9\,GeV/c$ with electron cooling.	$1.5\,GeV/c$ - $15\,GeV/c$ with stochastic cooling.

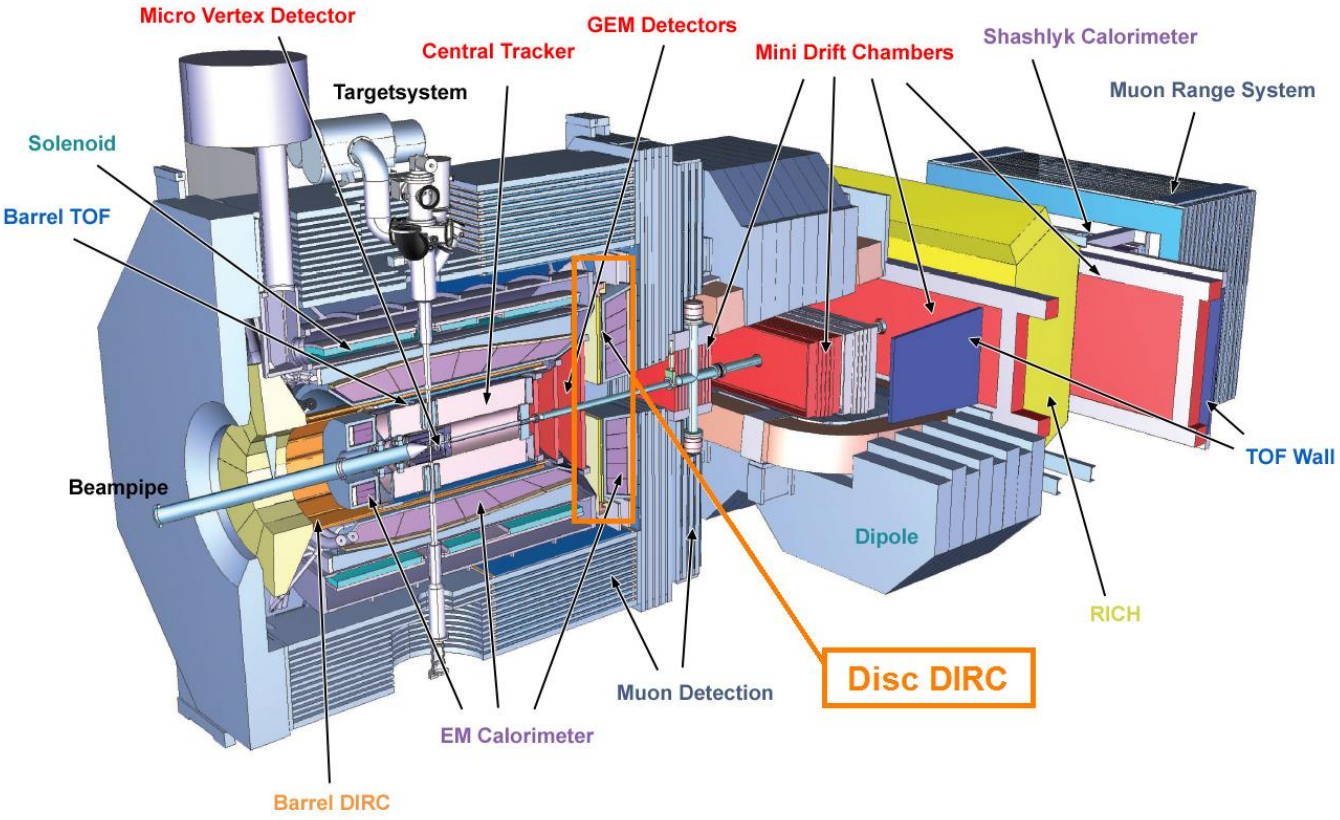

Figure 1.7: A CAD render of the full $\bar{\text{P}}$ANDA detector. The Disc DIRC, contained within the Target Spectrometer is highlighted. The beam enters through the beampipe from left to right [1].

measuring the flight path if charge particles, Particle Identification detectors (PID) - to discriminate between particle species, Electromagnetic Calorimeters (EMC) - to measure particle and photon energy, muon detectors - to distinguish muon tracks from others and a solenoid magnet - to allow measurement of charge particle momentum. It can be broadly split into two subsections, the Barrel and the Endcap covering $\theta \geq 22°$ and $5° \leq \theta \leq 22°$ in polar angle respectively. It is in the Endcap that the Focussing Lightguide Disc DIRC (FLDD) will be located.

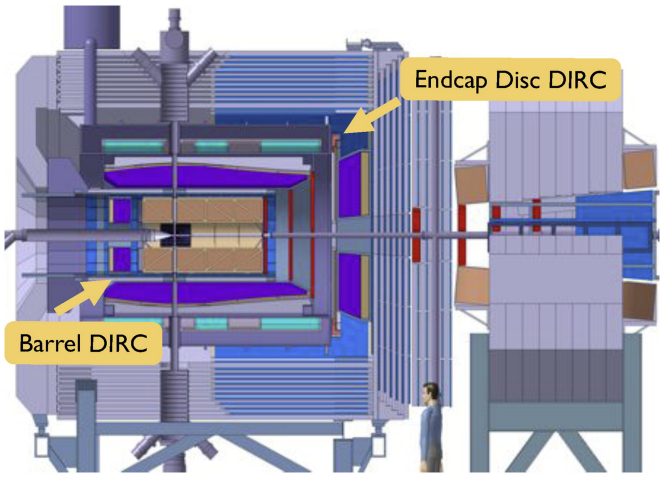

Figure 1.8: The Target Spectrometer. The beam enters from the left. Highlighted are both the Barrel DIRC and the FLDD. The EMCs are shown in purple, the GEM trackers in red, the central tracker is in beige and the MVD is in black [1].

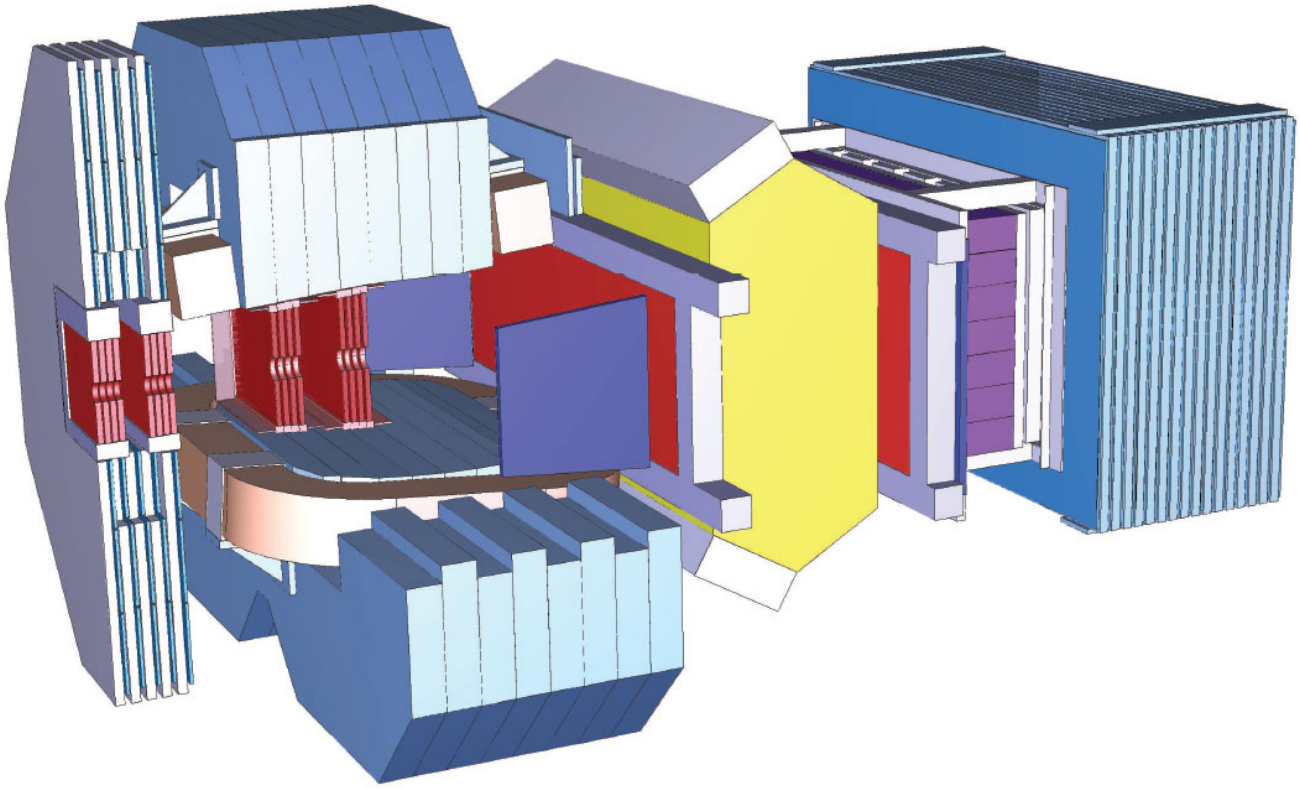

Figure 1.9: The Forward Spectrometer. Secondary particles produced at the Interaction Point enter from the left. Tracking is highlighted in red, the magnet in blue, PID in yellow and the EMC in purple. Tracking consists of a system of GEM-foil trackers organised in sets located before and after the dipole magnet and also within the magnet opening [1].

The second section is the Forward Spectrometer (FS), Figure 1.9, which is located downstream of the TS Endcap. The system covers $\theta \leq 5°/10°$ in polar angle with the asymmetry introduced by the dipole magnet. It shares the Micro Vertex detector and sections of the TS Endcap Tracking detector, but also includes

Tracking, Particle Identification, Electromagnetic Calorimetry and muon detection within its set-up. The highest momentum particles, which will have the greatest Lorentz boost in the downstream direction, will be detected in the FS.

The $\bar{\text{P}}$ANDA system will not use central trigger, but will distribute time information to each subsystem individually where it will then be encoded with the detected events. Offline reconstruction can use this time information to associate events from each subsystem appropriately.

The beam will enter the $\bar{\text{P}}$ANDA detector and strike the Internal Target, located within the TS section of the detector system [31]. The current leading design for the target is a cluster-jet target where cooled gaseous hydrogen is forced through a nozzle and is ejected at speed, causing it to cool and cluster in to bunches of between 10^3 and 10^5 atoms. Studies into the optimum combination of experimental conditions for this target have been conducted and it is believed this system will produce a target which matches the $\bar{\text{P}}$ANDA experimental requirements.

An alternative target system is the creation of frozen pellets. This system comes with two primary strengths. First in producing high effective thickness of target and second it allows for an accurate monitoring of the position of the target within the Interaction Point, limiting uncertainties in production position. However the discrete nature of the pellets can cause wide variations from pellet to pellet and so a high variability in interaction rate.

Charged particle tracking is vital to any modern particle detector system. The first stage of the $\bar{\text{P}}$ANDA tracking system will be the Micro Vertex Detector (MVD) [32]. It is designed to sit close to the Interaction Point (IP) and provide 3D spatial information immediately after the primary reaction has taken place. Additionally the initial tracking measurements will aid in the momentum reconstruction for all charge particles, which in turn will aid all PID.

The MVD will consist of barrel and endcap-type sections with the inner layers being silicon pixel detectors and the outer layers being silicon micro strip detectors. It will cover between 3° and 150° in polar angle, θ_p, which is most of the geometric acceptance of the complete $\bar{\text{P}}$ANDA detector. The system is designed such that there a minimum of 4 measured track points within the detector, spanning a maximum of 150 mm radially from the centre of the cylindrical design and 230 mm downstream from the IP.

The second level of tracking is provided by a Straw Tube Tracker (STT) [33]. Operating similarly to a ionization chamber tracking detector in that they measure the time of arrival of ionised electrons to determine the distance of closest approach to the anode wire within each tube. As with the tracking from the MVD that from the STT is required for momentum measurements. The track information also allows for subsequent positive identification of particles in other detectors. The Particle Identification power of the two Čerenkov detectors relies heavily on knowing the trajectory of the traversing particles to resolve the combined Čerenkov and particle angle.

The STT will be in a barrel like configuration and cover $10° \leq \theta_p \leq 140°$. The radial cross-section will be hexagonal and the only blind spot is caused by the target pipe. The inner portion of the STT will have straws aligned parallel to the beam direction, extending in z. There will then be layers of straws offset by

$+2.9°$ and $-2.9°$ to the parallel, followed by a final section of z-aligned tubes. Straw tubes only measure distance of closest approach to the anode wire running within the tube, therefore angularly offset layers are required to resolve z-coordinates in tracking.

In the direction of the beam the same role is performed by a set of GEM-foil trackers [34]. The detectors will cover $\theta_p \leq 22°$ and will be placed and $1.1\,m$, $1.4\,m$ and $1.9\,m$ downstream of the IP. These detectors will see a high particle flux, upwards of $1 \times 10^4\,cm^{-2}\,s^{-1}$ and operate in high magnetic fields of up to $2\,T$.

These tracking detectors are all located within the Target Spectrometer which is housed within a solenoid magnetic field, the central axis of the magnet running parallel along the beam line [35]. The field strength in this central region will be $2\,T$ and the internal bore will measure $1.9\,m$. The uniformity of the field strength within the tracking region of the detector, from the IP to the end of the STT and GEM trackers, is designed to be $\pm 1.6\%$ and give a bending power of $1\,Tm$ within the tracking region. Within the endcap region the field strength will decrease.

Particles with a the highest momentum will be preferentially produced at the lowest θ_p and will pass through the TS into the Forward Spectrometer (FS). The tracking within the FS will be carried out by a set of wire chambers placed in 3 pairs, the first pair in front of a dipole magnet, the second within the magnet and the final set downstream of the magnet. The design of these detectors is foreseen to have 3 pairs of detection planes per element, 1 with vertical wires and 2 with wires offset by $\pm 10°$ to give the z coordinate. The momentum resolution of this system is expected to be $\Delta p/p = 0.2\%$, limited by the scattering induced by the detector system.

The magnetic field used for momentum measurements within the FS will be provided by a superconducting Dipole magnet [35]. It will provide a bending power of $2\,Tm$ when the beam momentum is $p_{beam} = 15\,GeV/c$ and has an acceptance of between $0°$ and $5°$ in the vertical and $10°$ in the horizontal. The bending power will be variable in association with p_{beam}, starting at $0.2\,Tm$ for $p_{beam} = 1.5\,GeV/c$. Particles with a momenta which is a factor of 15 less than p_{beam} will be undergo a strong enough deflection that they will not traverse the full field produced by the dipole. The uncertainty in momentum reconstruction introduced by the reduced field integral is offset in part by the increase deviation these particles undergo.

Reconstructing the energy of the final state from their decay products is critical to the performance of any particle detector like the $\bar{\text{P}}$ANDA detector. Electromagnetic Calorimeters (EMCs) will be used for both the TS and FS sections of the detector and are required to cover a large range of energies, from a few MeV up to a few GeV per particle. Reconstruction of di-lepton and multi-photon channels is central to the physics programme and only an EMC can access these channels. They will be the outermost layer of the $\bar{\text{P}}$ANDA system and requires detectors inside them to minimise radiation length and therefore the energy deposition in each section.

The Target Spectrometer EMC system will consist of a barrel and an endcap section both functioning independently [36]. Such a large energy range requires special consideration to be given to ensuring a sufficient light yield at the lowest energies. Lead Tungstate (PWO) crystals will be used and cooled to $-25°C$ in order to increase yield at lower energy scales. The barrel section will consist of 11,360, $200\,mm$ crystals and cover the majority of the angular coverage of the $\bar{\text{P}}$ANDA detector. Backwards from the IP will be a 592 crystal

cluster, part of the barrel system, ensuring close to 4π solid angle coverage. The endcap EMC will consist of 3600 crystal and have to cover a much larger particle flux than the barrel system. It is in front of this endcap EMC that the Focussing Lightguide Disc Čerenkov detector will be positioned.

Calorimetry in the Forward Spectrometer will be handled with the Forward Sampling Calorimeter [37]. It consists of alternating layers of heavy absorber material, lead, and active scintillator material, PWO as above. The ratio of absorber thickness to scintillator thickness is a vital step in the design of a sampling calorimeter. A design favouring absorber material will produce a shower of particles with a very narrow Moliere radius whereas a design favouring scintillator material will result in a greater energy resolution. The design will utilise lead plates with a thickness of $275\,\mu m$ and scintillator crystals with a thickness of $1.5\,mm$ in cells of $5.5. \times 5.5\,cm^2$.

A system of muon detectors, based on the range system technique, will be placed as the furthest system from the IP in each of the Barrel, Endcap and FS sections. The system will be placed within the iron yoke of the TS solenoid magnet for the Barrel and Endcap and will be placed beyond the FS EMC. The use of layers of iron as absorber is intended to aid in separation of muon tracks from those of low momentum pions, the further through the system a particle travels the greater the likelihood of it being identified as a muon. Using Mini-Drift Tubes, a miniaturised version of ionization chambers, a two coordinate measurement of particle track is obtained for each instrument stage. The third dimension is obtained from the layer of detector fired. Accurate track reconstruction, combined with information from the other tracking detectors, will allow for separation of secondary decay muons from the primary decays being studied.

The final stage in reconstruction of the final state of any reaction is positive charged particle identification. $\bar{\text{P}}$ANDA will utilise three PID detector systems to achieve PID: a barrel Čerenkov detector based on the successful BaBar Barrel DIRC design; an endcap disc-shaped detector based on the same DIRC principle and a Time-of-Flight (ToF) detector. The design of these detectors will be discussed in Section 1.3.

1.3 Particle Identification and the Focussing Lightguide Disc DIRC

Particle Identification (PID) is one of the central features of every high energy physics detector. The correct, positive identification of the species of particle responsible for tracks within the tracking detectors and clusters within the calorimeters is a basic requirement of any such detectors. Sub-detectors designed specifically to contribute accurate PID to a detector do so typically by measuring the velocity of the traversing particle, using Time-of-Flight or electromagnetic effects to ascertain it. Tracking detectors can contribute to PID by measuring energy deposition with respect to the distance traversed within the detector, abbreviated to dE/dx. $\bar{\text{P}}$ANDA will have three PID specific detectors, a forward Time-of-Flight detector in the Forward Spectrometer (FS) and a pair of Čerenkov detectors utilising the Detection of Internally Reflected Čerenkov (DIRC) radiation principle, a barrel DIRC and an endcap Disc DIRC in the Target Spectrometer (TS).

1.3.1 The Čerenkov Effect

The Čerenkov effect is the emission of electromagnetic radiation caused when an electrically charged particle traverses a dielectric medium with a velocity greater than the phase velocity of light in the medium, described by the Refractive Index of the medium $n = c/v_p$. The particle creates a disturbance, which builds up and is discharged in an electromagnetic shockwave, similarly to a Sonic Boom of aircraft exceeding the speed of sound. It is named for Pavel Čerenkov who was the first person to rigorously categorise the effect [39].

The shockwave is emitted with a conical wavefront relative to the path of the particle causing the disturbance. The emitted photons are polarised radially outward from the particle path. The opening half-angle of the cone is called the Čerenkov angle, θ_c, and is govern by the relation:

$$\cos\theta_c = \frac{1}{n_p(\lambda)\beta} \tag{1.3.1}$$

The Čerenkov angle varies with n_p, the Refractive Index of phase of the medium in which the effect takes place, and the the velocity of the particle $\beta = v/c$. It is clear that $\cos\theta_c = 1$ at threshold and so light is produced along the particle trajectory at $\beta = \beta_t$. As $\beta \to 1$, $\cos\theta_c \to 1/n_p(\lambda)$ which gives the maximum Čerenkov angle for a given medium.

The frequency dependence of the production of photons by the Čerenkov effect is governed by the Frank-Tamm relation which describes the energy dissipated per unit length [40]:

$$\frac{dE}{dx} = \frac{(ze)^2}{c^2}\int_{\epsilon(\omega)>1/\beta^2} \omega\left(1 - \frac{1}{\beta^2\epsilon(\omega)}\right)d\omega \tag{1.3.2}$$

where z is the charge of the particle whose passing causes the Čerenkov effect, ω is the frequency of a photon produced and $\epsilon(\omega)$ is material dielectric constant. Expressed with respect to energy and for a given β and particle path length through the radiator of L Equation 1.3.2 can be re-written in terms of number of photons as:

$$N = \frac{2\pi\alpha L}{\hbar c}\int \sin^2\theta_c \, dE \tag{1.3.3}$$

where α is the fine structure constant. The number of detected photons $N_{obs} = wN$ where the weighting factor w is derived from the detector performance and is given by:

$$w = \int Q \cdot G \, dE \tag{1.3.4}$$

where Q is the intrinsic Quantum Efficiency of the chosen photon detection device and G is the geometric efficiency of the optical systems used in the detector. As both of these vary with λ they remain non-trivial integrands and the result of the integral which is unique to each detector system. The maximum number of observed photons is related to the threshold Lorentz factor $\gamma_t = (1 - 1/n_p^2)^{1/2}$ by the relation [40]:

$$N_{max} = \frac{\alpha L}{\hbar c}\frac{w}{\gamma_t^2} \tag{1.3.5}$$

and the mean number of observed photons for a given β is lower and governed by the relation:

$$\frac{N_{obs}}{N_{max}} = \frac{\gamma^2 - \gamma_t^2}{\gamma^2 - 1} = 1 - \frac{\eta_t^2}{\eta^2} \tag{1.3.6}$$

where $\eta = \beta\gamma$ and is related to the particle momentum by $\eta = p/m$ in natural units.

1.3.2 Čerenkov Detectors

The first and simplest type of detector utilising the Čerenkov effect were so-called threshold detectors. They were designed to distinguish between two particle species by designing the detector in such a way that β_t would only be achieved by the lighter of the two particle species for a given reaction that was to be studied. Detectors like this can be tuned by using a gas radiator and varying the pressure of gas within the radiator volume, thereby varying the gas density. As outlined in Equation 1.3.6 it is possible to determine particle momentum by accurately measuring the number of photons detected and thereby reconstructing the number produced.

An improvement on this system was proposed in the form of a Ring Imaging Čerenkov (RICH) detectors [41]. Position sensitive photon detection and a knowledge of the particle tracks and detector geometry can be combined to allow the reconstruction of θ_c and so an indirect measurement of particle β. With good particle track resolution prior to the detector a RICH system can measure β for high particle multiplicities and across a broad range of momenta. This addresses one of the main drawbacks of the threshold system, when more than one particle creates Čerenkov light within the same section of a threshold detector it is impossible to disentangle photons produced by one particle from the other.

A RICH detector contributes charged particle identification by measuring the impact positions of Čerenkov photons on a system of photon detectors and using this image to reconstruct the Čerenkov cone and thus β. They are typically described in four stages: photon production within the radiator and photon transportation through the optical system photon detection with a suitable photomultiplier device and pattern recognition after detection. The prototype FLDD is primarily concerned with the first two stages.

When a particle with direction $\mathbf{u}_p$ traverses a RICH detector it will produce a set of N photons with a corresponding set $\mathbf{u}_i$ of direction vectors. An ideal RICH bijectively[2] maps $\mathbf{u}_i$ onto the set x_i of spatial points on the detector surface. The detector output is then this set of spatial x_i values. As the mapping $f(\mathbf{u}_i) \mapsto x_i$ is defined by the detector geometry pattern recognition is achieved by applying the inverse mapping $f(x_i)^{-1} \mapsto \mathbf{u}_i$ and then using the $\mathbf{u}_p$ in combination with $\mathbf{u}_i$ to reconstruct the angle subtended by the cone with respect to $\mathbf{u}_p$. This angle is then θ_c.

[2] A Bijective mapping is one which is injective - maps onto every element in the co-domain from at most one element in the domain - and surjective - maps onto every element in the co-domain from at most one element in the domain. This is also known as *one-to-one* and *onto*.

If multiple particles are present within the detector at the same time then the set of observed photons x_j will include a set of x_i for each coincident particle. Pattern recognition in this case must first associate the subset of x_j which belong to a given particle with $\mathbf{u}_p$, a task that that requires detecting a minimum number of distinct x_i for each particle. This number varies with the number of coincident particles, the external tracking of each particle available to the reconstruction and the desired PID efficiency of the detector system.

Each stage of the process is subject to constraints which add uncertainty to the reconstructed θ_c and so the extracted β. The errors pertaining to single photons include: optical errors arising from surface quality, approximation of curved surfaces and the inherent difficulty in defining a suitable mapping f; the granularity of the photon detector; the multiple scattering of the traversing particle within the radiator; the bending of the particle trajectory arising from magnetic fields within the detector; the effect of chromatic dispersion in photon production arising from the λ dependence of Refractive Index, n.

Each of these are independent processes and so the error on a single photon reconstruction of the angle, σ_θ, is the quadrature sum of each contribution. If the detector observes N_{obs} photons from the same Čerenkov cone the overall uncertainty on θ_c is given by [40]:

$$\sigma_{\theta_c} = \frac{\sigma_\theta}{\sqrt{N_{obs}}} \tag{1.3.7}$$

The contribution arising from chromatic dispersion is greater than that arising from multiple scattering. For gaseous detectors this is often by an order of magnitude but it is also true of more dense liquid or solid radiators. The maximum momentum, p_{max}, at which it is possible to resolve between two particles of masses m_1 and m_2 is given by the relation:

$$p_{max} = \left(\frac{\beta^2 \Delta m^2 \eta_t}{2 n_\sigma \sigma_{\theta_c}} \right) \tag{1.3.8}$$

where n_σ is the number of standard deviations separation desired for successful separation. The value of p_{max} varies with radiator material choice and is high typically for gaseous when compared to liquid or solid radiators. The minimum momentum, p_{min}, is the momentum at which the most massive particle reaches β_t.

RICH detectors have relied upon solid, gel, liquid and gaseous radiators to produce Čerenkov photons throughout their existence. Examples of radiator choices include He, N_2 for gases, C_6F_{14} for liquids, LiF or SiO_2 for solids. Gaseous and liquid radiators are often expensive and are space intensive. It is in this regard that they are unsuitable for use in the $\bar{\text{P}}$ANDA Target Spectrometer (TS).

A solution utilising solid radiators was first implemented by the BaBar experiment on the PEP-II asymmetric e^+e^- collider at the Standford Linear Accelerator (SLAC) facility. It was the first detector to operate on the Detection of Internally Reflected Čerenkov radiation principle (DIRC) where the photons which undergo total internal reflection are extracted at the edge of the radiator and subsequently imaged [42]. The asymmetry gives rise to the distinctive Barrel DIRC design which is the basis for the barrel DIRC in the $\bar{\text{P}}$ANDA TS.

The success of the initial DIRC has lead to proposed adaptations into different geometries such as the FLDD, at the WASA-at-COSY experiment [43] and for the TORCH upgrade to RICH-II in LHCb [44].

1.3.3 The Focussing Lightguide Disc DIRC

The $\bar{\text{P}}$ANDA detector is designed to cover a full 4π solid angle. To achieve this detector functions will be separately present in the Forward Spectrometer, which covers $\theta_p < 5°/10°$, and in both the Barrel, which covers $\theta_{ploar} > 22°$ and Endcap, which covers $5°/10° \leq \theta_{polar} \leq 22°$ regions of the Target Spectrometer. It is in the Endcap region that a DIRC detector based on disc geometry will be constructed. This geometry is novel and unique to the $\bar{\text{P}}$ANDA Endcap. A space of only $60\,mm$ in the downstream direction is available and the design must be robust for magnetic fields up to $1.5\,T$.

Two competing designs are proposed to fit within the Endcap region, one based on a Time-of-Propagation (TOP) principle and the Focussing Lightguide Disc DIRC (FLDD) the prototype for which is discussed in this thesis. The TOP DIRC works by measuring the position of photon impact on the rim of the disc and the relative time of arrival of each photon to reconstruct the Čerenkov angle [45].

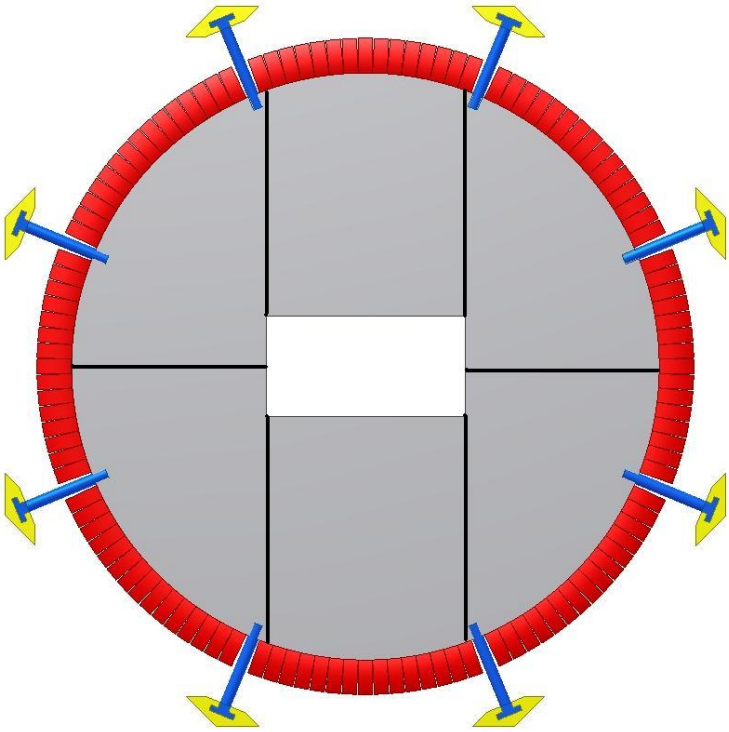

Figure 1.10: The front elevation of the Focussing Lightguide Disc DIRC (FLDD). The asymmetric central hole through which the beam line passes is centrally located and the 6 sections marked. It can be seen that the 6 sections are constructed from 2 designs: 2 central sections with 3 straight edges and 4 side sections with 2 straight edges. The removal of Focussing Lightguides due to support arms, blue, is clearly visible.

The FLDD will be a 128-sided polygon with a radius of $1100\,mm$ and a thickness of $15\,mm$ [46]. The chosen radiator material will be synthetic fused silica similar to that used by BaBar. Production of fused silica in the grade required for the FLDD necessitates the design to be constructed from 6 sections, introducing glue joints as marked in Figure 1.10. Support arms will be connected in 8 places, occupying 1 of the 128 sides

per arm. This will result in a dead section covering $\pi/64$ Radians per arm. The remaining 122 sides will be connected to a hardware based chromatic dispersion correction element, Chapter 2. The titular Focussing Lightguides are attached to each of these elements. They are designed on the principle of parallel-to-point optics and map the angle of photon propagation onto a position on the focal plane of the Lightguide. The focal plane is the instrumented by a position sensitive photon detector. Example expected patterns from the initial FLDD design are shown in Figure 1.11.

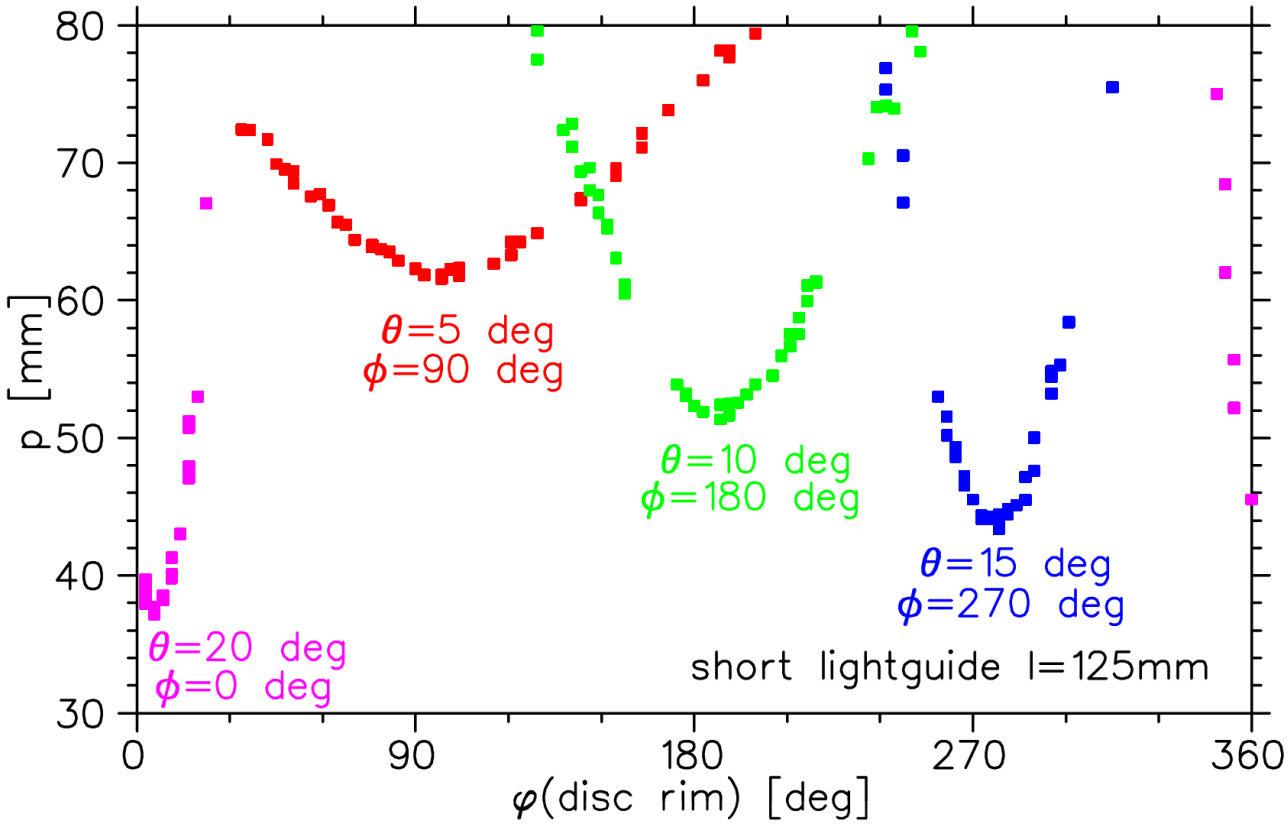

Figure 1.11: Simulated example patterns for an initial design of the FLDD. The coordinates used are the impact position, p, from the centre of the detector and azimuthal angle, ϕ, within the detector system. A central impact position corresponds to $0\,mm$ and a photon travelling straight up corresponds to 0°.

The choice of radiator material or materials is vital to the design of every Čerenkov detector as it defines the dynamic range over which the detector will work. Within DIRC detectors, however, the radiator material choice is of greater importance as it also must perform in photon transportation and as a mechanical structure. These roles must be balanced with the cost and usability of the material.

The BaBar DIRC used synthetic fused silica and this was the *de facto* starting point for the FLDD also [47]. Fused silica offers a refractive index in the range $1.45 \leq n_p \leq 1.55$ for $300\,nm \leq \lambda \leq 700\,nm$. This index range also allows for photon production over the short length available within the Endcap of the $\bar{\text{P}}$ANDA detector. Fused silica remains transparent in the near-UV and middle-UV wavelength ranges where the greatest number of Čerenkov photons will be produced thus increasingly the usable wavelength bandwidth of the detector.

The environmental conditions within $\bar{\text{P}}$ANDA also present challenges that any radiator material must over-

come. Central amongst these is the ability to withstand the radiation doses present within the $\bar{\text{P}}$ANDA Target Spectrometer. The expected lifetime dose in within $\bar{\text{P}}$ANDA is $\approx 100\,krad$ and samples of three brands of synthetic fused silica, Corning 7980, Lithosil Q0 and Suprasil 1, were irradiated to test for optical conductivity after $10\,krad$, $100\,krad$, $1\,Mrad$ and $10\,Mrad$ of absorbed dose. The %-transmission before irradiation and normalised transmission difference $\Delta T_{norm} = T_{before} - T_{after}/T_{before}$ is shown in Figure 1.12.

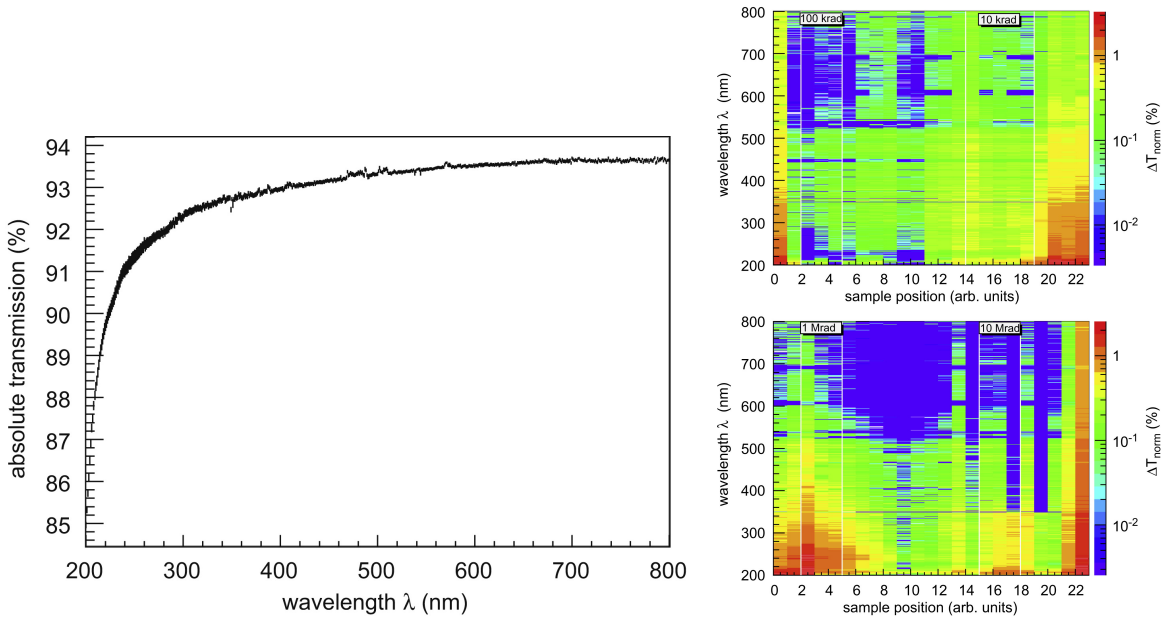

(a) (b)

Figure 1.12: The %-transmission of a non-irradiated sample of Suprasil 1 is shown in a). The values are not corrected for Fresnel losses. The ΔT of the sample after irradiation is shown in b). Vertical lines show expected position of the radiation spots and are labelled with the dose received. The top plot of b) corresponds to one edge of the sample and the bottom plot to the opposite edge. Positions are the lateral position along the sample edge, divided into 23 bins.[48]

The specifications for the radiator used in the final detector are envisaged to match those of the BaBar DIRC [47]. As photons traversed a longer path length and underwent more numerous surface interactions within the BaBar radiator bars than is anticipated in the FLDD it is likely that the specifications will be in excess of the minimum required for performance within the $\bar{\text{P}}$ANDA system. The accepted surface roughness was up to 7.5 Å.

The most novel element within the FLDD design is its hardware based chromatic dispersion correction element. A cuboid measuring $50 \times 50 \times 15\,mm^3$ constructed of monocrystaline Lithium Fluoride (LiF) is proposed for this function. It will be directly connected to the 122 active sides, marked in red on Figure 1.10, and will rely on a $dn/d\lambda$ variation that differs from that of fused silica suitably to correct for the inherent dispersion present upon creation. The performance of this component is discussed in detail in Chapter 2.

Upon exit of the LiF element photons produced from the same particle should enter the Focussing Lightguide (FLG) parallel to one another. The focussing surface of the element is then designed to focus parallel light onto a specific position on a focal plane. Such a step is required to remove the ambiguity in the photon

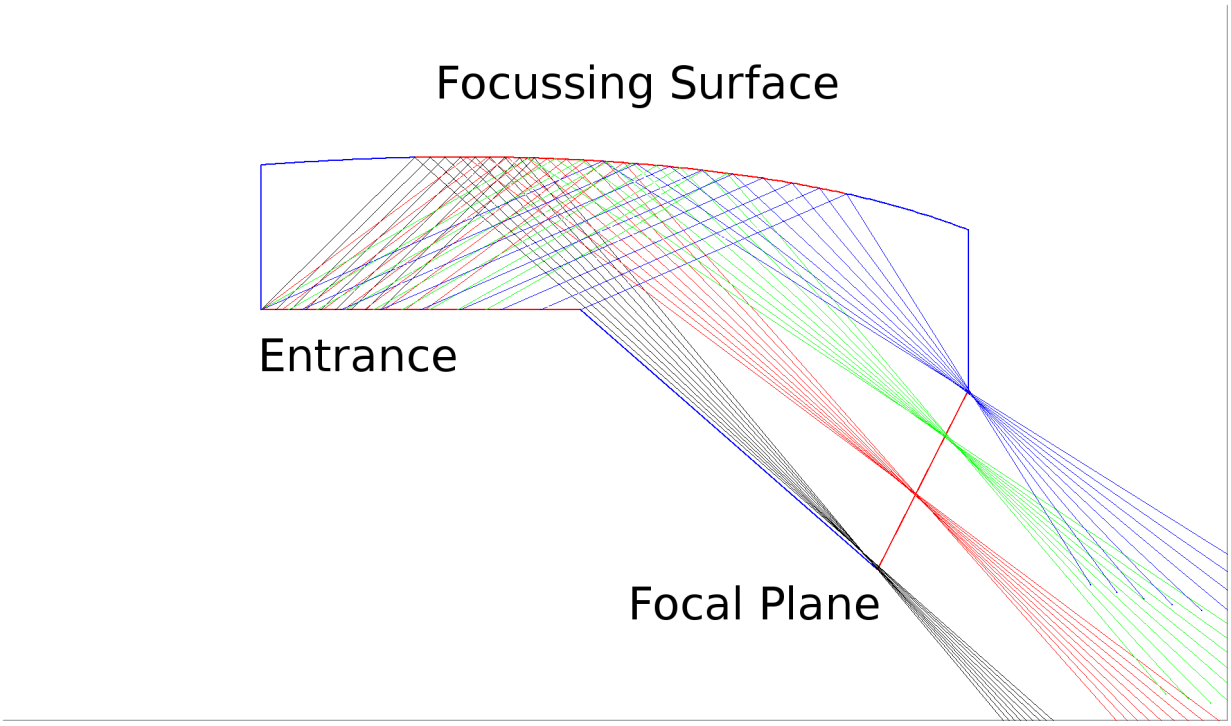

Figure 1.13: The design of the FLG used throughout prototype testing. Each colour represents a specific angle of photon propagation upon entry to the lightguide. The focussing surface directs light travelling with the same angle of propagation onto a specific position upon the focal plane.

production origin and to ensure the surface of the position on the focal plane is dependent solely on photon propagation angle. The input for the design of the Focussing element was calculated by taking the range of angles that will be present in the radiator disc, passing them through a perfect representation of the LiF element and using the resultant angular distribution. The surface was then designed with the optimisation criterion to minimise the average spread of light on the focal plane for 5 input angles of θ_p, spanning the full range expected in the final detector, and entering the lightguide at 5 differing positions spanning an isotropic distribution on entry to the lightguide. A discussion of the FLG performance and its impact on the overall FLDD performance can be found in Chapter 4.

A position sensitive photon detection device is a prerequisite for the FLDD design to work. The focal plane of the FLG was limited to $51 \times 51\,mm^2$, the active area of a Photonis Burle XP85011 Microchannel Plate Photomultiplier (MCP-PMT), Figure 1.14. This PMT is considered the base candidate for use in the FLDD, as well as the Barrel DIRC. Studies have shown that the current PMT options show a sufficient deterioration in gain to be inoperable over the whole $\bar{\text{P}}$ANDA lifetime [49]. Some performance requirements for any suitable candidate MCP-PMT are discussed along with the FLG in Chapter 4.

The geometric differences between the FLDD design and the successful BaBar DIRC lead to two clear mechanical engineering questions: can the joints of the central suspended section, see Figure 1.10, withstand the load imparted by the central section using only a two component epoxy resin and without aid of structural support; and is the disc able to withstand the load imparted under contact with the two bottom support arms.

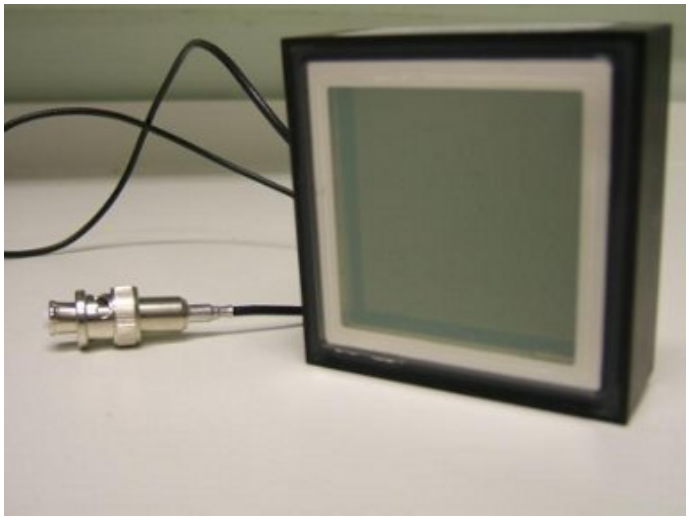

Figure 1.14: A Photonis Burle Planacon 85011-501 MCP-PMT. Compact position sensitive devices such as this are under consideration for use by the $\bar{\text{P}}$ANDA Čerenkov group.

The glue joints were tested throughout the course of prototype testing and were found to survive a load $> 9.6\,MN/m$ minimum. The tests were carried out on fused silica discs of $\varnothing = 20\,mm$ using a sheer stress machine at the Mechanical Engineering section of the University of Glasgow. The results were the extrapolated by area to the contact area between the central section of the FLDD and the two neighbouring "corner" sections. The equivalent load placed upon the joints of the central disc section will be $37.95\,kN/m$. It was noted that the bonds remained intact and the samples had shattered in all tested cases. The bonds are therefore of sufficient strength for use in the FLDD.

1.3.4 The Prototype Development

The FLDD design is novel in its geometry and in its approach to Chromatic Dispersion correction. It is therefore crucial to develop a prototype which tests the decisions made its design. A three step approach was used for the development of the prototype.

The first stage was to test the Lithium Fluoride Dispersion correction element. An optical bench based experiment comparing the path of light at wavelengths within the range planned for the FLDD with and without Lithium Fluoride was design and is discussed in detail in Chapter 2.

The second stage was to confirm the simulated performance of the chosen Heraeus Suprasil fused silica radiator. A photon counting experiment consisting of an example bar of Suprasil 1 and a conventional 2-inch Photomultiplier tube was designed to achieve this. It is discussed in detail in Chapter 3.

The final stage was to combine the LiF element with the fused silica radiator and an example FLG to test the performance of the combined system alongside an optical simulation. A Hamamtsu H9500 multi-anode Photomultiplier was used to give a position sensitive readout. It is discussed in detail in Chapter 4.

Chapter 2

Chromatic Dispersion Correction

There are uncertainties introduced in any detector which result from the fundamental physics underlying their operation, and which must be minimised to achieve the full potential of any detector design. With every Čerenkov detector these unavoidable uncertainties are dominated by Chromatic Dispersion introduced as a result of the variation in Refractive Index with wavelength. Corrective systems fall in to the two broad of categories software- or hardware-based, relying on precise timing or photon trajectory alteration respectively.

The Focussing Lightguide Disc DIRC (FLDD) has chosen a hardware based system. The selection of a medium with a suitably varying $dn/d\lambda$ from that of the radiator, and designed with a suitable geometry to allow for the correction of the dispersion by process of refraction. A cuboid of Lithium Fluoride placed between the edge of the radiator and the entrance window of the Focussing Lightguide. A simple optical experiment was devised to verify the simulated parameters of this component.

2.1 Dielectric Materials and Refractive Index

The Čerenkov effect occurs when a particle carrying electric charge traverses a dielectric medium with a velocity $\mathbf{v}$ such that $|\mathbf{v}| > |\mathbf{v}_p|$, the phase velocity of light in the medium. A dielectric medium is electrically insulating and able to be polarised under an applied electric field. The magnitude of the phase velocity is given by $|\mathbf{v}_p| = c/n_p$ where n_p is the real part of the phase Refractive Index of the medium. It is the variation of $|\mathbf{v}_p|$ with λ or μ that gives rise to optical dispersion.

The decrease in the velocity of light within matter, when compared to vacuum, is as consequence of scattering. As the light scatters from the individual constituents of the matter being traversed the scattered waves interfere with the primary impinging wave. This interferences changes the phase of the wave, and thus the wave velocity. At wavelengths suitably far from absorption bands within a material it is possible to show the connection between scattering and refractive index. We can achieve this by studying the change in intensity caused by scattering from a material with scattering coefficient α_s and thickness, t, which is small compared to λ. The change in intensity in this case is:

$$dI = -\alpha_s t I_0 \tag{2.1.1}$$

The intensity scattered by a single atom, for a density of Nt atoms per unit area, is thus:

$$I_a \approx \frac{\alpha_s t}{Nt} = \frac{\alpha_s}{N} \tag{2.1.2}$$

and, if we assume a wave of the form $E = e^{ikx}$ at a given time, a resulting amplitude of the scattered wave of:

$$E_a \approx \sqrt{\frac{\alpha_s}{N}} \tag{2.1.3}$$

As the light scattered in the direction of propagation of the primary light source is coherent we must sum the contributions to amplitude from each atom, resulting in a scattered wave amplitude, E_s, of:

$$E_s \approx Nt\sqrt{\frac{\alpha_s}{N}} = t\sqrt{\alpha_s N} \tag{2.1.4}$$

At a distance R_0 along he path of primary beam propagation, and a distance R from the scattering volume the two waves will be superimposed given a resulting amplitude of:

$$E + E_s = e^{ikR_0} + t\sqrt{\alpha_s N}\int_0^\infty \frac{2\pi r}{R} dr\ e^{ikR} \tag{2.1.5}$$

where r is the distance between the central axis of the primary wave and the Nt particles from the scattered amplitude emanates. As $R^2 = R_0^2 + r^2$, it follows that $r\ dr = R\ dR$ and so the integral becomes:

$$\int_0^\infty \frac{2\pi r}{R} dr\ e^{ikR} = \int_{R_0}^\infty e^{ikR} dR = \frac{2\pi}{ik}\left[e^{ikR}\right]_{R_0}^\infty \tag{2.1.6}$$

As the source wave must have finite length the scattered amplitude will have no effect for $R > R_0$ and so we have:

$$\begin{aligned} E + E_s &= e^{ikR_0} - t\sqrt{\alpha_s N}\ \frac{\lambda}{i}\ e^{ikR_0} \\ &= e^{ikR_0}(1 + i\lambda t\sqrt{\alpha_s N}) \end{aligned} \tag{2.1.7}$$

The second term in parenthesis is small compared to the first and so these terms combined are the first two terms in the expansion of $e^{i\lambda t\sqrt{\alpha_s N}}$. Therefore the coherent wave amplitude is:

$$E + E_s = exp\left[i(kR_0 + \lambda t\sqrt{\alpha_s N})\right] \tag{2.1.8}$$

Which means that the initial wave has undergone a phase shift of $\lambda t\sqrt{\alpha_s N}$. It is also true that such a thin material will cause a phase retardation of $(2\pi/\lambda)(n-1)t$. It is therefore true that:

$$\begin{aligned} \lambda t\sqrt{\alpha_s N} &= \frac{2\pi}{\lambda}(n-1)t \\ n - 1 &= \frac{\lambda^2}{2\pi}\sqrt{\alpha_s N} \end{aligned} \tag{2.1.9}$$

It is therefore clear that refractive index and scattering are related and are both Chromatically dependent. The verified modelling of the Refractive Index of the materials used in the FLDD design is crucial to judging its potential performance. Dispersion behaviour falls in to two categories, *normal* and *anomalous*.

In the case of *normal dispersion* four conditions are satisfied: the Refractive Index increases with decreasing λ; the rate, $dn/d\lambda$ increases as λ decreases; for a given λ, $dn/d\lambda$ will be greater if n itself is greater; it is not possible to recreate the curve for a substance simply by changing the ordinates of the curve for another.

The Cauchy Equation was able to successfully model *normal dispersion* and give relations for both n and $dn/d\lambda$ in terms of a series of material specific constants, A, B and C.

$$n = A + \frac{B}{\lambda^2} + \frac{C}{\lambda^4} \tag{2.1.10}$$

$$\frac{dn}{d\lambda} = -\frac{2B}{\lambda^3} - \frac{4C}{\lambda^5} \tag{2.1.11}$$

The equation, however, has no mechanism for dealing with the natural absorption wavelengths of the material it is modelling. As $\lambda \to \infty$ Equation 2.1.10 predicts that $n \to A$. The presence of an absorption band results in a the observed Refractive Index deviating from the Cauchy prediction below A as λ approaches the band. Once λ exceeds the absorption band the Cauchy equation again describes the behaviour of n, though the constants A,B and C differ from those in the previous regime in which the equation held. As such it is also true that in this new regime n starts with a value greatly in excess of A, as predicted. This discontinuity over the absorption band is called *anomalous dispersion*, where higher wavelengths are bent to a greater extent than short ones, in contradiction with normal experience within the optical range.

To overcome the effects of absorption on Refractive Index it was proposed to model materials as though composed of particles which were bound by elastic forces, and have a natural frequency of vibration, ν_0. Impinging light waves of frequency ν impart a periodic force on the particles as they pass. If $\nu \neq \nu_0$ the vibration induced in the particles will be forced and so have a small amplitude, rising as ν approaches ν_0 until, at $\nu = \nu_0$, the resonance peaks. These vibrations act upon the light wave and impede its progress and, at resonance, halt it. The Sellmeier Equation incorporates this and takes the form, as function of λ:

$$n^2 = 1 + \sum_i \frac{A_i \lambda^2}{\lambda^2 - \lambda_i^2} \tag{2.1.12}$$

where each of the λ_i correspond to a natural resonance frequency ν_i. As the wavelength approaches an absorption value from below $n \to -\infty$ and from above $n \to +\infty$, which is non-physical. In addition the predictions of the equation differ from observation in the immediate vicinity of the absorption value. For the FLDD, however, λ values included in the design are sufficiently far from any value of λ_i that the Sellmeier Equation holds.

By modelling the material as a collection of damped oscillators, and the impinging light wave as providing a forced oscillation, the process by which Refractive Index and wavelength are linked becomes clear. Secondary waves are the superposition of the scattered waves from the oscillators mentioned above and, as above, must

be superimposed with the original wave. This superposition results in a change of phase of the original wave The magnitude of this change is given by taking the vector sum of the original wave and the secondary wavelet. The phase change induced is therefore a combination between the amplitude of the secondary wavelets, which peaks at λ_i, and their phase lag, which is $\pi/2$ at wavelengths significantly longer than λ_i, crosses a lag of π at λ_i and approaches a $3\pi/2$ for λ significantly shorter than λ_i.

2.2 Dispersion Correction and Lithium Fluoride

Once a radiator material is chosen the Chromatic uncertainty in the production of Čerenkov photons is set. It is imperative to correct for this uncertainty within the detector design. Two sets of correction systems have been postulated: software- or timing-based and hardware-based.

2.2.1 Software- or Timing-based Correction

The propagation velocity of a photon within any medium varies with the wavelength carried by the photon. This speed is the *group velocity* of light within the medium and differs from the *phase velocity* which is used in Equation 1.3.1 and discussed in Section 2.1. The group velocity, u, and phase index, n, are related by:

$$\frac{c}{u} = n - \lambda \frac{dn}{d\lambda} \tag{2.2.1}$$

Sufficient resolution in the timing of photon arrival can be combined with the requisite positional information of the detector system to reduce Chromatic uncertainty. Precise knowledge of the time of arrival of the first photon from an given particle combined with knowledge of the particle track through the detector allows wavelength to be discerned with a precision which improves with improved timing resolution. Correction must then be applied during the "offline" analysis of the data as the pattern recognition algorithms are computationally expensive. Such algorithms are outwith the scope of this thesis.

The FLDD design requires 122 instrumented Lightguides, each with 32-channels read out, totalling 3904 channels. Combined with the lack of a central trigger within the $\bar{\text{P}}$ANDA system this option was considered impractical for use in the FLDD.

2.2.2 Hardware-Based Correction

As every material has different refractive and dispersive properties it is possible to select a secondary material which refracts the light such as to correct the initial dispersion. To achieve this the secondary material must combine appropriate geometry and a suitable $dn/d\lambda$ such that the light entering the Focussing Lightguide (FLG) is parallel. The increase parallelism reduces the chromatic element contained within the photon propagation vector. The FLG is then required only to map angle of photon propagation onto position on the detector plane.

This role will be performed within the FLDD design by a cuboid piece of Lithium Fluoride (LiF). It was

chosen as it is highly transparent in the UV, with a cut off at $120\,nm$, and has a $dn/d\lambda$ which varies from fused silica. This difference is selected such that an initial refraction combined with a secondary refraction into the fused silica FLG , through a surface at 90° to the initial surface. A simple rectangular cuboid was used.

The Refractive Indexes of phase for both LiF and fused silica are shown with the group Index for fused silica in Figure 2.1. The differing $dn/d\lambda$ values are clearly visible. Also shown is the group Index for fused silica, as used for the group velocity in Equation 2.2.1.

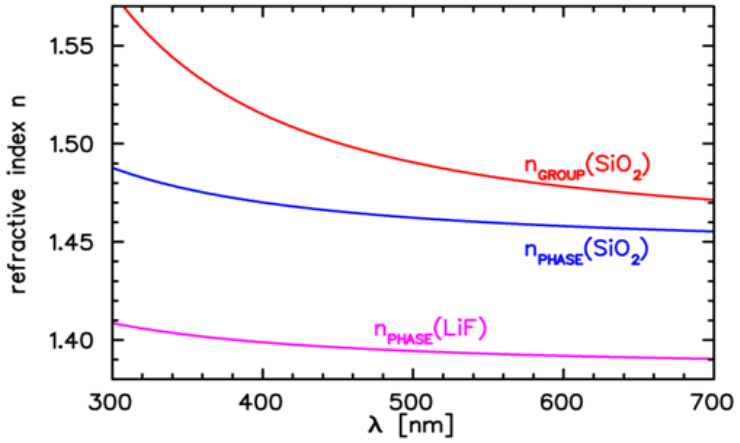

Figure 2.1: The Refractive Indexes of phase for LiF and SiO_2 as a function of λ. The production of Čerenkov light and the refraction of light at material boundaries depends on n_{phase}. The different $dn_{phase}/d\lambda$ between the two materials allows for dispersion correction. Shown also is n_{group} for SiO_2 which affects the velocity of propagation of Čerenkov photons.

Theoretical calculations to show the spread in detected θ with and without LiF were carried out using the first two stages of the FLDD design. These do not take into account the performance of the lightguide or of pattern recognition algorithms. The calculated spread in angle, $\Delta\theta_{obs}$, is the chromatic contribution to Čerenkov angle uncertainty, σ_{chr}. A reduction in angular spread therefore reduces the uncertainty in observed θ, σ_θ. Any reduction in σ_θ leads to a reduction in σ_{θ_c} as defined in Equation 1.3.7. The predicted angular spread $\Delta\theta_{obs}$, expressed in radians, for a $\beta = 1$ particle over the wavelength range $337\,nm - 633\,nm$ without Lithium Fluoride is:

$$\Delta\theta = 14.070^{+5.9\times10^{-3}}_{-3.2\times10^{-3}}\,mrad \tag{2.2.2}$$

The $\Delta\theta_{obs}$ for a $\beta = 1$ particle at $\theta_p = 5°$ over the wavelength range $337\,nm - 633\,nm$ with Lithium Fluoride is:

$$\Delta\theta = 2.80104^{+1.127\times10^{-2}}_{-2.608\times10^{-2}}\,mrad \tag{2.2.3}$$

The $\Delta\theta_{obs}$ value is reduced by a factor of ~ 5. If Chromatic dispersion was the only contribution to σ_{θ_c} it would result in an improvement of $5/\sqrt{N}$ where N is the number of observed photons. For $N = 10$, to

allow pattern recognition to be performed, this results in an improvement of a factor of $5/\sqrt{10} \approx 1.581$ in Čerenkov angle uncertainty.

To verify this improvement two experiments were devised. The first experiment was a Brewster's angle experiment to verifying the Refractive Index at the utilised wavelengths. The second was a set-up to compare the performance of the LiF block in a set-up analogous to the final FLDD design with the same set-up constructed of pure fused silica.

2.3 Refractive Index Confirmation

Manufacturer data for material properties such as absorption length and Refractive Index is provided for every material and is precisely measured. Verification of manufacturer specification is important for understanding both the performance of the prototype and for tolerances associated with the final FLDD design. Measurement of the Refractive Index was carried out on the samples to be used to test for Dispersion correction. A simple Brewster's Angle set-up was used for these measurements, as shown in Figure 2.2. The samples were three Suprasil-1 fused silica blocks each of dimension $50 \times 50 \times 20\,mm^3$ and a single LiF block of $50 \times 50 \times 15\,mm^3$.

Two light sources were used: a monochrome laser with $\lambda = 633\,nm$ and a Mercury vapour lamp which peaks clearly at $\lambda = 578.2$, 546.1, 435.8, 404.7 and $365.4\,nm$. To split the Mercury lamp into its spectrum and allow for use in measurements a Pellin-Broca prism was used [50]. Such a prism works by admitting the combined spectrum and reflecting a single wavelength at exactly 90° and the used of apertures to select only that wavelength allows for accurate separation of the source. A schematic of this is in Figure 2.3.

A Hamamatsu C9200-901 CCD with 1344×1024 pixels was placed behind the sample stage and a live image taken with no sample present. The sample was added and aligned such that the transmitted light was aligned on the same CCD pixels as when no sample was present. The images were both recorded and examples are shown in Figure 2.4. The system was then set up such that this was defined to be 0°.

The CCD spectra then had a Region-of-Interest (ROI) defined within the acquisition system. The x-axis projection of the ROI is then taken and the system extracts the mean value of the data and the FWHM of the distribution. This process was repeated to ensure reproducibility in results; an second example of a calibration run is shown in Figure 2.5.

The sample was then rotated using a rotation stage with accuracy of ± 2.5 minutes of arc. This corresponds to an uncertainty of $\pm 0.7272\,mrad$, sufficient to detect the predicted improvement in $\Delta\theta$. The sample was rotated until the observed reflected intensity dropped to a minimum. This was then taken to be the Brewster Angle, θ_B. The Brewster angle is linked to the refractive index by:

$$\tan\theta_B = \frac{n_{sam}}{n_{sur}} \tag{2.3.1}$$

Where n_{sam} is the Refractive Index of the sample to be measured and n_{sur} is the Refractive Index of the sample surroundings, in this case air. As the manufacturer data is stated to a precision of 10^{-5} the Index

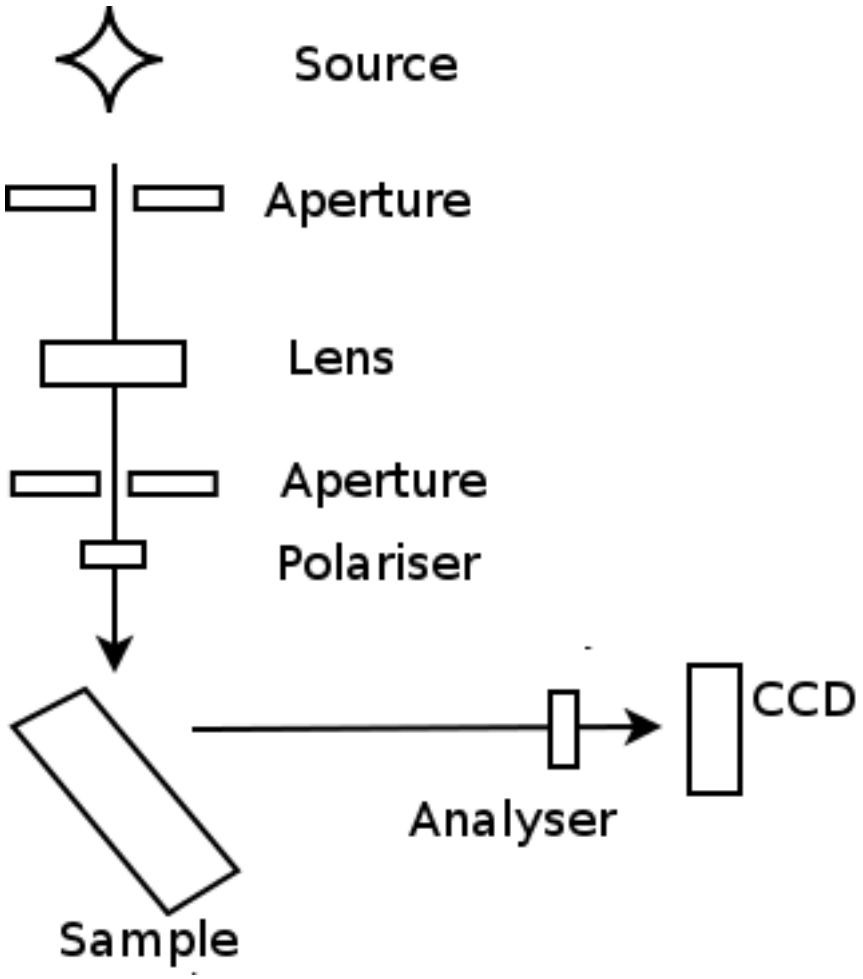

Figure 2.2: The set-up for measuring Refractive Index. The source passes through a series of apertures and lenses to construct a parallel beam which is then reflected off the sample, through the polariser and onto a CCD. When no light of a specific polarisation is reflected the Brewster's condition is satisfied.

of air is a non-negligible value and was included throughout [51]. A summary of the results is presented in Table 2.1.

As can be seen the observed data is in agreement with the manufacturer supplied data for both fused silica and LiF. The uncertainties on the measured Indexes arise solely from the measurement uncertainty in the Brewster Angle. The uncertainties on the manufacturer's data were not provided and so were taken to be ± 0.5 of the lowest digit. These uncertainties are well below that which is detectable with the given set-up. As the manufacturer data were in agreement and measured to greater precision than with the experimental set-up they were used for all theoretical calculations.

2.4 Chromatic Dispersion Correction Verification

The performance of the Lithium Fluoride block to correct for the dispersion discussed in Section 2.2 is central to the design of the Focussing Lightguide Disc DIRC. To test its performance a simplified geometric set-up analogous to the FLDD design was conceived, utilising the components for which the manufacturer data was

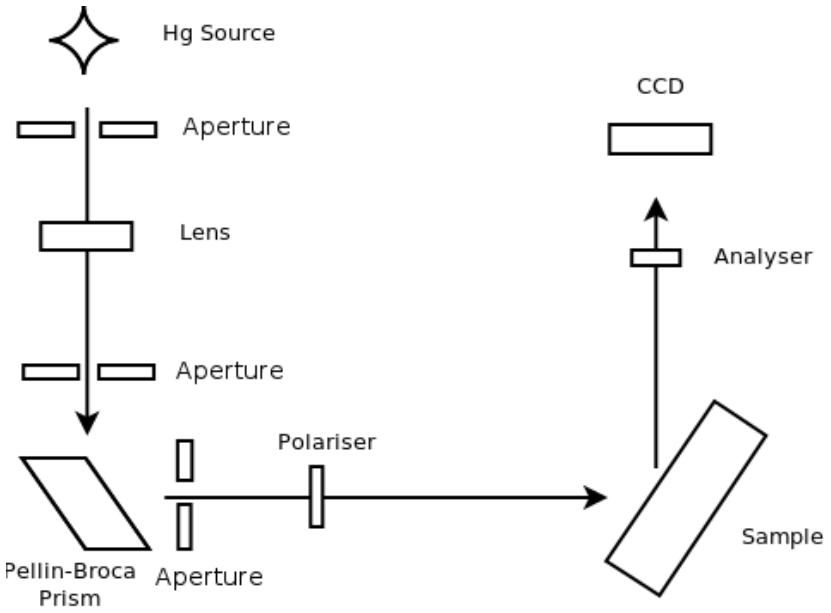

Figure 2.3: The modified version of the set-up shown in Figure 2.2. The addition of the Pellin-Broca prism and the resultant 90° offset is marked.

Table 2.1: The measured Refractive Index at the wavelengths of a HeNe laser and the four main peaks of a Hg lamp compared to those provided by the manufacturer.

Material	Wavelength (nm)	Manufacturer Refractive Index	Measured Refractive Index
Fused Silica	365	$1.47454 \pm 5 \times 10^{-6}$	1.474 ± 0.132
	436	$1.46668 \pm 5 \times 10^{-6}$	1.469 ± 0.132
	546	$1.46008 \pm 5 \times 10^{-6}$	1.461 ± 0.131
	578	$1.45881 \pm 5 \times 10^{-6}$	1.455 ± 0.130
	633	$1.45702 \pm 5 \times 10^{-6}$	1.454 ± 0.130
Lithium Fluoride	365	$1.40144 \pm 5 \times 10^{-6}$	1.398 ± 0.123
	436	$1.39697 \pm 5 \times 10^{-6}$	1.395 ± 0.123
	546	$1.39311 \pm 5 \times 10^{-6}$	1.391 ± 0.122
	578	$1.39235 \pm 5 \times 10^{-6}$	1.391 ± 0.122
	633	$1.39127 \pm 5 \times 10^{-6}$	1.386 ± 0.121

test in Section 2.3. The layout for the set-up is shown in Figure 2.6 and consists of the same two sources as in Section 2.3, a monochrome source at $\lambda = 633\,nm$ and a Mercury lamp with peak wavelengths at $\lambda = 578$, 546, 436, $365\,nm$, a right-angle triangular prism of fused silica to couple the light into the test components, an initial fused silica block, the replaceable second block of LiF or fused silica, and a final fused silica block before detection. All components were joined using an optically conductive silicone gel. These components represent the radiator, the potential addition of a LiF block and the Focussing Lightguide. The focussing surface was not included to allow the most direct access to the refracted photon propagation path.

As in Section 2.3 the wavelength from the Mercury source was selected by means of a fused silica Pellin-Broca prism. The set-up in Figure 2.6 was then rotated such that the light struck the silica-air boundary of the

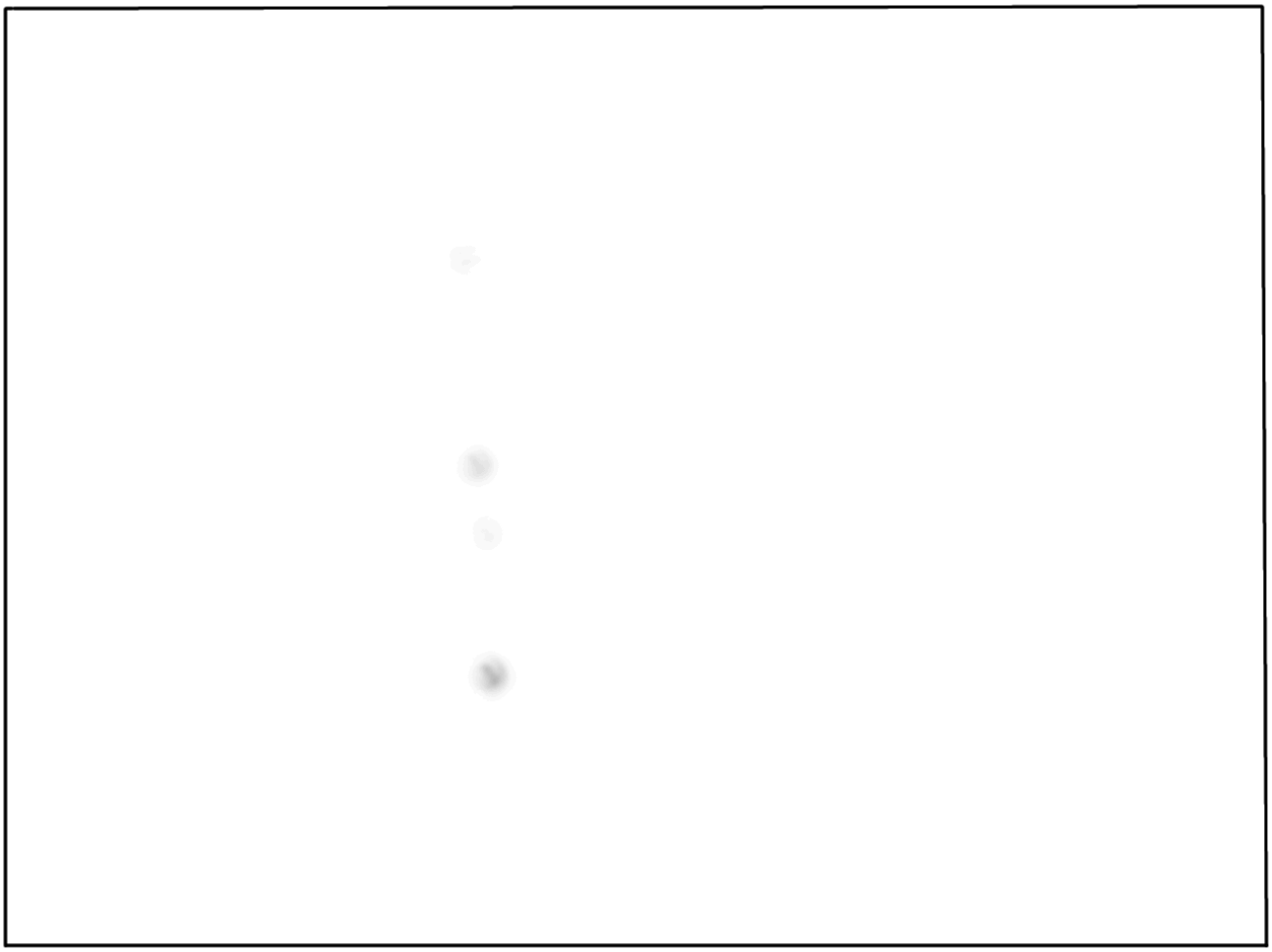

Figure 2.4: Example CCD image with a fused silica sample present. The primary peak is in the bottom left of the image and secondary peaks can be seen above, these are introduced by reflections at each of the collimation components.

first fused silica block at an angle which was either the Critical angle for the selected λ or the angle that will result from the Čerenkov angle for a particle at $\beta = 1$. The light propagates through the sample under test and then into the final fused silica block. Upon exit the light is detected by the CCD at position A and the spectrum taken. The CCD is then moved on a fixed rail through a distance of $10\,mm$, $25\,mm$ and $50\,mm$ and a spectrum taken at each. The starting position of the CCD relative to the set-up axis of rotation was varied to account for the change in exit position for the light being measured. The distance along the CCD measurement axis gives the z-coordinates and the CCD pixel the x-coordinates of the photon vector in the CCD coordinate frame.

The angle of rotation of the set-up with reference to the Set-up Alignment Axis gives the rotation of the final silica block from which the shown θ_{offset} with the CCD z-axis can be calculated. All the measured vector angles were adjusted by this angle to give θ_{exit}, formed by the light refracted upon exiting the final fused silica block. As the refractive index data were confirmed in Section 2.3 this was directly converted into the angle of propagation prior to refraction, θ_{disp}. The change in λ dependence caused by replacing the second

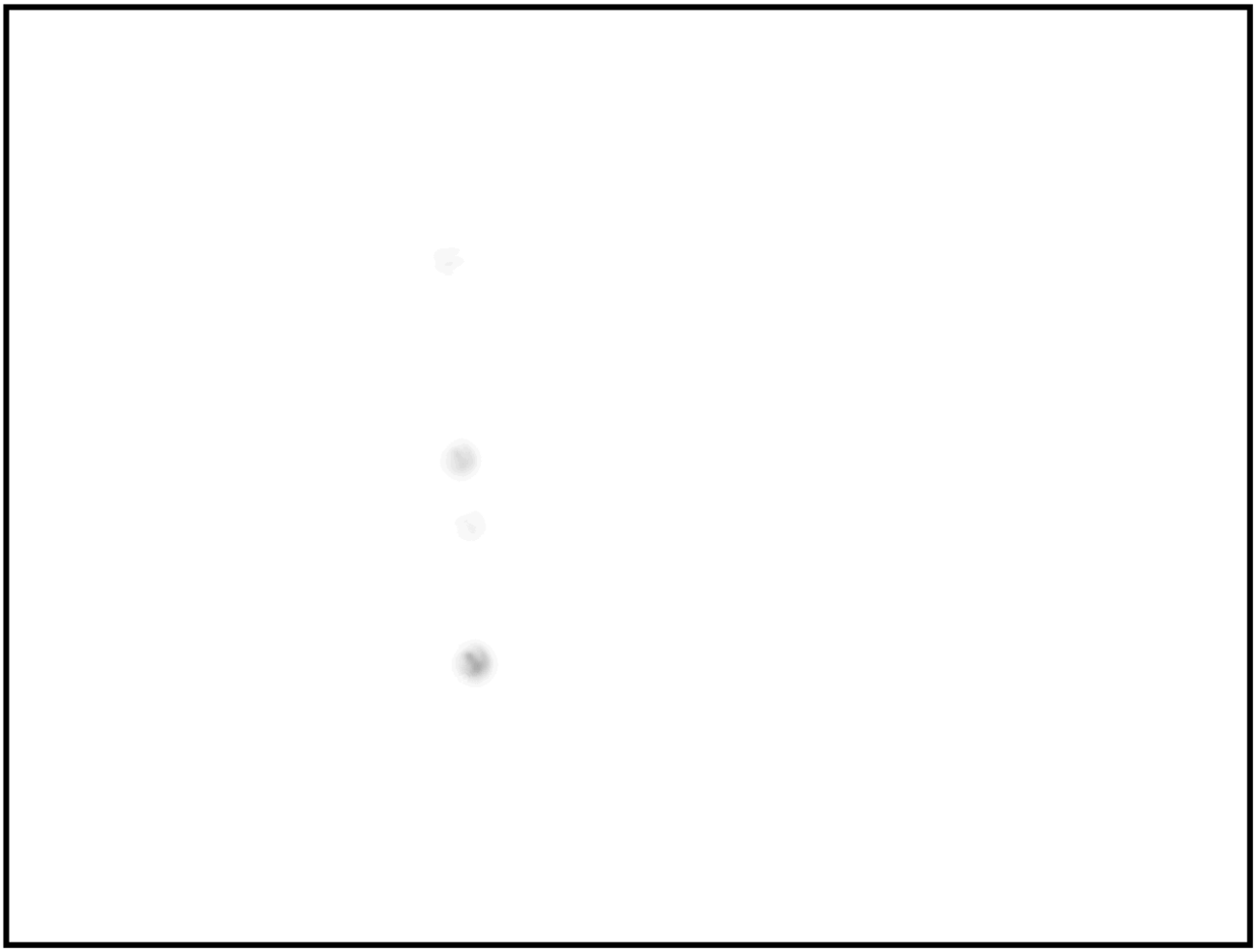

Figure 2.5: Example CCD image with a LiF sample present. Secondary peaks are present as is in Figure 2.4.

fused silica block with a LiF block will show the level of Chromatic Dispersion Correction resulting from the LiF. A diagram of the angles is shown in Figure 2.7.

The spread of angles was predicted first for a fused silica only case and then for the case where LiF was added. Table 2.2 shows the theoretical angles for the set-up with only fused silica and one with Lithium Fluoride added. All angles are measured relative to the normal of the external surface of Block 2.

The predicted reduction in spread caused by the introduction of Lithium Fluoride is $8.803\,mrad$ which results in a spread which $\approx 1/4.75$ that of the pure fused silica construction. The level of uncertainty is therefore predicted to be close to that caused by multiple scattering which has an rms spread of $\Theta_{rms} = 0.001721\,rad$.

2.4.1 Results

The set-up was aligned using a three-point alignment system and the 0° reference angle was taken to be when the entrance window of the right-angled prism was perpendicular to the optical axis. The set-up is then rotated through θ_{set} such that the light strikes the external surface of the first fused silica piece, Block 2, at the desired angle. The angles tested correspond to the θ_c for a $\beta = 1$ particle incident at $\theta_p = 5°$for

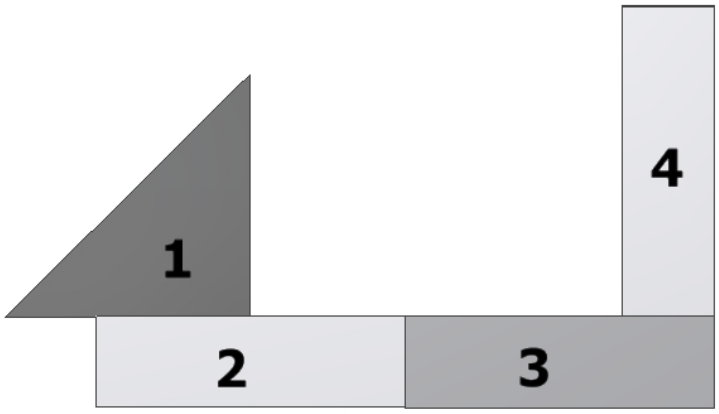

Figure 2.6: Schematic of the set-up devised to test the efficiency of LiF as a solution to Chromatic Dispersion Correction. Block 2 and 4 are fused silica, as used for Refractive Index verification, whilst block 3 is interchanged between a fused silica block and the LiF block for testing. A fused silica right-angled prism is used to couple the light in to the first block.

Table 2.2: The predicted angles after entry into the final fused silica Block 4. All angles are measured with respect to the normal to the external surface of Block 2.

Material	Wavelength (nm)	Theoretical Final Angle θ_f (rad)	$\Delta\theta_f$ (rad)
Fused Silica	365	$1.000053 \pm 3.1 \times 10^{-6}$	$0.011155 \pm 3.146 \times 10^{-5}$
	436	$0.995096 \pm 3.2 \times 10^{-6}$	
	546	$0.990874 \pm 3.2 \times 10^{-6}$	
	578	$0.990056 \pm 3.2 \times 10^{-6}$	
	633	$0.988898 \pm 3.2 \times 10^{-6}$	
Lithium Fluoride	365	$0.897768 \pm 2.8 \times 10^{-6}$	$0.001761 \pm 4.024 \times 10^{-6}$
	436	$0.897127 \pm 2.8 \times 10^{-6}$	
	546	$0.896415 \pm 2.9 \times 10^{-6}$	
	578	$0.896251 \pm 2.9 \times 10^{-6}$	
	633	$0.896007 \pm 2.9 \times 10^{-6}$	

each wavelength.

The spectra for each CCD data point was taken and fitted with a Gaussian distribution to establish impact pixel, as in Section 2.3. The axis along which the CCD ran was defined to be the z-axis and the lateral position, translated from pixels to mm, is the x-axis. The set of measured (x,z) coordinates give a vector which forms a given angle θ_{CCD} with the z-axis. This can be converted as shown in Figure 2.7 into θ_{exit} which is linked through Snell's Law, via the Refractive Index confirmed in Section 2.3, to θ_{disp} and then θ_f.

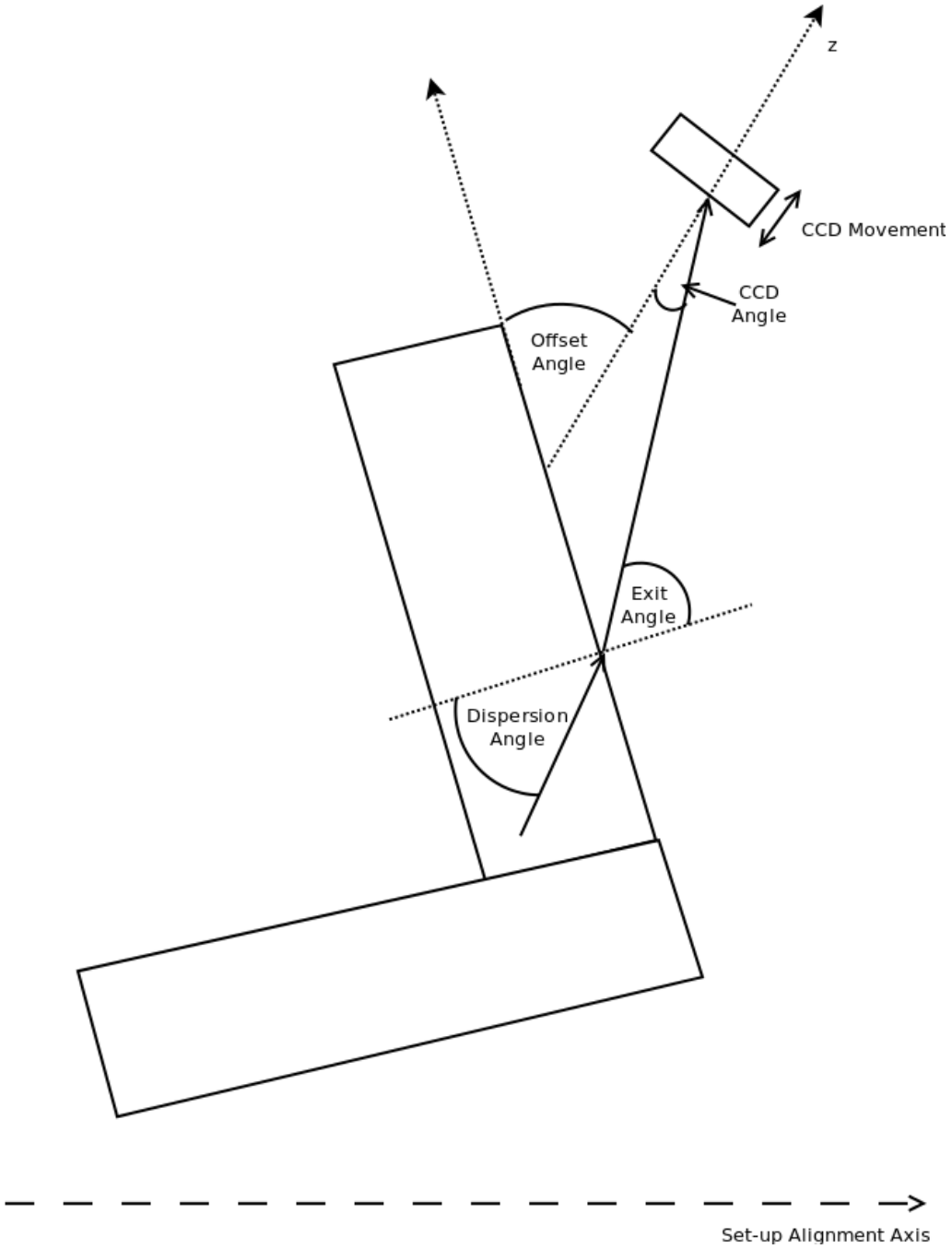

Figure 2.7: A close up of the schematic of Figure 2.6. The z-axis through the centre of the CCD, the Offset Angle, θ_{offset}, Exit Angle, θ_{exit}, and Dispersion Angle, θ_{disp} are shown. The Set-up Alignment axis was used for defining the 0° on the rotation stage.

To calculate the relevant angles after measuring the angle with respect to the CCD, θ_{CCD}, the following geometric relations are used:

$$\theta_{exit} = \theta_{CCD} - \theta_{offset} + 90^{\circ} \tag{2.4.1}$$

$$\theta_{disp} = \arcsin\left(\frac{n_{air}}{n_{SiO_2}} \sin\theta_{exit}\right) \tag{2.4.2}$$

Where both n_{air} and n_{SiO_2} are taken for the wavelength at which the measurement is carried out.

The results predicted in Table 2.2 are measured with respect to the normal to the external surface of Block 2, Figure 2.6. As the exit surface of Block 4 is orthogonal to the external surface of Block 2 the Final angle, θ_f is given by:

$$\theta_f = 90^\circ - \theta_{disp} \tag{2.4.3}$$

Examples of the spectra take and histograms of the resulting distribution are shown in Figure 2.8. Each spectrum had its x-axis projection taken and fitted with a Gaussian distribution. This gives an accurate pixel position for the x coordinate. The z coordinate is taken to be the measured displacement the CCD holding unit. These give a vector for each λ and this vector is used to calculate the θ_{disp} for that wavelength and θ_c setting.

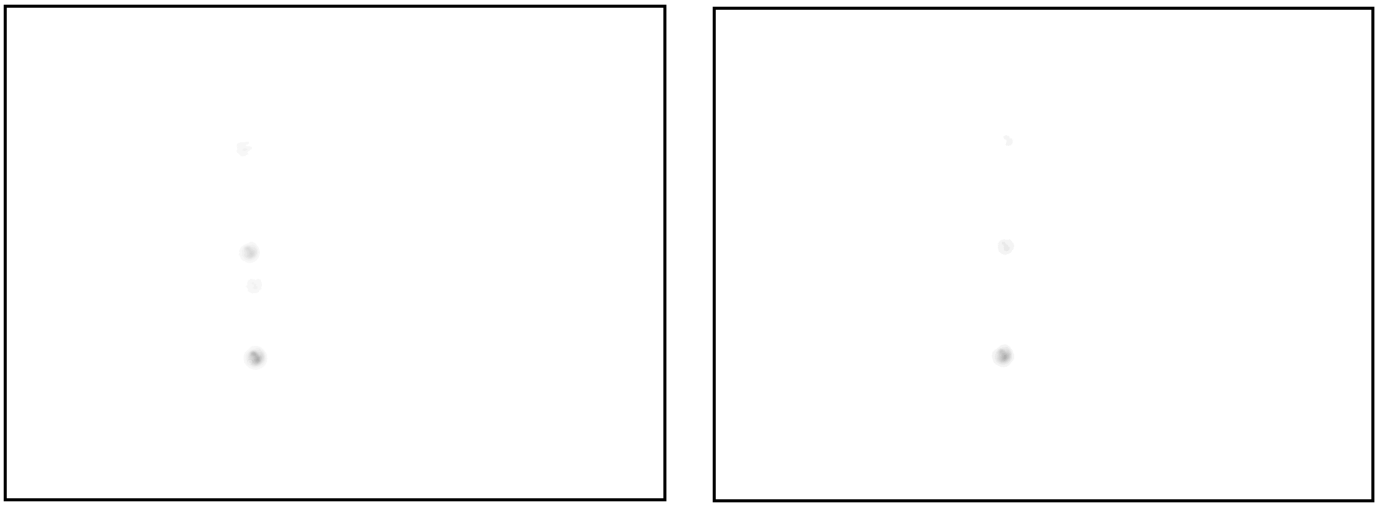

(a) (b)

Figure 2.8: Two CCD spectra from the same measurement. The signal is displaced as the CCD is moved from $10\,mm$ and $25\,mm$.

Results are shown in Table 2.3 and are grouped into the results with and without the Lithium Fluoride element. Also shown is the difference $\Delta\theta_f$ between the largest and smallest angles present, a direct measure of the Chromatic Dispersion related uncertainty that will be present in reconstructed θ_c.

2.4.2 Analysis

The observed results for θ_f in Table 2.3 can be seen to show a systematic bias of $\approx 2.6 \times 10^{-3}\,rad$ on all fused silica cases and of $\approx 2.9 \times 10^{-3}$ on all LiF cases, suggesting that the prism was misaligned by a small amount during both measurement programmes. As all of the observed values had a similar bias it was deemed to be

Table 2.3: The measured angles after being recorded on the CCD with geometric calculations included. All angles are measured with respect to the normal to the external surface of Block 2.

Material	Wavelength (nm)	Measured Final Angle θ_f (rad)	$\Delta\theta_f$ (rad)
Fused Silica	365	$0.9974 \pm 2.7 \times 10^{-4}$	$0.0111 \pm 3.8 \times 10^{-4}$
	436	$0.9925 \pm 2.7 \times 10^{-4}$	
	546	$0.9882 \pm 2.7 \times 10^{-4}$	
	578	$0.9874 \pm 2.6 \times 10^{-4}$	
	633	$0.9863 \pm 2.7 \times 10^{-4}$	
Lithium Fluoride	365	$0.9008 \pm 2.6 \times 10^{-4}$	$0.0021 \pm 3.7 \times 10^{-4}$
	436	$0.9000 \pm 2.6 \times 10^{-4}$	
	546	$0.8995 \pm 2.6 \times 10^{-4}$	
	578	$0.8991 \pm 2.6 \times 10^{-4}$	
	633	$0.8987 \pm 2.7 \times 10^{-4}$	

a systematic effect and, as $\Delta\theta_f$ is a relative measurement, it was ignored for the purposes of this comparison. The predicted and observed $\Delta\theta_f$ for both fused silica and LiF set-ups are shown in Table 2.4.

Table 2.4: The measured angles after being recorded on the CCD with geometric calculations included. All angles are measured with respect to the normal to the external surface of Block 2.

Material	Predicted $\Delta\theta_f$ (rad)	Measured $\Delta\theta_f$ (rad)
Fused Silica	$0.011155 \pm 3.146 \times 10^{-5}$	$0.0111 \pm 3.8 \times 10^{-4}$
Lithium Fluoride	$0.001761 \pm 4.024 \times 10^{-6}$	$0.0021 \pm 3.7 \times 10^{-4}$

A comparison of the predicted $\Delta\theta_f$ and those observed shows agreement within uncertainty. The presence of such a large uncertainty on the measured data is a result of the uncertainty on the measurement of θ_{offset} and in the measurement of the z-axis movement of the CCD. Both of these were at the limitations of the measurement devices used and as such the uncertainty on the data could not be further improved.

These uncertainties do not detract from the success of the Lithium Fluoride plate in reducing the $\Delta\theta_f$ value. A reduction in the angular spread resulting from Chromatic Dispersion will improve the measured resolution σ_θ. This resolution is then translated into the resolution σ_{θ_c} by Equation 1.3.7. Therefore this reduction will give an improved Čerenkov angle resolution for the a constant number of observed photons, or allow for suitable Čerenkov angle resolution with a lower number of observed photons. Taking only the observed Chromatic Dispersion as contributing to the overall σ_{θ_c} as a function of observed photons is shown in Figure 2.9.

Using the values for $N = 10$ observed photons we arrive at a maximum momentum for $\pi^\pm$ and $K^\pm$ separation of $1.453\,GeV/c$ for fused silica only and of $3.164\,GeV/c$ after the addition of LiF. The endcap region of the $\bar{\text{P}}$ANDA detector will be expected to separate particles up to $4.5\,GeV/c$ and so only the solution with LiF present will allow for suitable Focussing Lightguide Disc DIRC performance over the full dynamic range required.

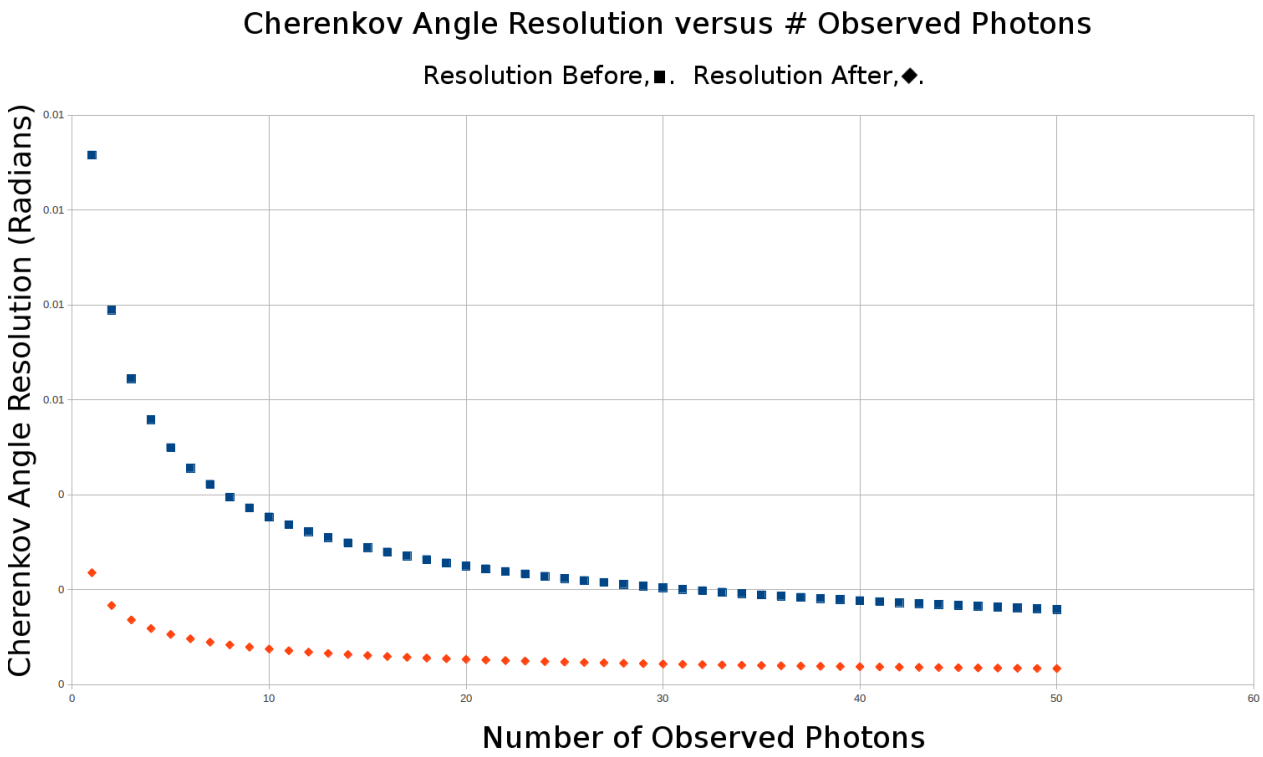

Figure 2.9: The resolution on final Čerenkov angle resulting from Chromatic Dispersion alone before and after the addition of LiF to the set-up. $N = 10$ is marked and is often quoted as the minimum number of photons required for successful pattern reconstruction.

The resolution figures given do not include impact from track deviation, due to stray magnetic fields, photon detector granularity or intrinsic multiple scattering. For LiF the latter is approximately a factor of 5 below the level of uncertainty introduced by Chromatic Dispersion, and is of greatest impact in solid materials due to the density of scattering centres. As multiple scattering for fused silica results in $\Theta_{RMS} = 0.001721\,rad$ spread, the reduction of Chromatic Dispersion by a factor of ~ 4.73 results in contributions from both that prevents the true σ_{θ_c} from being reduced as shown in Figure 2.9.

The Lithium Fluoride corrective element results in a clear improvement in the uncertainty introduced by Chromatic Dispersion. This corrective effect is replicated in an optical ray simulation of the system used to test it. The use of current models for the system performance are recommended to provide an upper limit as to the performance of the detector system. To achieve π/K separation within the momentum range required the FLDD must reduce the Chromatic uncertainty. This will not be achieved within the FLDD design without the use of Lithium Fluoride as a dispersion correction element.

Chapter 3

Initial Prototype Design & Performance

The performance of the Focussing Lightguide Disc DIRC (FLDD) will be dependent on the performance of each of its constituent components: the radiator, the dispersion correction element, the focussing lightguide (FLG) and the photon detection device. In the system of prototype development outlined in Chapter 1 it is crucial to understand each component in the final Advanced Prototype in order to understand its complete performance. A Basic Prototype was devised to test the performance and understanding of the radiator using a simple photon counting experiment.

3.1 Experimental Design

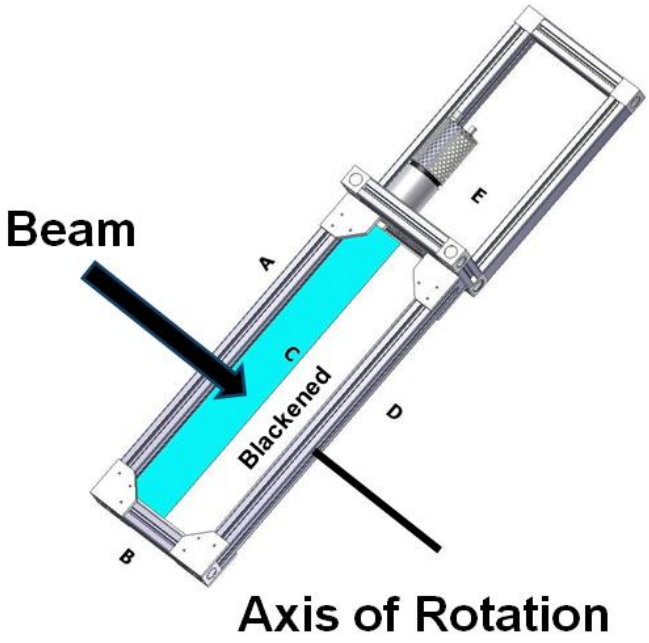

Figure 3.1: The Basic Prototype system with the fused silica radiator bar marked, blue. The axis of rotation was chosen to pass through the impact position of the beam. Sides A & B were covered in foam rubber to nullify unwanted reflections, the space on side D was filled with a black plastic bar and join C was again covered in foam rubber, the PMT is located on side E.

The design of Basic Prototype was deliberately simple. A single radiator bar of Heraus Suprasil 1, dimensions 500 mm x 70 mm x 20 mm, was connected to a 2 inch Photomultiplier tube (PMT) with a bi-alkali photocathode[1]. The bar was placed into a holding frame along side A as in Figure 3.1. A totally absorbing bar of the same dimension was placed in contact with the radiator, contacting along C. The PMT was then placed into contact with the radiator on side E. Pressure was applied along sides B and D, and to the PMT, to ensure the radiator maintained position and that a good optical contact was maintained with the PMT. Silicone based index matching fluid was applied to this contact to reduce reflection losses.

3.1.1 Radiator

Synthetic fused silica was chosen as the radiator material for its excellent transmission and radiation hardness, as well as its mechanical properties, Section 1.3.3. The transmission properties are integral to both photon production and transportation; the greater the optical bandwidth for transmission the greater the photon production and the longer the absorption length the higher the probability these photons will propagate to the edge of the detector. Excellent radiation hardness results in these transmission properties being maintained in spite of the large flux of ionizing radiation present in an environment such as the $\bar{\text{P}}$ANDA detector.

As the radiator is the base component for any Čerenkov detector it is crucial to understand and quantify how it performs in its dual role of production and transportation.

To ensure a good optical contact between the radiator and PMT a commercial silicone based optical grease. It was applied to the bar end facing the PMT and then pressure was applied to the PMT by springs to provide a good optical contact and ensuring it remained in place during data taking.

3.1.2 Photomultiplier Tube

Crucial to extracting an accurate measurement of photon yield is the accurate and precise calibration of the chosen PMT. The PMT is a 2 inch device with 12 dynode stages in a linear focussing structure. The type of PMT was selected as it provides a gain sufficient to allow for single photon resolution without need of advanced electronics to provide a strong signal. The bi-alkali cathode is beneficial as it provides an Quantum Efficiency from the near- and middle-UV range, $300\,nm - 400\,nm$ and also through visible light. It was calibrated using the Single-Photoelectron (SPE) method. A fast pulse laser system was used for the calibration and neutral density filters utilised to lower the laser intensity such that a SPE could be clearly observed. The response was studied for a supply voltage of 1900 V as it was operated at within the Basic Prototype.

The single photoelectron Gain and width, G and σ_{SPE}, were measured to be:

[1] Photonis XP2262/B

$$G = 13.35 \pm 0.075\,\text{QDC Bins}$$
$$\sigma_{SPE} = 5.762 \pm 0.23\,\text{QDC Bins}$$

and these values were then used in the quantitative analysis of the Basic Prototype data. Present on both is a systematic uncertainty of an estimated 10%.

3.1.3 Experiment

The GSI test beam constituted of primary protons of kinetic energy, $E_K = 2\,GeV$ at an angle of 14.5° to the supplying beam line. At this E_K the protons have $\beta \approx 0.948$. At this velocity $\theta_c > \theta_{crit}$ for all optical wavelengths and so detectable Čerenkov photons underwent total internal reflection. As no Čerenkov angle reconstruction was attempted, variations in θ_c with λ were inconsequential so long as this condition was met.

Table 3.1: The Basic Prototype polar angles covered during the GSI testbeam. θ_{Min} and θ_{Max} are the minimum and maximum polar angles in the final FLDD design respectively.

Polar angle, θ_p (°)	Category
-10, -7, -4, -1	$\theta_p < 0$
0, 4, 5	$0° \leq \theta_p < \theta_{Min}$
6, 10, 12, 15, 20, 25	$\theta_{Min} \leq \theta_p \leq \theta_{Max}$

The polar angles covered by the Basic Prototype test programme are summarised in Table 3.1. They are split into 3 categories: $\theta_p < 0$, $\theta_p < \theta_{Min}$ and $\theta_{Min} \leq \theta_p \leq \theta_{Max}$. These categories are each crucial to understanding the performance of the Basic Prototype. They correspond to angles which are primarily diffuse reflected, which make it to the PMT but are below the active polar angle of the FLDD and which make it to the PMT and are within the active polar angle of the FLDD.

By studying a wide range of angles, both within and outwith those for which the FLDD is designed, the test programme aimed to access information about the radiator yield and also to systematically study factors inherent to the design of the Basic Prototype. In the first regime, $\theta_p < 0°$, the produced Čerenkov photons are increasingly lost from the bar and so these angles give access to the background number of counts. By studying $0° \leq \theta_p < \theta_{Min}$ the offset of the system is estimable. The final category, $\theta_{Min} \leq \theta_p \leq \theta_{Max}$, contains the data directly pertaining to the polar angle range of the final FLDD.

The Basic Prototype utilised four trigger scintillators, in two cruciform configurations located in up and down stream of the radiator. The coincidence within each configuration and then between both configurations limits the angular acceptance associated with the incident particles. Additionally timing information was taken from each scintillator, from a separate Timing-of-Flight (ToF) scintillator and from the triggers of other experiments present at the test beam.

Timing and signal data were recorded by a VERSAModule Eurocard (VME) Multihit Time-to-Digital Converter (TDC) and Multievent Charge-to-Digital Converter (QDC) respectively.

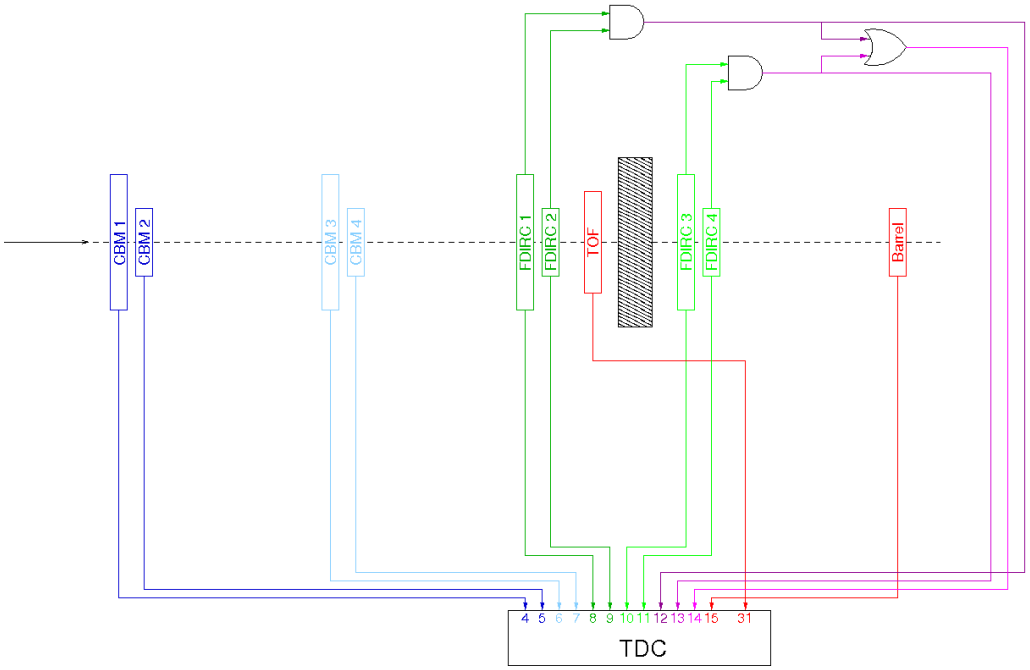

Figure 3.2: The trigger scheme for the Basic Prototype. A logical AND from either the first, FDIRC 1-2, or second, FDIRC 3-4, set of trigger scintillators was used to accept an event.

The ROOT system, a C++ based Object Oriented framework developed by CERN, was used both to encode and subsequently analyse all data from the beam time.

3.2 Data Extraction & Results

Raw data taken by the QDC and TDC required processing in order to extract the relevant parameters from which the Basic Prototype performance could be judged. The TDC unit uses a particular input channel as a reference, all other channels were compared to the designated reference channel. Extraction of the observed number of photons from the QDC spectra required particular attention and is described in detail below.

The initial concern of the data extraction process was to ensure data integrity. First the TDC data from all four trigger scintillators was taken into consideration and checked for consistency between cruciform pairs. An example of the TDC data for the front triggers before and after cutting around the central data peak is shown in Figure 3.3.

Similarly the TDC data before and after cuts for the rear triggers can be seen in Figure 3.4.

Both show clear structure within the distribution of un-cut events, attributed to the TDC reference time being defined by an accepted trigger arising from either a front or rear cruciform coincidence, Figure 3.2. These structures prevented consistent fitting of the data and so broad cuts were place manually on the distributions. As the beam energy and composition was consistent throughout the timing cuts were also consistent.

Extraction of the mean observed photons for each angle setting is a necessity. To obtain the relevant

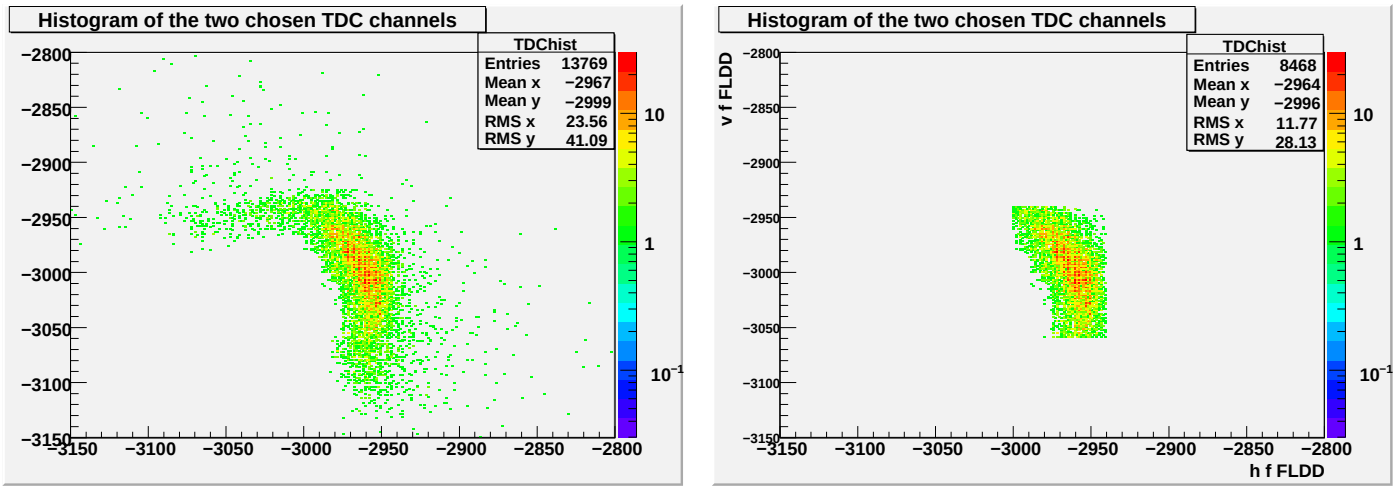

(a) TDC before cuts

(b) TDC after cuts

Figure 3.3: The TDC value for the front trigger scintillators before and after cuts

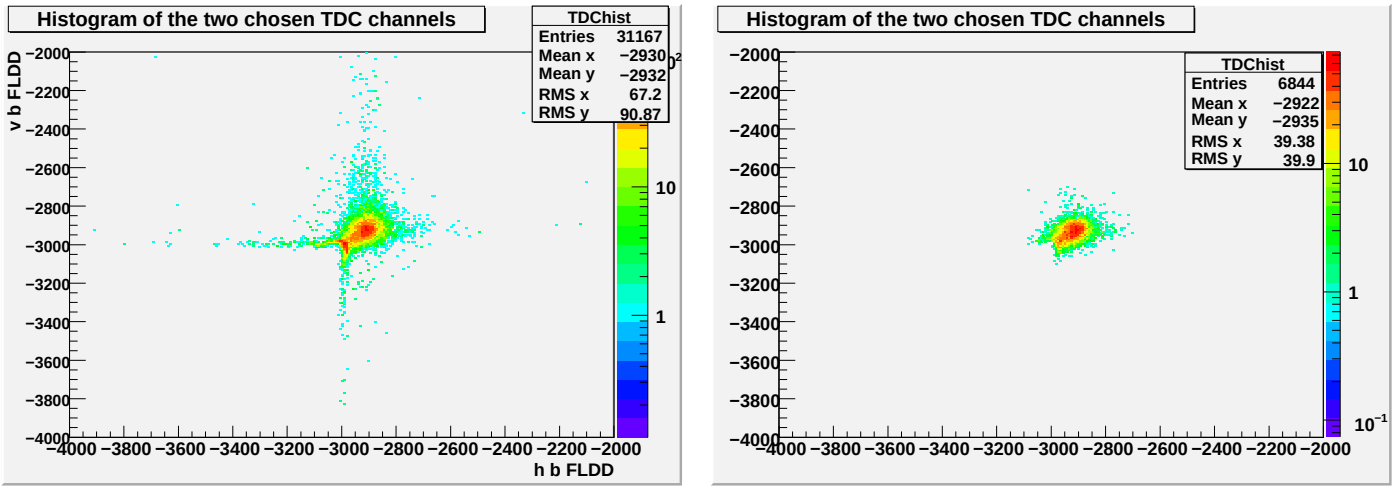

(a) TDC before cuts

(b) TDC after cuts

Figure 3.4: The TDC value for the rear trigger scintillators before and after cuts

performance parameters the response of the PMT must be well understood. For the calibration, Section 3.1.2, and final Data extraction the PMT was modelled as being the convolution of three distinct processes:

- The flux of photons incident upon the PMT.
- The performance of the photocathode and electron optics in converting photons in to photoelectrons collected by the first dynode.
- The performance of the dynode stages in electron multiplication.

The PMT response function, F, is a sum of weighted Gaussian response functions, S_j, corresponding to the response of the dynode multiplication stages to a given number of photoelectrons, with the individual weightings being the probability of occurrence of that number of photons folded with the probability of their conversion by the photocathode and collection by the first dynode stage, w_j.

This is expressed as:

$$F(x) = \sum_{j=1}^{\infty} w_j S_j(x) \tag{3.2.1}$$

$$w_j = \frac{\mu^j e^{-\mu}}{j!} \tag{3.2.2}$$

$$S_j(x) = \frac{1}{\sqrt{2\pi\sigma_j}} \exp\left(-\frac{(x-\bar{x}_j)^2}{2\sigma_j^2}\right) \tag{3.2.3}$$

where μ is the mean number of photoelectrons collected, j is the index counting the over photoelectrons, σ_j is the width of the dynode response function for j observed photoelectrons and the mean QDC value of the jth photoelectron is $\bar{x}_j$.

$$\mu = n_{ph} q \tag{3.2.4}$$

$$\sigma_j = \sigma_{SPE}\sqrt{j} \tag{3.2.5}$$

$$\bar{x}_j = \bar{x}_{SPE} + (j-1)G \tag{3.2.6}$$

where n_{ph} is the mean number of incident photons, q is the quantum efficiency of the photocathode and collection efficiency of the first dynode stage combined, σ_{SPE} and $\bar{x}_{SPE}$ are the width and mean of the single photoelectron response respectively and G is the gain of the PMT. A drawback of this fitting is its inability to account for noise contributions to the spectrum. Therefore noise in the recorded QDC spectra can bias fit results. A method of limiting this bias was used in which the lower boundary of the fit was varied and the reduced-χ^2 of the resulting fit was extracted. The fit with lowest reduced χ^2-value corresponds to the ideal value for the lower bound of the fit. By performing this reduced-χ^2 minimisation the noise contribution was also minimised.

The lower bound selected was not absolute and could be varied with each data set. Each fitting minimised the reduced-χ^2 independently and the minimised fit was chosen as final. Once the final fit was carried out the mean number of photoelectrons was taken to be mean μ, of the fit, as defined in Equation 3.2.2. The uncertainty on this value was taken to uncertainty, σ_μ, on the mean.

Once all runs at the same setting were fitted and their means extracted they were checked for consistency, Figure 3.7. A single, weighted, mean is then calculated for each setting. The weighted means for each setting were then plotted and are shown in Figure 3.8.

The results in Figure 3.8 show three distinct regions. The first region, $\theta_p < -1°$, shows a constant detection of ≈ 4 photoelectrons. The second region, $-1° \leq \theta_p \leq 5°$ shows a sharp peak at 2° descending to the constant level of the first region, below, and above to a gradient turning point at 5°. The third and final region, $\theta_p > 5°$, shows a rise in the number of observed photoelectrons up to the limit of the data at 25°.

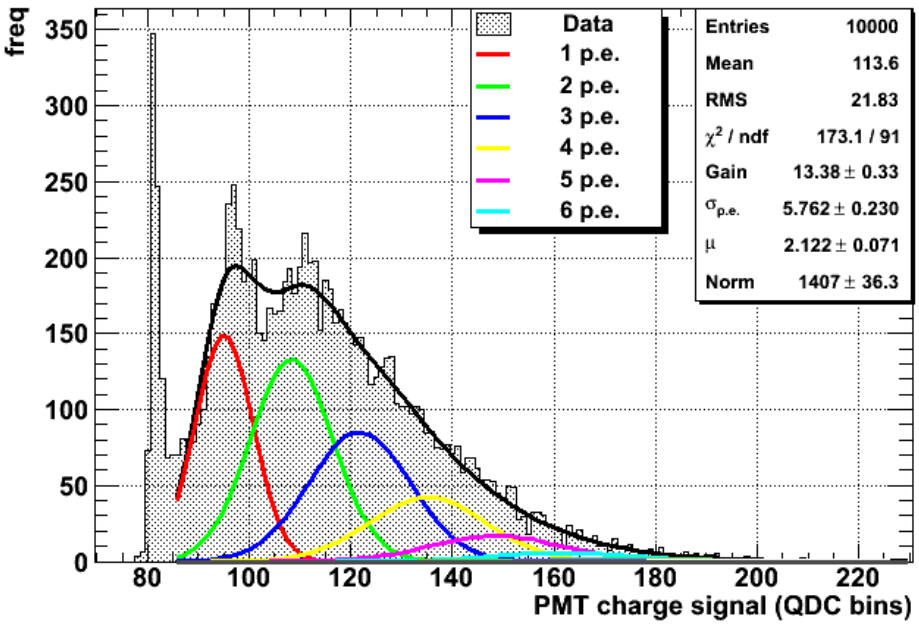

Figure 3.5: An example of the fitting algorithm with the multiple Gaussian contributions, coloured lines, and the envelope, black line. The number of photoelectrons seen follows a Poisson distribution and multiple of photoelectrons produces a Gaussian response in the detector.

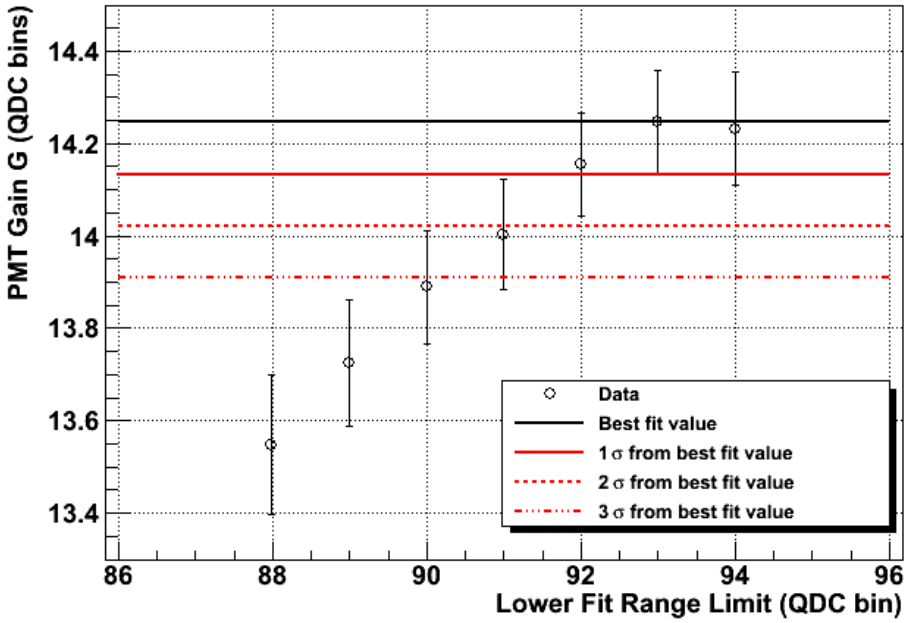

Figure 3.6: The variation in gain resulting from different lower bounds of the fitting function. The optimal lower bound for this example is seen to be a QDC value of 93.

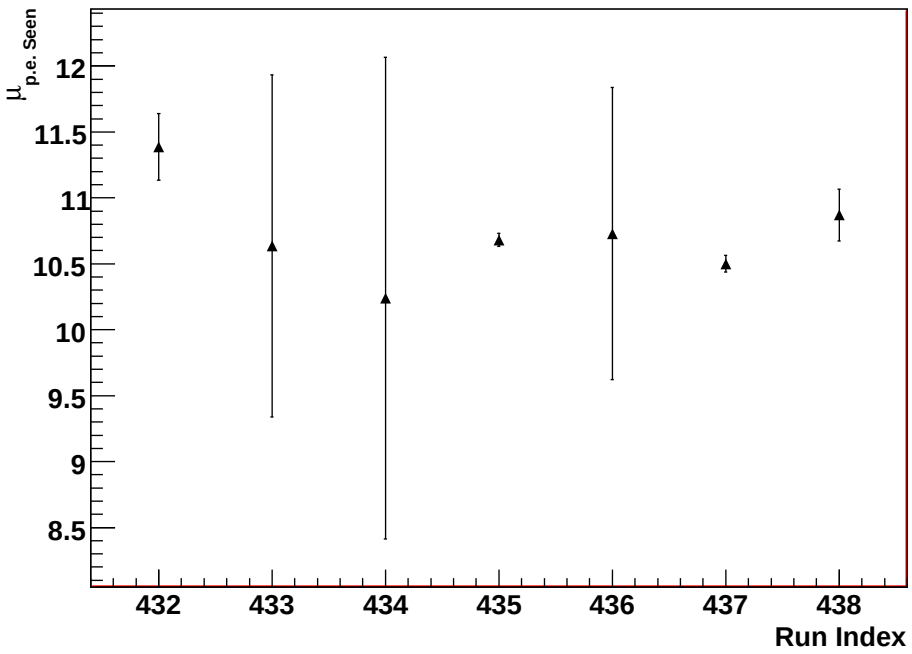

Figure 3.7: Comparison between the extracted means and their uncertainties for a single detector setting. Some runs contain many fewer events as beam delivery was not consistent and data acquisition timed out.

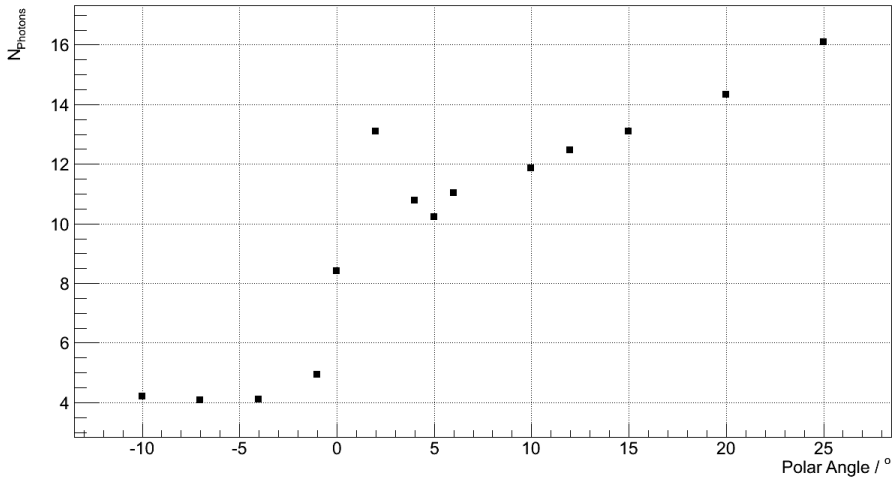

Figure 3.8: The weighted mean number of observed photoelectrons for each radiator bar polar angle setting. Statistical uncertainties obscured by the data markers.

3.3 Simulation & Analysis

Proper interpretation of the results presented in Section 3.2 requires suitable simulation of the detector set-up at the settings outlined in Section 3.1.3. The LITRANI optical simulation package, written in C++ and based on ROOT, was used to construct the simulation.

LITRANI allows the user to define non-curved geometries of optical materials, define properties of those

materials and to define detectors for the defined photons. Of particular importance to the simulation is the ability to define a beam of charged particles of a given β. This beam can then be steered through the defined materials and, should β be sufficient, the Čerenkov effect will be simulated. This allows for an accurate simulation of the photon production and transportation to the detector. The detector itself was defined to have a quantum efficiency based on the Hamamatsu H9500 which has a similar bi-alkali photocathode material. The output of the simulation was the mean number of photoelectrons as defined in Equation 3.2.4.

A crucial unknown was found to be the absorption of the side faces of the radiator, as defined in Section 3.1.1. The absorption co-efficient, η, was defined as the fraction of light absorbed by the side walls. As the foam rubber was porous it formed an imperfect contact with the side walls which allowed for reflections. These reflections then increase the mean number of photoelectrons which arrive at the detector when compared with totally absorbing side walls. The effect of greater absorption on the mean number of photoelectrons can be seen in Figure 3.9.

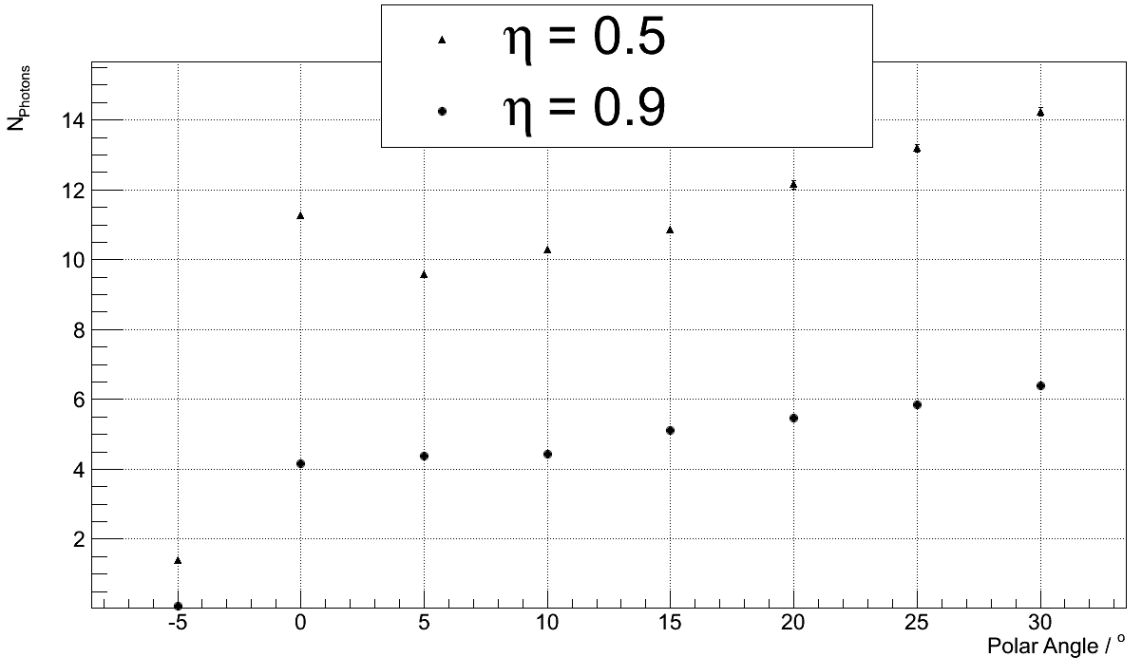

Figure 3.9: Comparison of simulated mean number of photoelectrons at $\eta = 0.5, 0.9$ for $-5° \leq \theta_p \leq 30°$ in steps of 5°.

The clear peak at 2° in the data, Figure 3.8, can only be seen at 0° for $\eta = 0.5$ in Figure 3.9. The presence of photoelectrons at $\theta_p < 0°$ within the observed data is also present only in the $\eta = 0.5$ case. Further investigation of this dependency on η was carried out for $0.3 \leq \eta \leq 0.8$ with steps of $\theta_p = 1°$. Figure 3.10 shows the mean number of photons reaching the PMT for these simulations. The peak at 0° throughout was found to be caused by the angle of photon propagation exceeding the critical angle for the entire Čerenkov cone at that setting.

Two trends are clear from Figure 3.10: first, the mean number of photoelectrons for a given angle is inversely proportional to η; second, the rate of increase photoelectrons with θ_p is greater at lower η values. The effective η value of the observed data can be extrapolated from this gradient value. This observed data from

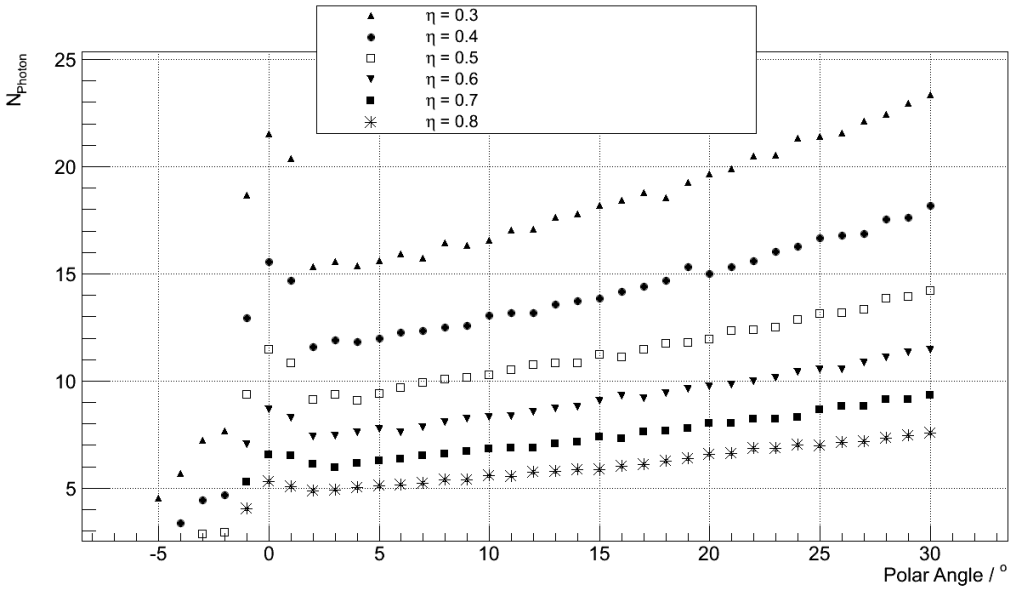

Figure 3.10: Comparison of simulated mean number of photoelectrons for $0.3 \leq \eta \leq 0.8$. The open symbol represents $\eta = 0.5$ which is carried from Figure 3.9.

Section 3.2 and simulated data for $\eta = 0.2, 0.3, 0.4, 0.5$ along with a linear fit of the region $2° \leq \theta_p \leq 25°$ for each is shown in Figure 3.11.

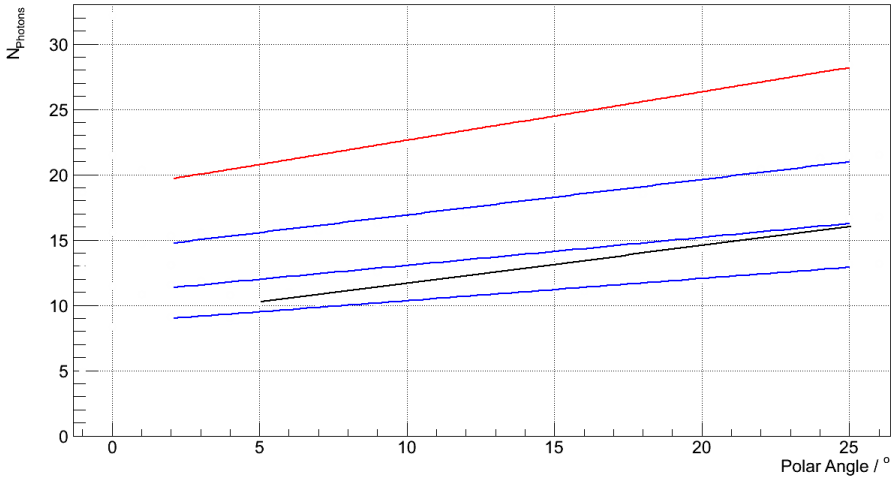

Figure 3.11: Comparison of a liner fit of Number of Photons with Polar Angle. The observed data, Black, has a greater gradient than simulated data in Blue and less than Simulated data in Red. The positions of the lines correspond to the Number of Photons for each setting.

The observed data can be seen to have an absolute value consistent with $0.5 \leq \eta \leq 0.6$ but a gradient consistent with $0.2 \leq \eta \leq 0.3$. The discrepancy between these two conclusions is a result of the difference between the simulation modelling and the observed data fitting algorithms. The first difference is that the simulation models all aspects of photon production, transportation and detection up to the production of photoelectrons, i.e. up to Equation 3.2.4. The fitting of the observed data includes these factors but

additionally requires knowledge of the photoelectron collection efficiency, the SPE gain, G, and the SPE width, σ_{SPE} to achieved the desired output. Therefore the performance of the dynode chain is unique to the observed data.

The second difference is in the number of produced photoelectrons by the photocathode. Variation in the quantum efficiency of the selected Photonis XP2262/B from that of the H9500 due to different bi-alkali material and ageing of the photocathode will result in a different number of produced photoelectrons for the same number impinging photons. The number of impinging photons is the product of the produced Čerenkov photons and the factor of these photons successfully transported to the photocathode. As fused Silica has excellent optical transmission properties, Section 1.3.3, the transportation relies solely upon geometry.

Čerenkov photons are emitted with equal probability at any azimuthal angle within the Čerenkov cone frame of reference. At $\perp$ particle incidence the Čerenkov cone projects as a circle on the downstream side of the radiator bar. An increase in particle θ_p results in a rotation of the central axis of the cone and an increase in eccentricity of the projection. This results in an increasing intersection between detector geometric acceptance and Čerenkov azimuthal angle.

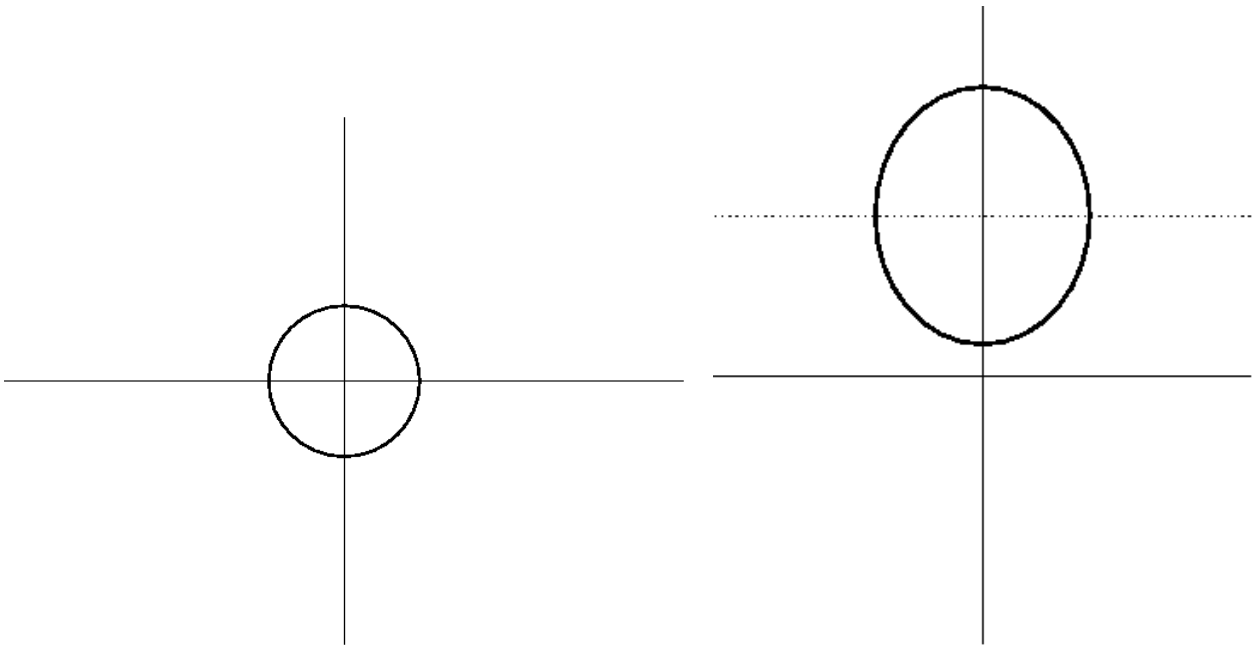

(a) Perpendicular Incidence

(b) Particle trajectory of 25°

Figure 3.12: The geometric acceptance of the radiator bar shown with Čerenkov cone projection at $\theta_p = 0°$ incidence, left, and at $\theta_p = 30°$. The central x-axis of the 30° case is shown with a dotted line.

The effective geometric acceptance of the radiator bar is summarised in Figure 3.12. Regions highlighted in green reach the PMT without striking any side wall, regions in red strike the side walls with a frequency such that fewer than one photon will reach the PMT per radian of arc subtended per particle. These values were calculated for an absorption factor of $\eta = 0.5$. The 30° case is shown for $\eta = 0.3, 0.9$ in Figure 3.13. The effective geometric acceptance can be seen to increase as η decreases.

Figure 3.14 shows the effective fraction of accepted Čerenkov azimuthal angle as a function of θ_p. The

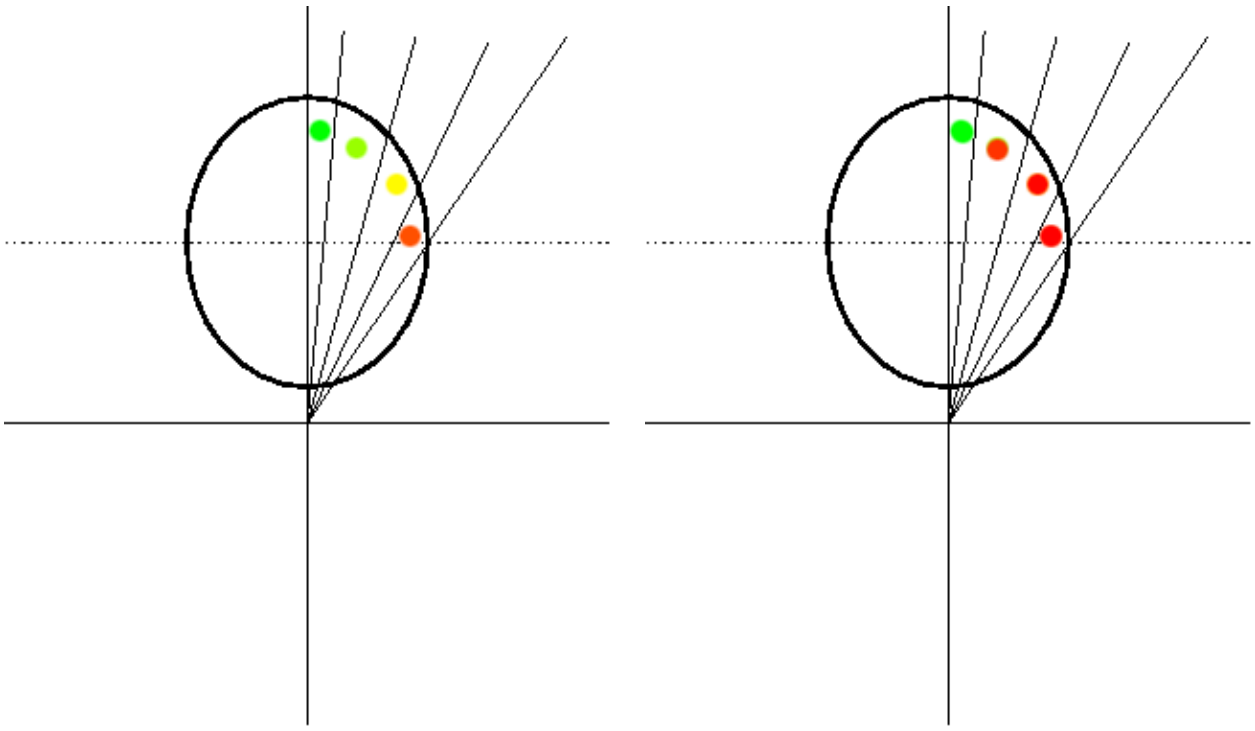

(a) (b)

Figure 3.13: Geometric acceptance of the radiator bar at $\theta_p = 25°$ for $\eta = 0.3$, a), and $\eta = 0.9$, b). Green indicates all light within that section is accepted, red indicates that no light remains at the PMT from that section. All four sections contribute for $\eta = 0.3$ but only the first 2 have significant contributions for $\eta = 0.9$.

effective azimuthal angle accepted is defined by Equation 3.3.1.

$$\phi_{eff} = \sum_{i=0}^{N} \phi_c^i \cdot \eta^i \tag{3.3.1}$$

where ϕ_c^i is the azimuthal angle subtended, in Čerenkov cone frame of reference, subsequently undergoing i bounces and N is the maximum number of bounces before the probability of photon transportation drops below one photon per radian per particle. The weighting factor $\eta^i \leq 1.0$ as $\eta \leq 1.0$ and i is in $\mathbb{I} \cup 0$. The increase in absolute value of effective accepted fraction of Čerenkov azimuthal angle and also the greater rate of increase in the region $\theta_p \geq 5°$ at lower η is clear. The structure seen in the simulated data of Figures 3.9 and 3.10 is also clear in Figure 3.14 at lower η. It is therefore clear that the primary issue within the simulation is the veracity of the η value and that it can be extrapolated by suitably fitting the region $5° \leq \theta_p \leq 30°$ in the observed data and comparing it to the fit of the simulated data.

The gradient within $5° \leq \theta_p \leq 30°$ as a function of η is shown in Figure 3.15. The corresponding gradient value of the observed data is marked and the effective $\eta = 0.27$. The reflectivity of the foam rubber used was directly measured using a Spectrophotometer and found to be $\eta = 0.2$ implying that the majority of the light should be absorbed. The large discrepancy between the directly measured and effective absorption values can be attributed to the poor optical contact between the foam rubber absorber and the side walls of the radiator bar. As a result the light was reflected at the surface of the radiator bar. An improvement in

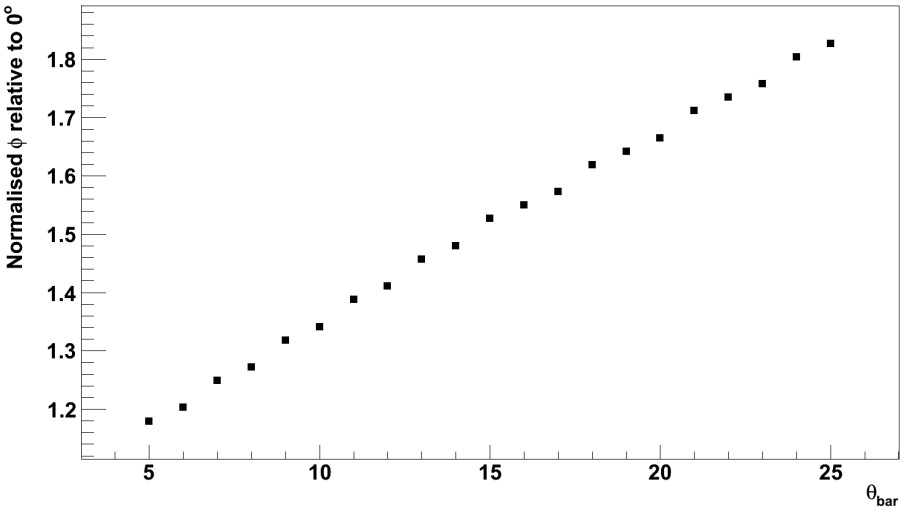

Figure 3.14: Comparison of the effective effective Čerenkov azimuthal angle, ϕ, as a function of θ_{bar}.

the optical contact is required for the effective suppression of reflected photons.

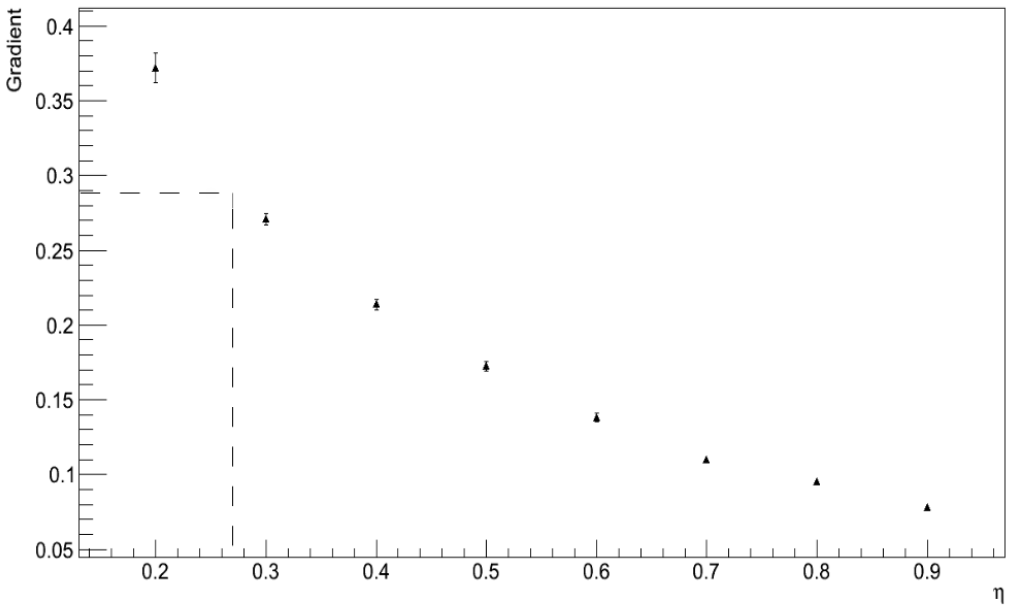

Figure 3.15: Gradient of observed photoelectrons as a function of absorption factor, η. The dashed line marks the gradient measured from the observed data and the corresponding η value.

The LITRANI simulation performed well in replicating the features of the observed data and enabled good analysis of the data taken at test beam. It was able to reproduce observed geometric subtleties and by allowing variation of side wall absorption it allowed for the extraction of the effective absorption of the Basic

Prototype.

Whilst the absolute photon production was not verified as the quantum efficiency of the PMT used was not known, the effective efficiency of the system could be extrapolated and the unknown absorption factor extracted as the simulation successfully reproduced the subtleties present in the observed data. The understanding of the system gained allows for accurate modelling and so presents evidence of the validity of development approach.

Chapter 4

Advanced Prototype Design & Performance

The prototype development for the Focussing Lightguide Disc DIRC (FLDD) has hitherto centred on the development and testing of its constituent components. An Advanced Prototype was devised to combine the two independently tested components, the radiator and Lithium Fluoride (LiF) dispersion correction element, with an example focussing lightguide (FLG) in addition, Figure 4.1. This set-up then approximates all the design features of the final FLDD.

4.1 Experimental Design

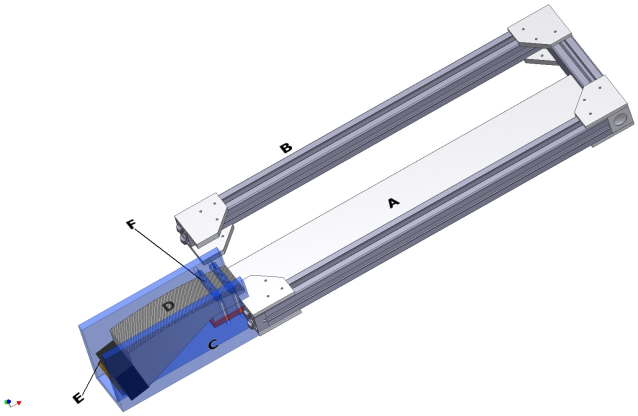

Figure 4.1: The Advanced Prototype design featuring the fused silica radiator (**A**) contained with an aluminium frame (**B**), the Lithium Fluoride corrective element and the Focussing Lightguide connect the radiator to the H9500 PMT (**E**). Contact rollers hold the lightguide in place (**F**)

The Advanced Prototype utilises the same Suprasil Fused Silica radiator component as the basic prototype in Chapter 3. Building on this familiar basis allows focus to be given to the addition of new components: the dispersion correction Lithium Fluoride (LiF) element, discussed in Chapter 2; the focussing lightguide, discussed in Section 4.1.1; and a Hamamatsu H9500 multi-anode Photomultiplier tube, discussed in Section 4.1.2.

The LiF plate was attached to the polished side of the Suprasil radiator bar, labelled A in Figure 4.1. The

focussing lightguide was then placed upon a long side of the LiF plate and the PMT subsequently attached to the lightguide focal plane. This set-up represents the components involved in the production, transportation and detection of Čerenkov photons in a radial direction within the final Focussing Lightguide disc DIRC design. In addition to radial photons, those with azimuthal angle $\phi = 0°$, the geometry of the bar retains photons of great azimuthal angle, up to $\phi \approx 47°$, which undergo total internal reflection from side walls of the bar. The presence and behaviour of photons which go on to strike the side walls of the FLG is a crucial and poorly understood element in the performance of the FLDD. These photons will be discussed in Section 4.3.

4.1.1 Focussing Lightguide

The only component within the Advanced Prototype which was previously untested was the Focussing Lightguide. The design of the FLG is based on parallel to point optics, where rays of parallel light are focused onto a single point on a focal surface, irrespective of their point of entry into the focussing optics. The FLG utilises this principle to map a given angle of propagation upon entry to the FLG onto a given row of the chosen photomultiplier. For an ideal detector all information is then encoded in the position of impact upon the focal plane.

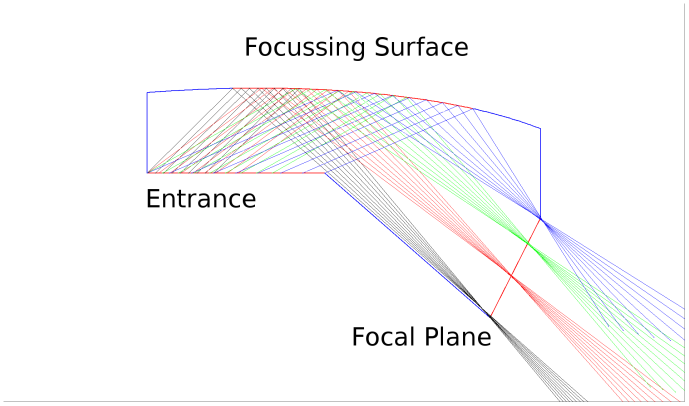

Figure 4.2: The Focussing Lightguide (FLG) design with focused rays. Each colour corresponds to a single photon angle upon entry to the FLG. Light entering at the same angle is focused onto the same section of the focal plane, irrespective of entry position.

The FLG used within the advanced prototype is shown within Figure 4.2. The reflecting surface is a polynomial section and is designed to work with a combined particle polar angle and Čerenkov production angle of $5° \lesssim \theta \lesssim 69°$. The design was to be constructed from the same Suprasil 1 material as the radiator bar for similar reasons to those outlined in Section 1.3.3. Existing methods of constructing complex shapes from fused silica and for polishing to a high standard are proposed to ensure suitable construction of the FLG.

The design of the focussing surface is dependent on the photon angles present after refraction from the LiF plate. As such the design is dependent on the interplay between the radiator material, which encodes the Čerenkov production angle, but also on the LiF corrective plate and the material of the lightguide itself.

An engineering prototype was constructed from poly(methyl methacrylate) (PMMA), commonly known as Perspex or Plexiglass. This prototype was designed to the specifications of a Suprasil design to ensure suitable construction. Due to production difficulties an optical prototype, of Suprasil, was unavailable for the test experiment of the Advanced Prototype. The engineering prototype was therefore used.

4.1.2 Photomultiplier

The final stage of any optical system is a photon detector. Of importance to Ring Imaging Čerenkov detectors are two characteristics of any suitable photomultiplier device: the granularity of the detector and its single photon detection efficiency. The former is crucial to achieving suitable resolution of Čerenkov angle and so to reconstruct β; the latter is required to ensure the detection of photons when the Čerenkov cone is spread over many lightguides. A combination of detector geometry and the intrinsic variation in photon density arising from the elliptical projection of the Čerenkov cone onto the detector results in only a few photons from some particles at some azimuthal angles making it to the photon detector. These photons can be crucial in pattern reconstruction and so in the overall resolution of Čerenkov angle.

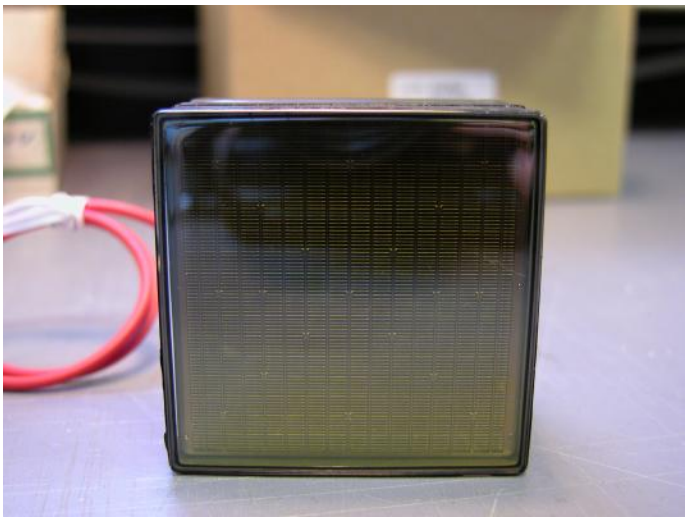

Figure 4.3: The Hamamatsu H9500 Multi-Anode Photomultiplier. It has 256 channels in a 16×16 matrix and uses a Bi-Alkali photocathode. The individual dynode chains of the PMT are clearly visible on the PMT surface.

For the advanced prototype a Hamamatsu H9500 Multi-anode Photomultiplier was used. The H9500 has dimensions of 52 mm x 52 mm x 33.3 mm with an active surface measuring 49 x 49 mm. It consists of 256 pixels arranged in a 16 x 16 matrix with each pixel measuring 2.8 mm x 2.8 mm and with a centre-pitch of 3.03 mm. The active surface of the H9500 matches closely to the design parameters of the FLDD, which envisage the lightguide having a 50 mm x 50 mm focal plane surface area. The spectral bandwidth of the H9500 is $300\,\text{nm} \leq \lambda \leq 700\,\text{nm}$ with the opacity of the entrance window, made from Borosilicate glass, causing the cut-off at 300 nm. The gain of the chosen model was 1.86 x 10^6 at a supply voltage of 1000 V.

For the advanced prototype test readout would be initially limited to 64 channels and then expanded to 128. Crucial, therefore, was selecting the correct channels to be read out. Connections were restricted by the

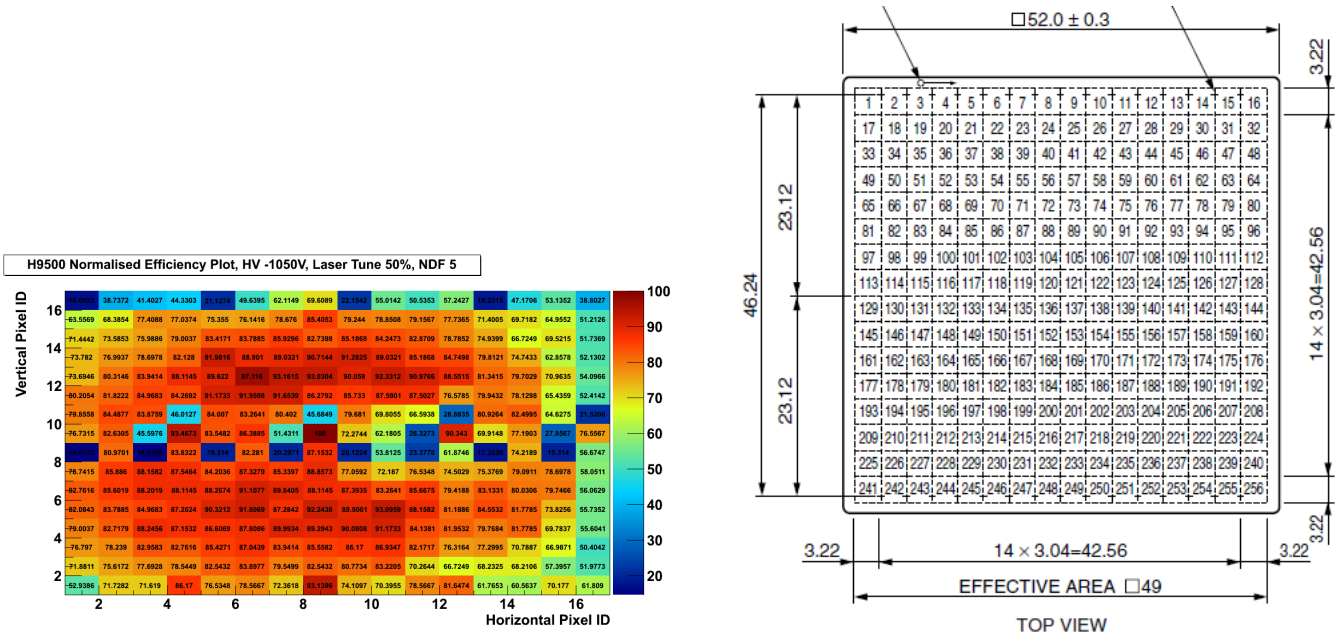

(a) Normalised H9500 Efficiency

(b) Anode Readout Layout

Figure 4.4: The relative efficiency of each channel in H9500 is shown on the left, and the anode labelling scheme is shown on the right.

layout of the signal connector output pins on the rear of the H9500, Figure 4.4(b). The 4 output connectors each read out 4 consecutive columns of the H9500, numbered 1 - 4, 5 - 8, and so on. The first 64 channels read out were taken from columns 5 - 8 as these channels showed the highest efficiency in pre-beam-time testing, Figure 4.4(a). When a second output connector was attached it was decided to connect columns 1 - 4 for two reasons: First, they showed the second highest efficiency with only the already connected columns being superior in this regard. Second, it was felt that selecting the outer columns might show any aberrations caused by proximity to the edge of the FLG, such as reflections. These could conceivably go unnoticed with only centre columns read out.

4.1.3 Data Acquisition and Experimental Layout

The Advanced Prototype was tested at the T9 beamline in the East Hall at CERN, Geneva. The facility was chosen by the $\bar{\text{P}}$ANDA Particle Identification group as it delivers a variable momentum beam of secondary mixed hadrons with similar dynamics to those which will be produced in the final $\bar{\text{P}}$ANDA detector.

Located on the CERN Proton Synchrotron (PS) accelerator, the East Hall has two targets which are fed by a $24\,GeV/c$ primary proton beam. The T9 beam line is situated on the North Target, shared with T10 and T11, and delivers secondary particles at momenta, $p \leq 15\,GeV/c$ and at a production angle from target of 0°. From the production target to the reference point, at the CERN supplied Multi-Wire Proportional Counter, is $55.81\,m$. The focal distance from this point was adjustable by the user. The beam was delivered to the target in pulses, Spills, of $\sim 300\,ms$ containing of order 10^6 particles per Spill. The Spill structure and the distribution of particles within each Spill varied.

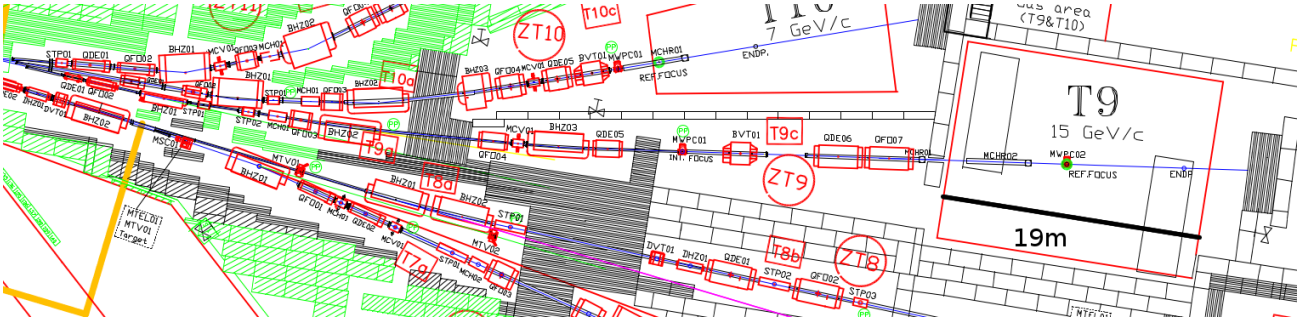

Figure 4.5: Schematic of the East Hall showing the T9 beamline showing the experimental area on the right and the production target on the left.

The data presented in this thesis used an aluminium target which resulted in the preferential production of $\pi^{\pm}$ and $K^{\pm}$ over $e^{\pm}$. The focal distance used for the data was +7.5m from the reference point throughout.

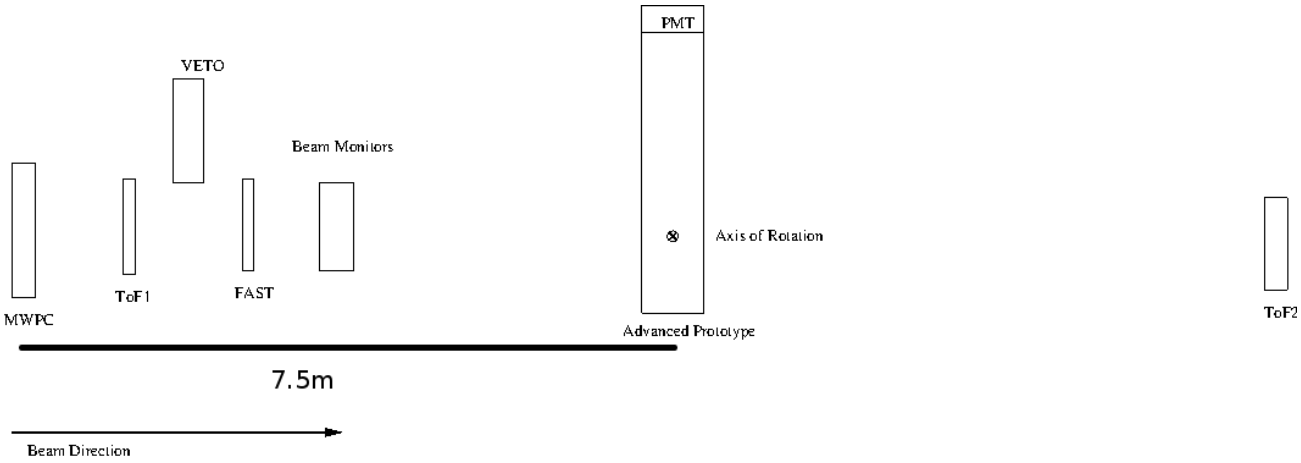

Figure 4.6: Schematic for the T9 experimental area. The beam enters from the left through the beam monitor MWPC and passes through the two trigger forming scintillators, ToF1 and FAST. The Advanced Prototype was rotated around the impact axis of the beam indicated. The final ToF2 scintillator was used to restrict the uncertainty on particle trajectory through the set-up.

The experimental set-up is shown in Figure 4.6. Shown in the schematic are:

- Multi-Wire Proportional Counter - Part of the permanent equipment at the T9 beam hall. Was not used other than as the origin of the co-ordinate system used in Figure 4.6.
- ToF1 - The first scintillation detector. It formed both the first component of the trigger system and of the Time-of-Flight system.
- Fast - The second scintillation detector. It was used in coincidence with ToF1 to form the affirmative trigger signal.
- Veto - The Third scintillation detector. It was used in anti-coincidence with ToF1 and Fast to reject events with a secondary particle incident on the Advanced prototype in a position other than that desired.

- Beam Position Monitors 1 - 4 - A set of 4 scintillators. These were used only to monitor rates during commissioning to ensure the beam had not strayed from the desired path. They were used in isolation for monitoring.
- Advanced Prototype - As outlined in Section 4.1.
- ToF2 - The final scintillation detector. It did not form part of the trigger logic but was used to calculate particle time-of-flight. It was also used during analysis to restrict solid angle uncertainty in the final data.

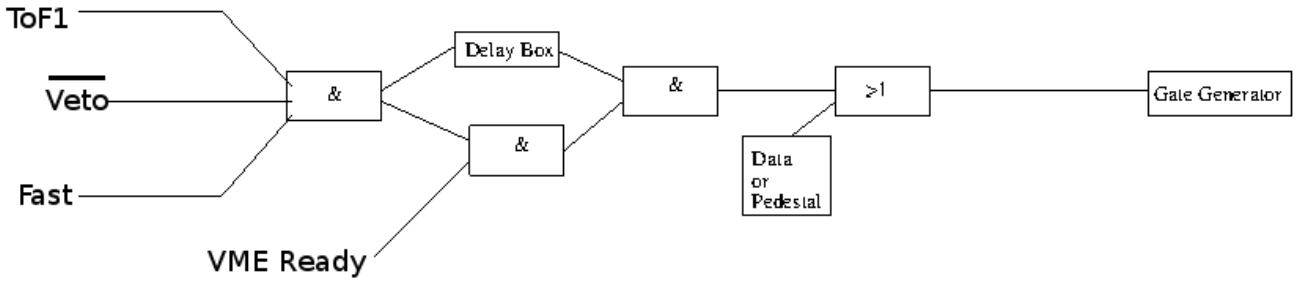

Figure 4.7: The trigger logic of the set-up. The trigger is formed by the coincidence of the ToF1 and Fast and the absence of a VETO. This trigger is accepted when it coincides with a ready signal from the QDC unit. A delay is used to give a Synchronised trigger, one which has a constant offset from the initial scintillator triggers. This final trigger then goes on to start the QDC gate generation process.

The logic for the trigger system is shown in Figure 4.7. At the first stage a coincidence is formed between the ToF1 and Fast detectors, provided there is no coincident signal from the Veto detector. This coincidence is then split, with one leg sent to a delay and the other sent to form a second coincidence with the ready signal formed when the VERSAModule Eurocard (VME) controller unit has finished processing the previous selected event. This second coincidence was combined with the delayed first coincidence such that the delayed signal would arrive last. This ensured that the timing of each selected event would be directly correlated to first coincidence. A final "OR" logic was used to allow the user to switch between external triggering, through the described procedure, or internal triggering, which allowed data to be collected without need of the beam firing the external trigger. These were then used to achieve "Data" and "Pedestal" runs respectively.

Three data taking module types were used within the VME crate: a CAEN V560 Scaler unit, a simple counter of the number of times an input fires during a triggered event; a CAEN V1290 Multi-hit Time-to-Digital Converter (TDC), used for timing measurements of every hit for each connected channel and each triggered event. 5 CAEN V792 Charge-to-Digital Converters (QDCs), used for digitising the signals from the trigger, time-of-flight and H9500 PMT detectors. The signals from the PMT to the QDC were delayed by $130\,ns$ to account for the delay in forming an accepted trigger and to allow the QDC gate to be opened. This was achieved by running the signals through an appropriate length of cable. These settings were extensively tested prior to shipment and again at CERN to ensure consistency and validity throughout.

A system of measurements was devised to cover a large proportion of the polar angles present in the final detector, to introduce azimuthal "tilt" and to vary the momentum of the incident particles. The settings

Table 4.1: The angle range covered during the Advanced Prototype test beam. The utilisation of a motorised rotation stage allowed for setting changes throughout run time.

Polar Angle, (°)	Step Size (°)	Tilt Angle (°)	Step Size (°)
0-18	0.5	0-10	1

used are summarised in Table 4.1. At a beam momentum of $p = 10\,GeV/c$ all incident particles have $\beta \approx 1$. Data at this momentum can therefore be considered to give a "clean" signal allowing calibration and comparison. Many of the angular settings were also taken at $p = 4\,GeV/c$ which is close to the upper limit of the dynamic range expected for the final FLDD. A few settings were also then taken at $p = 1.5\,GeV/c$ as the beam composition was comprised largely of $\pi^{\pm}$. At this lower momentum the β of a $\pi^{\pm}$ is close to that of a $p = 4\,GeV/c$ $K^{\pm}$.

Throughout the measurement programme a system of "sandwiching" data run sets with pedestal runs was employed. Such frequent background readings allows for regular checks on background consistency and for accurate pedestal subtraction from the data. In addition the system allows the clear affiliation of background measurement with data runs, allowing a subsequent background fitting and subtraction for each data run. For a beam with $p = 10\,GeV/c$ the data rate was such that a 1 - 5 - 1 system of Pedestal - Data - Pedestal runs was used. At lower p the data rate was such that a system of 1 - 1 - 1 was used instead.

4.2 Data Extraction & Results

Only through detailed study of all the data available data can final results for the Advanced Prototype, and so conclusions for the full FLDD design, be obtained. The ROOT system was used both to encode and subsequently analyse all data from the beam time. This framework contains a number of tools for the presentation and analysis of a wide variety of high energy physics data.

4.2.1 Data Output

The primary data handling object within ROOT is the Tree. A Tree binds together a pre-defined group of data sub-sets, called Branches, and each Branch contains Leaves of a given data type, such as Integer or Floating Point. The data taken by the Scaler, TDC and QDC units were then be placed into a single Tree object and subsequently analysed. The utilised branches of this raw data Tree were:

- Run Number - incremented each time the Data Acquisition system took a run of data.
- DAQ Setting - a binary flag to indicate an Internal trigger. Pedestal, run or and external trigger, Data, run.
- Event Number - the number of a given event within the run.
- QDC Location - the QDC channel number. This spans all QDCs connected in one index, ranging from 0-95 for 4-Column runs and 0-159 for 8-Column runs.

- QDC Value - the event-by-event reading from the QDC. The event rate varied with beam momentum setting.
- TDC Location - the TDC channel number.
- TDC Value with respect to reference value - even-by-event timing of each signal arriving into the TDC and displayed relative to a reference signal. The TDC times the arrival of both the leading, first, and trailing, second, edge of the input signal.
- TDC Edge - Correlates TDC value with the leading or trailing edge of the timed signal.
- Scaler Location - the Scaler channel number
- Scaler Value - event-by-event reading of the number of hits in a given channel.

In addition the total number of entries presented from each VME unit was recorded. This output framework is based on that used in Basic prototype in Chapter 3.

4.2.2 Timing Calculations

Utilising the data available fully required an analysis system which made use of both primary and derivative quantities. An outline of the stages involved in the process is given in Figure 4.8.

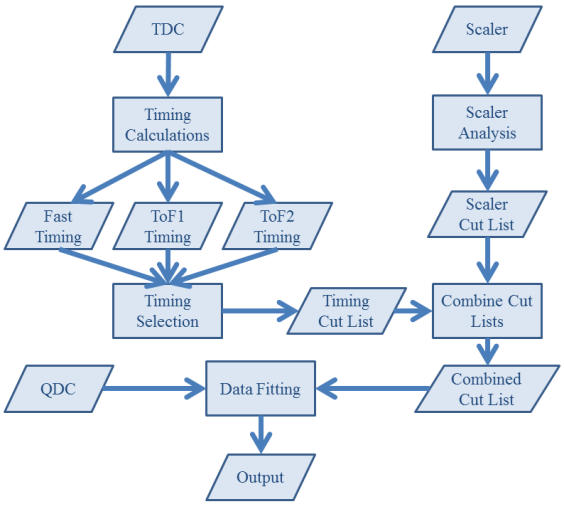

Figure 4.8: Flow Chart outlining the stages of the data analysis. Each process was checked across the data range to ensure consistency of selection rules.

The first stage of the process was to calculate the derivative timing quantities required for the further analysis stages. This section of the analysis used data from the V1290 TDC unit and the V560 Scaler and calculated: the number of events in a given Spill - a distinct group of arriving particles, Spill Index; the number of a given event within a Spill, Spill Event Index; the length of the Gate for a given event, Gate Length; the time-of-flight between the ToF1 and Fast scintillators, ToF Short; the time-of-flight between the ToF1 and ToF2 scintillators, ToF long; the timing of Raw coincidence trigger, Trigger Timing; the timing of each of

the ToF1, Fast, Veto and ToF2 scintillators, ToF1, Fast, Veto and ToF2 Timing; the timing of the Accepted Triggers i.e. those where the DAQ system is ready, Accepted Timing; the timing of the Synchronised Trigger i.e. Accepted triggers combined with the delayed raw trigger, Synchronised Timing; the timing different between the Raw trigger and the ToF1 and Fast scintillators, Raw to TOF and Raw to Fast; the timing difference between the Raw and Accepted triggers, Raw to Accepted; the length of the ToF1, Fast, Raw Trigger and Final Trigger signals, ToF1, Fast, Raw and Final Length.

Table 4.2: The recorded data and subsequent derivative quantities.

Electronics Module	Primary Data	Derivative Quantities
TDC	Leading Edge timing	Scintillator Arrival Times Logic Arrival Times Timing Differences Between Signals
	Trailing Edge Timing	Lengths of Signals
QDC	Pixel Observed Signal	N/A
Scaler	Number of hits per channel per event	Spill Event Index Spill Index

As the TDC used was multi-hit the first stage of data extraction was to associate entries with the input channel which caused the entry. This is done because timing signals will arrive in no set order, the first scintillator need not be the first signal to arrive nor need it be recorded in the same position from event to event. Additionally there may be multiple entries per channel and these could intersperse data from other channels. From the correctly associated data it was then possible to calculate all the derived quantities listed in Table 4.2.

4.2.3 Data Selection

Proceeding from the timing calculations in Section 4.2.2 it was possible to make selections to ensure the quality, consistency and, firstly, integrity of the data to be used in the final analysis of the Advance Prototype. The study of the timings taken by the TDC is the first step in this process.

The Accepted and Synchronised triggers, Figure 4.7, should show a variable offset depending on the arrival of the QDC ready signal. The resulting distribution is shown in Figure 4.9(a). Four independent peaks can be clearly observed, projecting to two in each of the Accepted and Synchronised data. As the peaks are independent it was taken that the cause affected each timing channel separately. A study of the Synchronised timing as a function of the passage of real time elapsed, Figure 4.9(b), shows no systematic correlation within the trend. Both peaks are present throughout.

As the timings were measured relative to the end signal of the gate generator the impact of varying gate length on Synchronised trigger timing was investigated, Figure 4.10(a). Both peaks present in the Synchronised trigger are shown to be present irrespective of variations in gate length. The timing distribution of the Fast scintillator was taken in isolation and shows 2 clear peaks. The contributions to these peaks resulting from each of the 4 independent peaks in Figure 4.9(a) were overlaid and show no clear correlation. As each

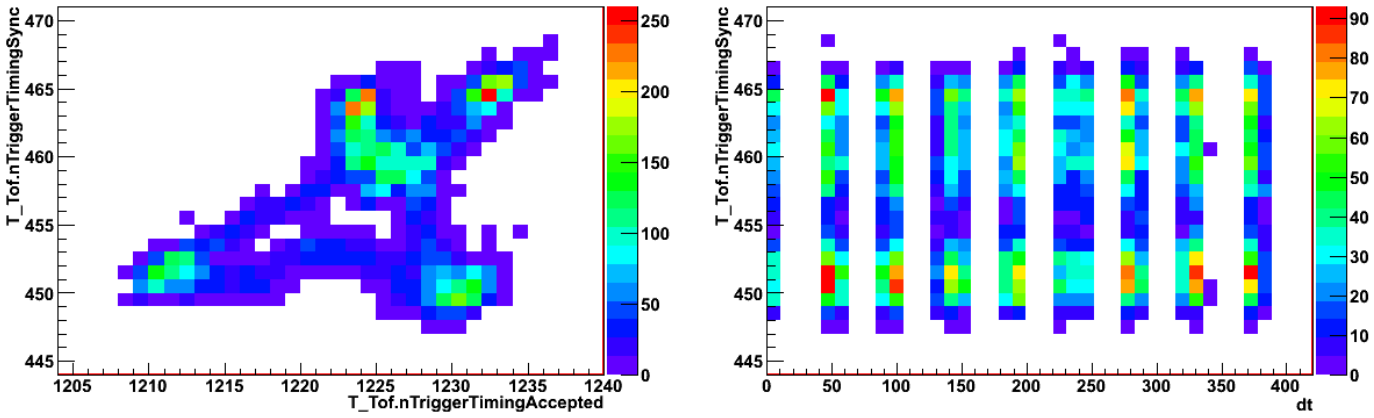

(a) (b)

Figure 4.9: The time structure of the accepted triggers versus the synchronised triggers is shown on the left. The Synchronised trigger time plotted against the time elapsed since the beginning of the data run is shown on the right.

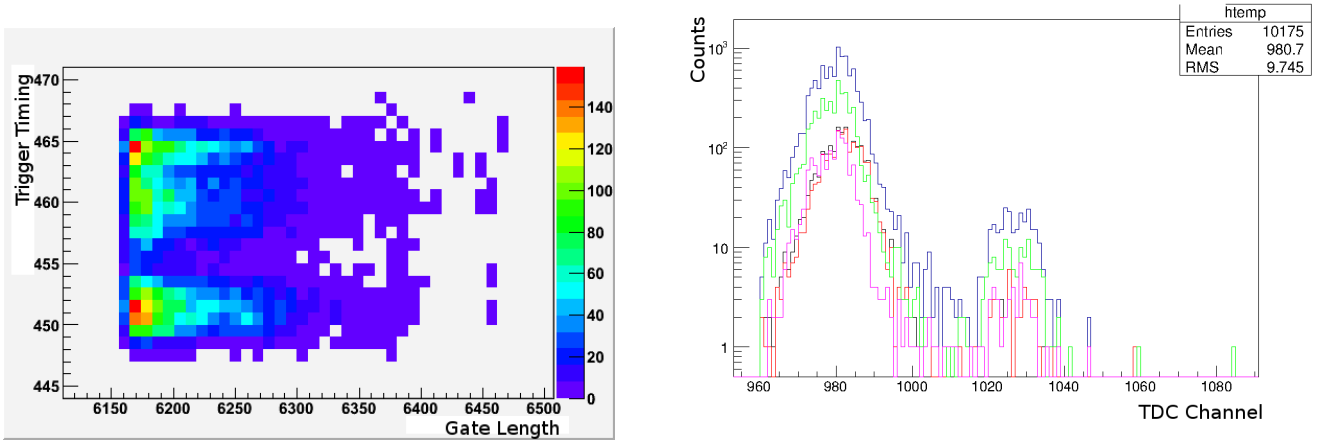

(a) (b)

Figure 4.10: The Synchronised trigger timing is shown against the measured length of the Gate for the QDC is shown on the left. The timing of one of the trigger scintillators is shown on the right. The overlay histograms in green, red, purple and black, each correspond to one of the four peaks shown in Figure 4.9(a).

separate stage of the logic has shown its own independent twin-peak structure it was considered an artifact of the timing chain and not inherent in the trigger logic passed through the system. An investigation into a single QDC signal channel was carried out the confirm this and is shown in Figure 4.11.

It is clear that each peak shows no correlation to either higher or lower QDC values. The discrete splitting of trigger propagation times did not result in a systematic alteration of the signals observed through the QDC and as such no correction for this effect was applied. As each separate component within the logic system showed independent peaks it was taken to be an artifact introduced between the logic signal production and

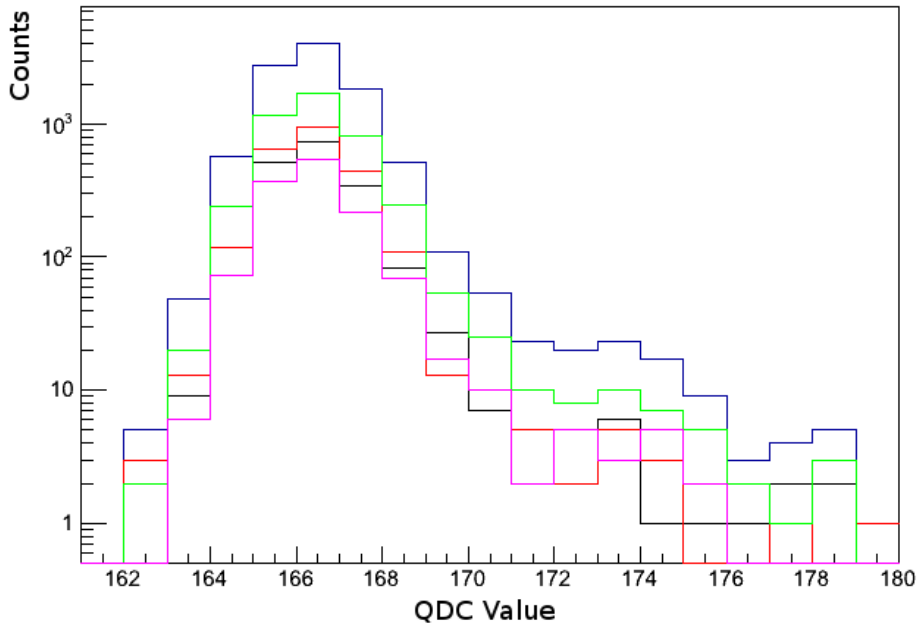

Figure 4.11: An example QDC channel spectrum shown with an overlay of the contributions to the signal arising from events located within each of the 4 peaks visible in Figure 4.9(a).

the TDC digitisation, and so was independent of the QDC trigger or data chain.

Following these steps resulted in the removal of anomalous events and spurious signals from the data stream and so it was then possible to impose cuts which ensured the quality and consistency of the data. The first of these was to ensure that the time with respect to reference of each of the ToF1, Fast and, if requested, ToF2 scintillators were fell within the primary distribution for each detector. As this distribution is correlated to a fixed reference time, events falling within it were correlated with the particle which caused the trigger condition.

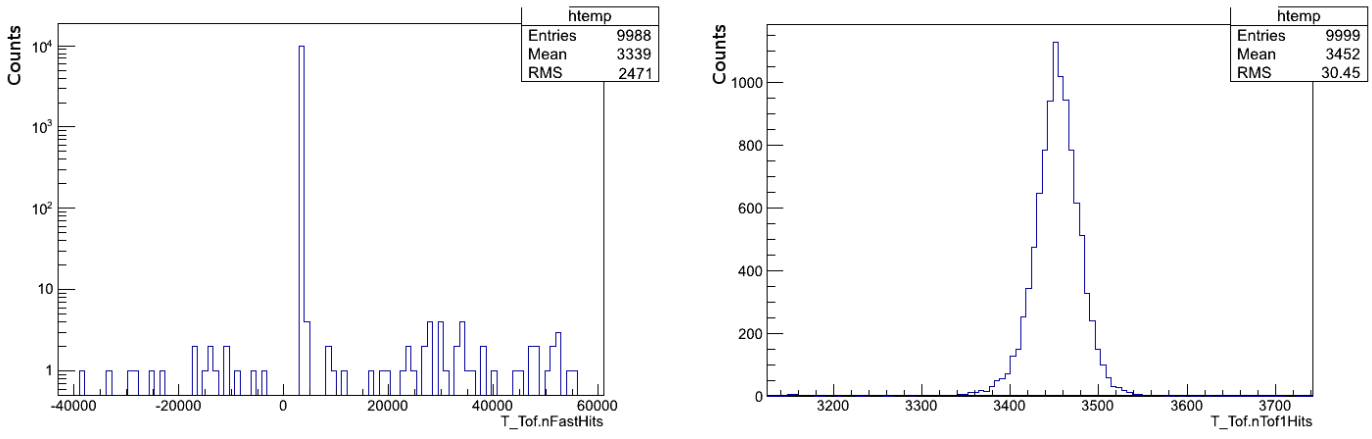

(a) (b)

Figure 4.12: Timings for the ToF1 scintillator showing a full spectrum, left, and a spectrum constrained to show the primary distribution.

An example of a raw ToF1 spectrum can be seen in Figure 4.12(a). Some events can be seen at extreme times relative to the clear main distribution centred around channel 3330. If the upper and lower limits on the time are constrained to show the details of the main peak we can see a distribution which can be approximated as Gaussian Figure 4.12(a). As this distribution was clean from background events, an indication of a low particle rate, an automated Gaussian fitting algorithm was used within channels 3000 to 4000.

The selection criterion was $t_{event} = \mu_{Gaus} \pm 3\sigma$.

A similar process was used for the Fast scintillator.

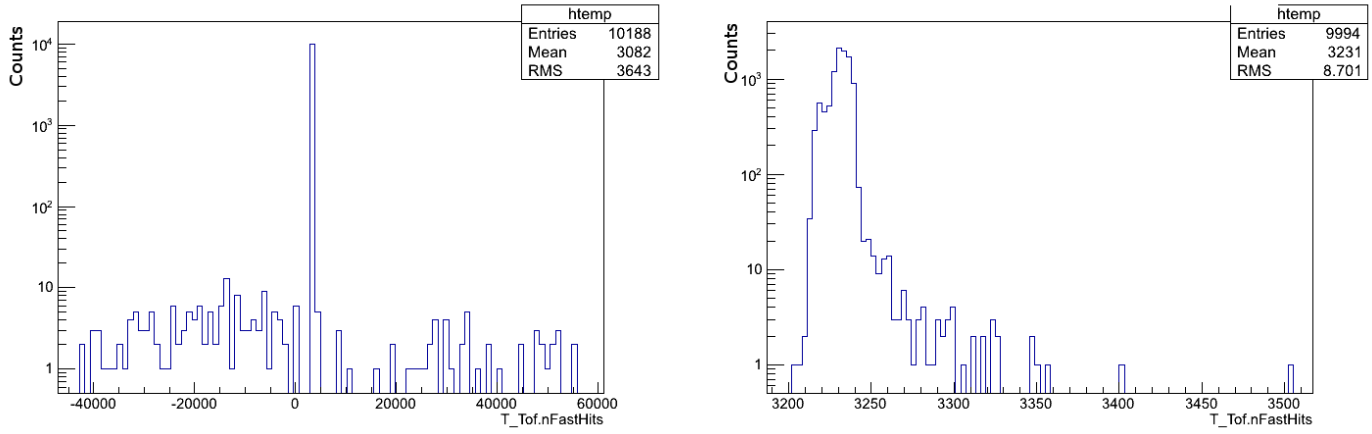

(a) (b)

Figure 4.13: Timings for the fast scintillator showing a full spectrum, left, and a spectrum constrained to show the primary distribution.

This process was used finally on the Raw trigger logic, Figure 4.14.

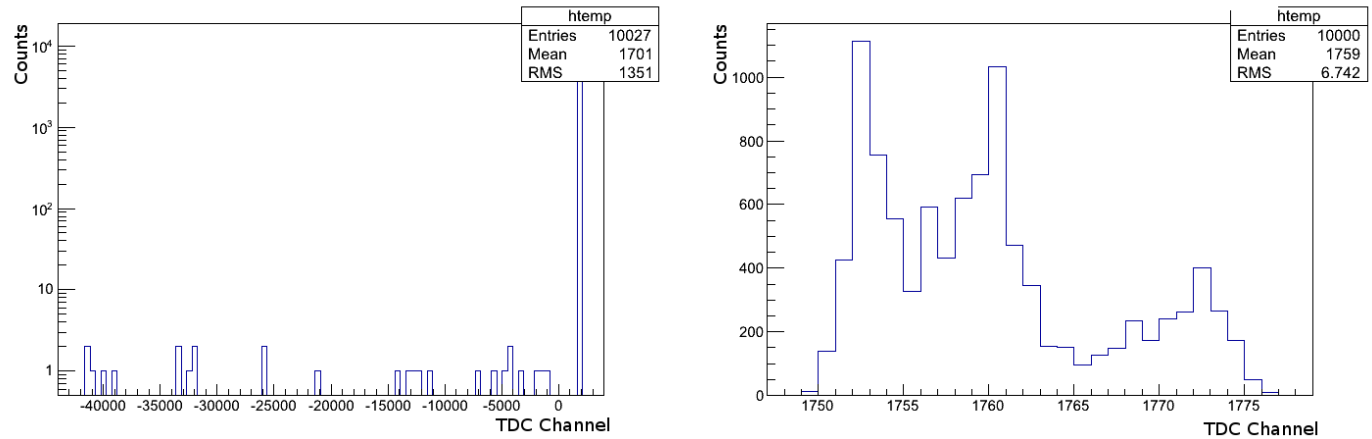

(a) (b)

Figure 4.14: Timings for the raw trigger showing a full spectrum, left, and a spectrum constrained to show the primary distribution.

The Raw trigger logic timing spectrum is appreciably different to both the ToF1 and Fast scintillators as it was used as part of the trigger logic. The trigger system was constructed and timings calculated such that all

accepted triggers would show a positive TDC reading. This allowed for a simple cut to be placed restricting the domain of the Raw trigger to positive TDV values.

Selection cuts were also placed on the number of times a given channel was allowed to have fired within a given event. For data runs it was required that: there was at least 1 raw coincidence, there was exactly 1 accepted trigger, there was exactly 1 synchronised trigger, there was exactly 1 QDC gate start signal and there was exactly 1 QDC gate end marker signal. This ensured we only deal with events which fire all stages of the trigger scheme as designed.

For pedestal runs only the QDC gate was used. This allowed a measure of the background signal across all QDC channels simultaneously and in-situ.

Each of these selection cuts produced a ROOT TEventList object containing a set of the number of every event which pass each of the selection criteria. The intersection of all of these sets was then taken and contained only those events which were selected by all selection criteria.

4.2.4 Data Extraction

Run by run data was selected as outlined in Section 4.2.3 and the selected data was used subsequently as the basis for further analysis. Each Data run was then associated with the neighbouring pedestal runs as defined by the measurement programme, Section 4.1.3. These backgrounds were then checked for consistency, fitted and then subtracted from the data runs to access the signal events present in the data.

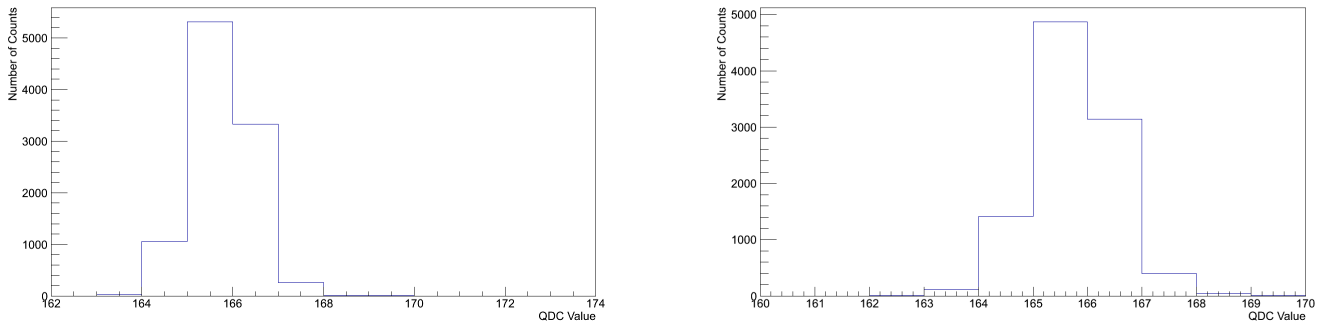

(a) (b)

Figure 4.15: Pedestal distributions for the background runs either side of data runs.

The first stage in this process was to compare the spectra of both pedestal runs to ensure the background was self-consistent. This was achieved by fitting both spectra with Gaussian distributions, Figure 4.15, and comparing these fits. If they agreed within 1σ then they were combined into a Chained ROOT object. A Chain allows the combination of Tree objects into a single, combined, Tree. For practical purposes this sums the data from each Pedestal Tree such that the resultant Chain will have the total number of entries from both contributing pedestal runs.

The chained data can then be fitted in the same way as a single tree of data. The combined pedestal data is then fitted with a Gaussian distribution, Figure 4.16, and the amplitude, mean and σ of this distribution

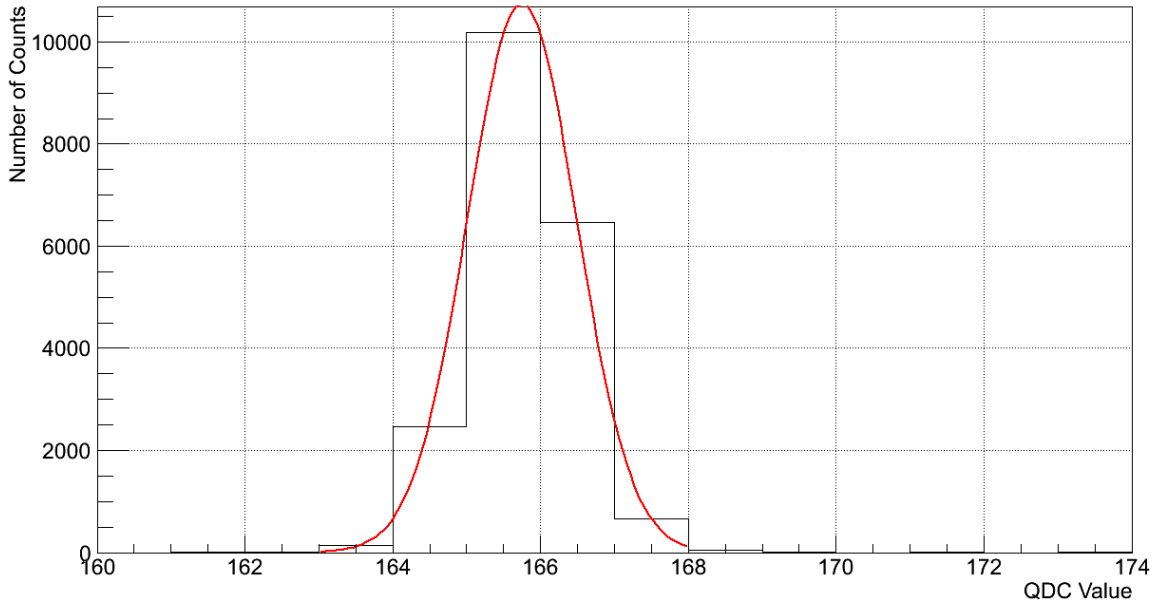

Figure 4.16: If the mean of the two sandwich pedestal runs agreed they were summed, a process known as "chaining". The resulting distribution was then fitted with a Gaussian distribution as shown in red.

extracted. A new Gaussian distribution is then defined with these parameters. This distribution is then fitted to the leading edge of the Data run spectrum, limited to the region of the spectrum up to and including the mean of the combined Pedestal spectrum. This constraint is required as the Data spectrum will have signal events at values greater than the Pedestal and this would skew any fit for subtraction purposes. The constraint is valid as the Pedestal represents the lower bound for output from any given QDC channel, therefore the leading edge is not skewed by additional data at QDC values lower than pedestal. The amplitude, mean and σ of this constrained fit are then extracted.

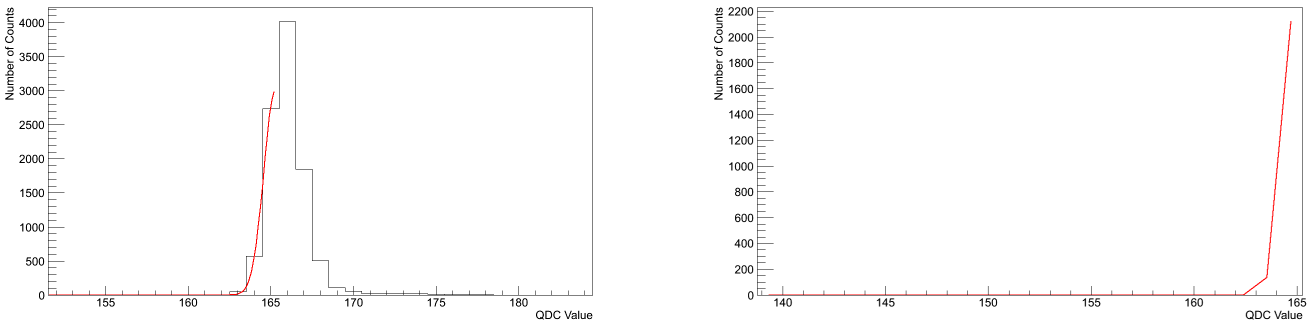

(a) (b)

Figure 4.17: The spectrum with leading edge pedestal fit in red, left, and the resulting left half-Gaussian function from this fit, right.

The parameters from this constrained Gaussian are then extracted, Figure 4.17, which is the subtracted from the signal spectrum. The resultant value is the residual signal, with background subtracted. This procedure

is carried out for each QDC channel in turn. As this method is constrained to the rising edge of the pedestal, pedestal trailing edge events are still included in the resulting spectrum.

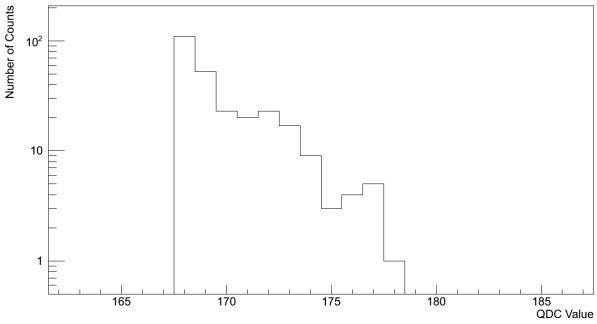

Figure 4.18: The spectrum with 5-σ cut is shown with a logarithmic y-axis to show the signal "bumps".

To remove the remaining pedestal events from he signal the a cut was imposed removing events within the Gaussian distribution, as defined above, that fell within $\pm 5\sigma$ of the pedestal mean, Figure 4.18. The remaining events are then summed and taken to be the total number of signal events for that QDC channel within that data run. It is these vales that are used throughout the remaining analysis.

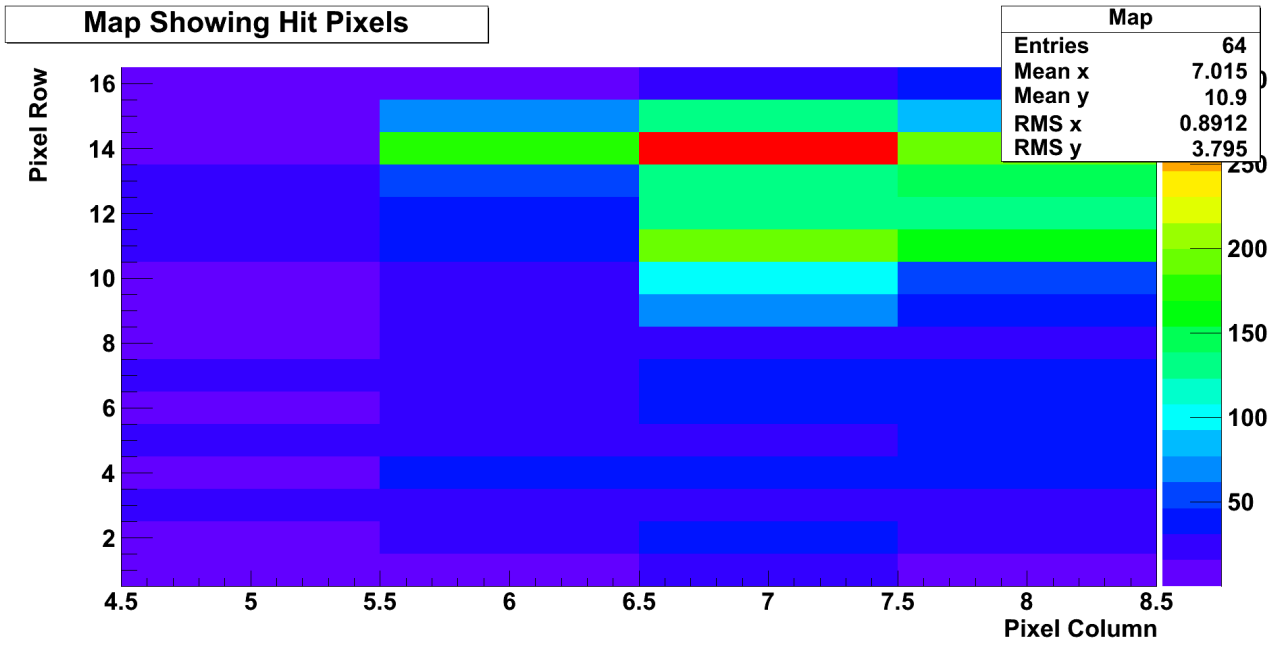

Figure 4.19: An example of the Heat Map histogram system. This example is data taken at $10\,GeV/c$ at $\theta_p = 18°$.

Each of the background subtracted spectra are then sorted into their respective detector and beam settings e.g. $p = 10\,GeV/c$, $\theta = 10°$, $\phi = 0°$. The number of events remaining in each QDC channel of the subtracted spectra were then taken and associated with the pixel the data corresponds to as outlined in Section 4.1.3. The average remaining signal from runs at a given setting was then taken for each pixel. This data was then mapped on a 2-D Histogram "Heat Map" showing each pixel and the remaining signal clearly, Figure 4.19.

4.2.5 Results

Studies were carried out using the measurement programme outlined in Table 4.1. At first each angle setting was taken using a beam momentum of $10\,GeV/c$ as this predominantly contained particles with a velocity of $\beta \approx 1$. These were then compared to data taken with a beam momentum of $4\,GeV/c$ at the same angle setting and the results compared. It was noted that the top left sector quadrant, Columns 4 and 5 and Rows 9 to 16, had induced line noise which obscured the signal striking pixels in the quadrant.

Figure 4.20 shows the results taken at an angle of $\theta_p = 18°$ for both momenta.

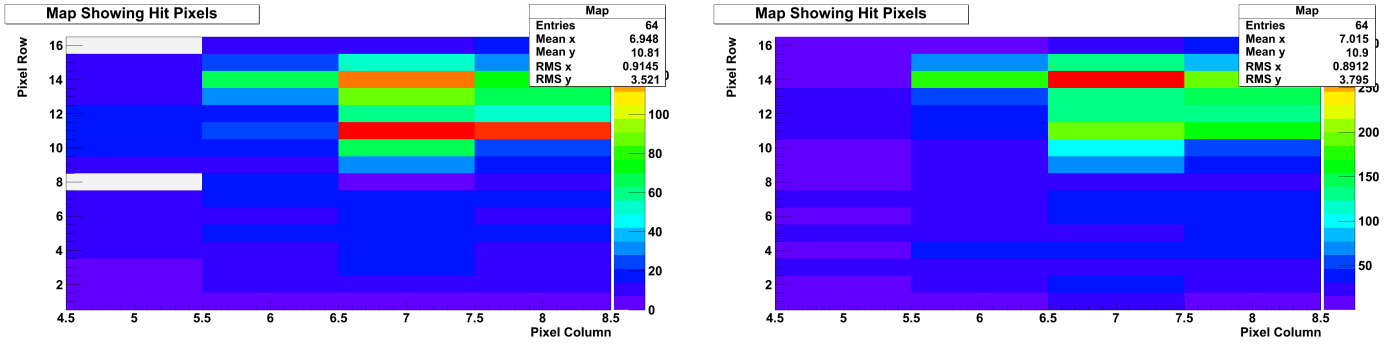

(a) (b)

Figure 4.20: A comparison of the data taken at beam momentum $4\,GeV/c$, a), and $10\,GeV/c$, b), with a polar angle of $\theta_p = 18°$.

A small difference in the mean can be clearly seen with the $4\,GeV/c$ events striking the PMT closer to the bottom of the face. Both also show a splitting of the signal across two distinct pixel rows, Rows 11 and 14. Similarly the signals at $\theta_p = 10°$ were compared in Figure 4.21.

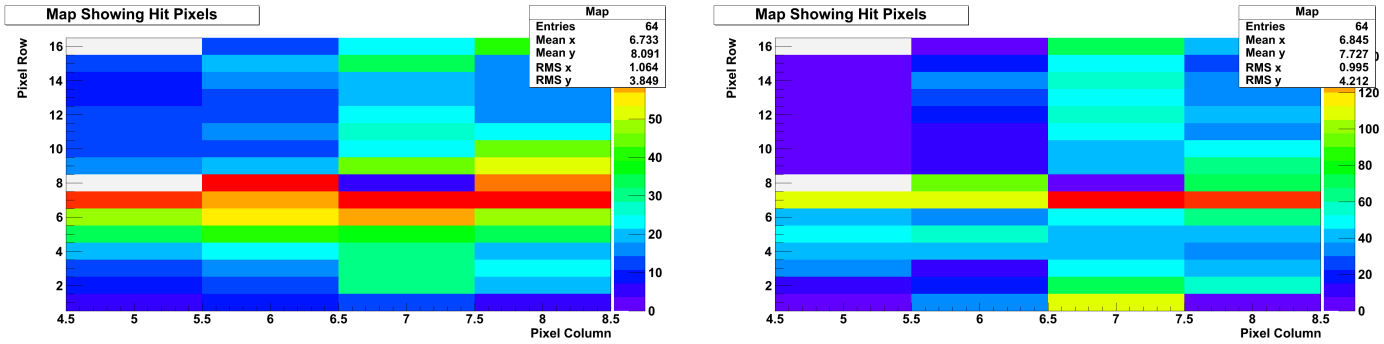

(a) (b)

Figure 4.21: A comparison of the data taken at beam momentum $4\,GeV/c$, a), and $10\,GeV/c$, b), with a polar angle of $\theta_p = 10°$.

The signal for $\theta_p = 10°$ at a beam momentum of $10\,GeV/c$ is located on primarily on a single pixel row, no split signal is observed in Figure 4.20. The $4\,GeV/c$ signal is spread over neighbouring rows however it also does not have a secondary band as previously. Such a 2-row effect was not observed at other angle settings. The lowest clean signal angle was found to be $\theta_p = 6°$ and the results are shown in Figure 4.22.

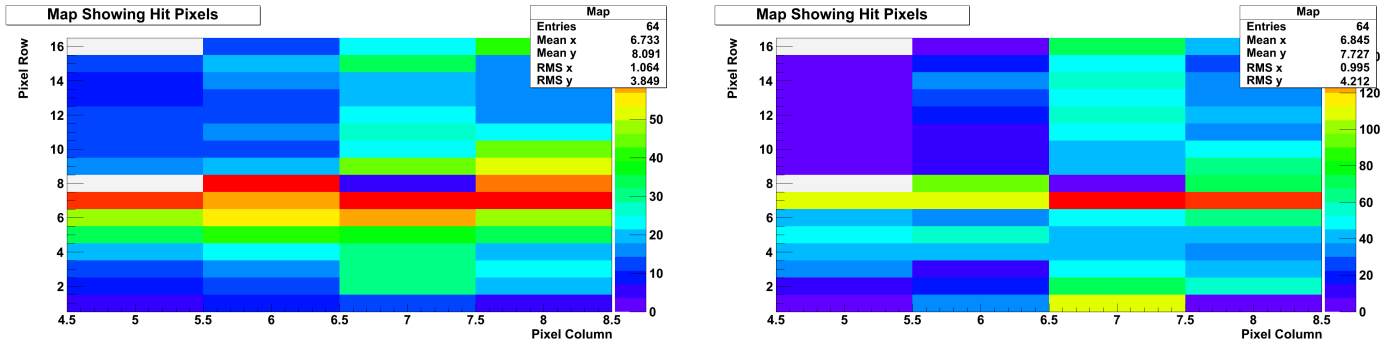

(a) (b)

Figure 4.22: A comparison of the data taken at beam momentum $4\,GeV/c$, a), and $10\,GeV/c$, b), with a polar angle of $\theta_p = 6°$.

Again the $10\,GeV/c$ results show a clean peak centred on row 5 and the $4\,GeV/c$ shows a signal split near evenly over rows 4 and 5. This pattern is repeated across the range $6° \leq \theta_p \leq 18°$, a slight difference is apparent between signals taken with at 4 and those taken at $10\,GeV/c$. For $\theta_p < 6°$ we see less predictable and less clear cut signal detection. Shown in Figure 4.23 is the data taken with a beam momentum of $10\,GeV/c$ at $\theta_p = 5°, 5.5°$.

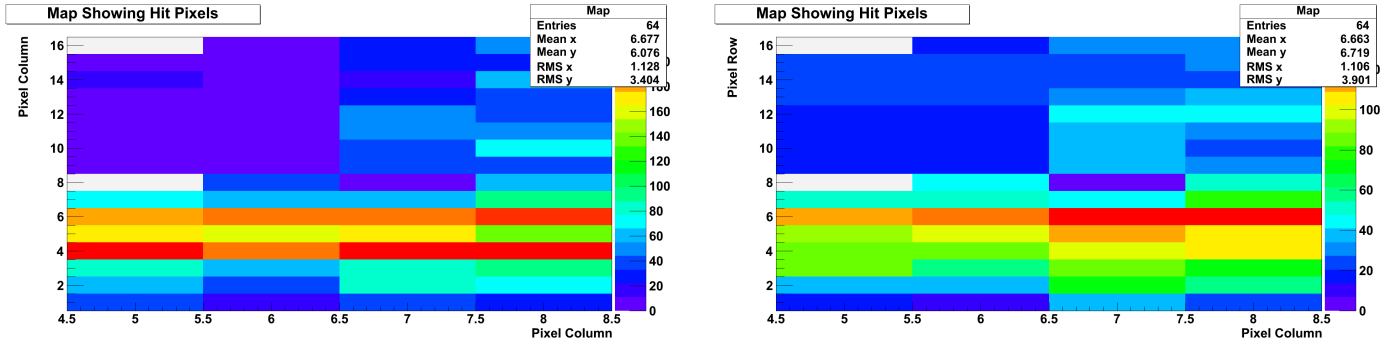

(a) (b)

Figure 4.23: The observed data taken with $10\,GeV/c$ beam at $\theta_p = 5.5°$, a), and at $\theta_p = 5°$, b). In both a strong signal can be seen to be spread across a larger area of the PMT surface than for $\theta_p \geq 6°$.

A clear secondary peak is visible for the data at $\theta_p = 5.5°$ and at $\theta_p = 5°$ the distribution is spread over the lower pixel rows with a peak in common with $\theta_p = 5.5°$. This data presents the lowest angle that will be present in the final FLDD. Lesser θ_p were planned to investigate offset between beam direction and measured θ_p but this was extended to investigate the unexpected spread behaviour shown in Figured 4.23. The data at perpendicular incidence and and at $\theta_p = 1.5°$ are shown in Figure 4.23.

The signals at $\theta_p = 0°$ and $1.5°$ can be seen to be spread across the whole PMT surface, with only small peaks visible. At perpendicular incidence the core constituent of the light is spread near evenly over Rows 2-5 and at $1.5°$ a slight peak at Row 3 is offset by a high mean signal across the PMT. As the peak row $\to 1$ as $\theta_p \to 0°$, the Focussing Lightguide (FLG) tries to reflect light below the bottom edge of the focussing surface. When this occurs the light is focused onto the inactive bottom side and subsequently reflected on

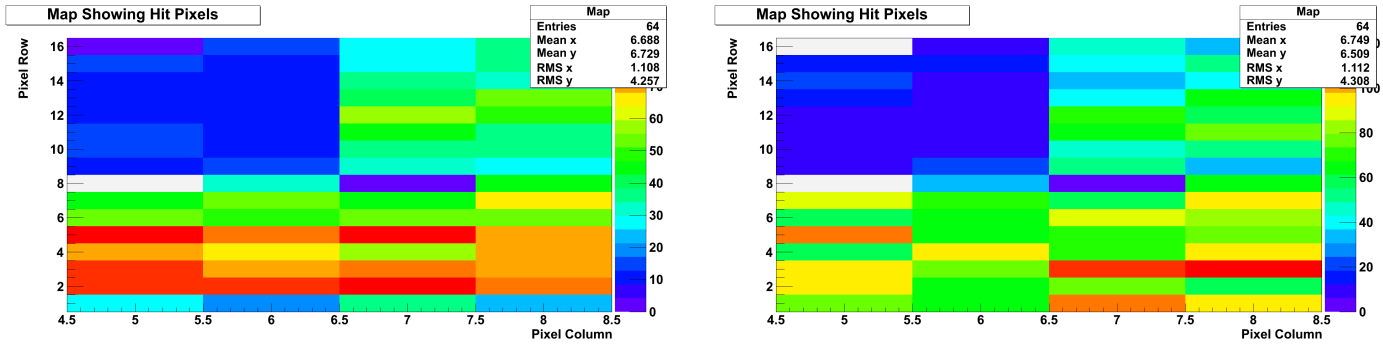

(a) (b)

Figure 4.24: The observed data taken with $10\,GeV/c$ beam at $\theta_p = 0°$, a), and at $\theta_p = 1.5°$, b).

to the PMT. Further studies were carried out to discern to what extent this effect explains the behaviour observed.

4.3 Simulation & Analysis

A number of clear features are present in the results, Section 4.2.5, that differ from the the ideal of a single-peaked signal. If these features were present in the combined data for a given setting they were also present in each contributing run to that setting. This would imply that effects over time or Data runs being systematically misaligned from those at the same setting were not responsible.

The experimental set-up was therefore simulated using the Zemax optical simulation system to ascertain if these features were inherent in the design of the Advanced Prototype as used at the CERN T9 Beam time.

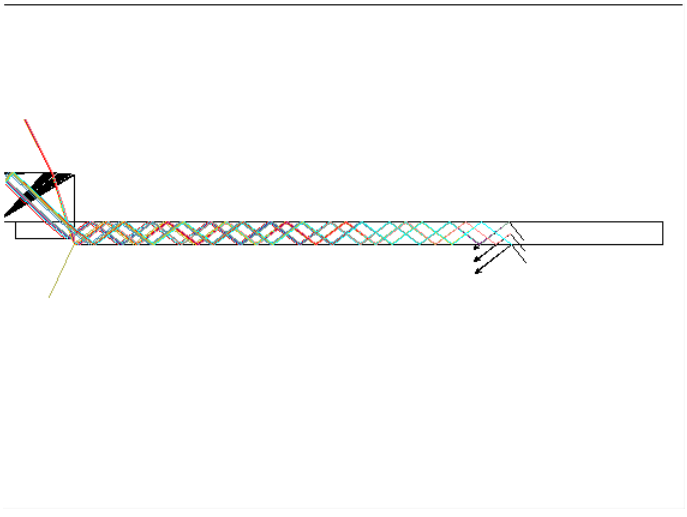

Figure 4.25: A cross-section of the radiator bar and the corrective LiF element.

Zemax is a proprietary ray-tracing-based lens design and optimisation software package published by Radiant Zemax. It enables the user to define objects and prescribe the objects with given material properties, either pre-defined or user entered. Simple geometries such as those for the radiator bar and Lithium Fluoride

element are easily defined within Zemax and are shown combined in Figure 4.25.

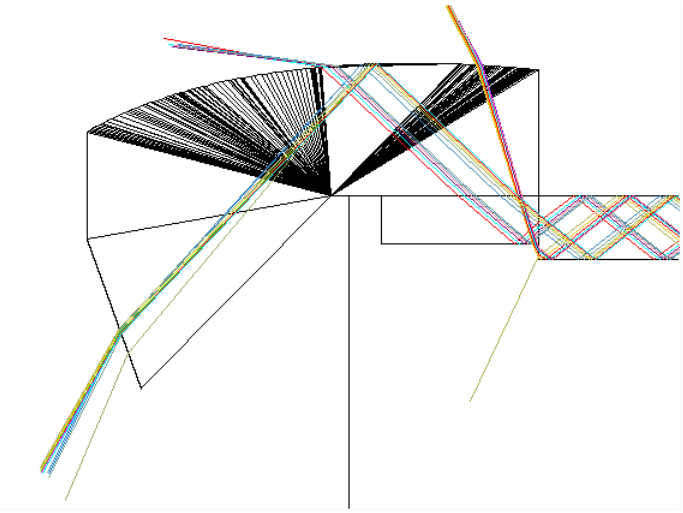

Figure 4.26: The Focussing Lightguide simulated with rays of Čerenkov light. The mismatch of $0.5\,mm$ between radiator and LiF thickness is clearly visible.

It is non-trivial to define the Focussing Lightguide (FLG) shape with the pre-defined geometries Zemax provides. It does, however, allow the user to import an object in the form of common Computer Aided Design file types, such a STEP files. This imported object, although possibly displayed less clearly than predefined objects, can be prescribed in a similar fashion to the predefined objects.

Source rays were then defined at angles corresponding to $\beta = 1$ particles incident upon the detector as described in Section 4.1. The angle and origin position of these rays were then rotated and moved to account for each of the settings shown in Section 4.2.5.

The first question the simulation was able to answer was that of systematic offset within the Advanced Prototype. This was caused as the precise alignment of the beam and detector was not known during the beam, the best constraint on the beam being the geometric acceptance of the ToF1, Fast and ToF2 scintillators. By looking for clearly identifiable features which are unique to a single Data setting and comparing to their occurrence to the setting at which they occur within the simulation allows for a best estimate of systematic angular offset. Figure 4.27 shows this for the data taken at $\theta_p = 6°$ with a beam momentum of $p = 10\,GeV/c$ and the simulation at the same setting.

The simulated data splits the PMT surface dimensions into 128 rows and 4 columns for greater resolution compared to the 16 rows of the H9500. The peak in the Observed data, Figure 4.27(b), is on Row 5 of 16, or $31.25 \pm 3.13\%$ up the surface from the bottom row. The peak in the Simulated data, Figure 4.27(a), is situated at row 40 of 128 or $31.25 \pm 0.39\%$ up the surface from the bottom row. The same comparison was carried out at $\theta_p = 10°$.

The peak in the Observed data falls on Row 7 of 16, $43.75 \pm 3.13\%$ up the PMT from the bottom, and the peak in the Simulated data is at Row 59 of 128, $45.31 \pm 0.39\%$ of the way up, again indicating agreement in alignment. The Observed data thus shows movement of $3.125 \pm 1.105\%$ of the surface per degree in Polar angle while the Simulated data shows movement of $3.71 \pm 0.14\%$ of the surface per degree, again within

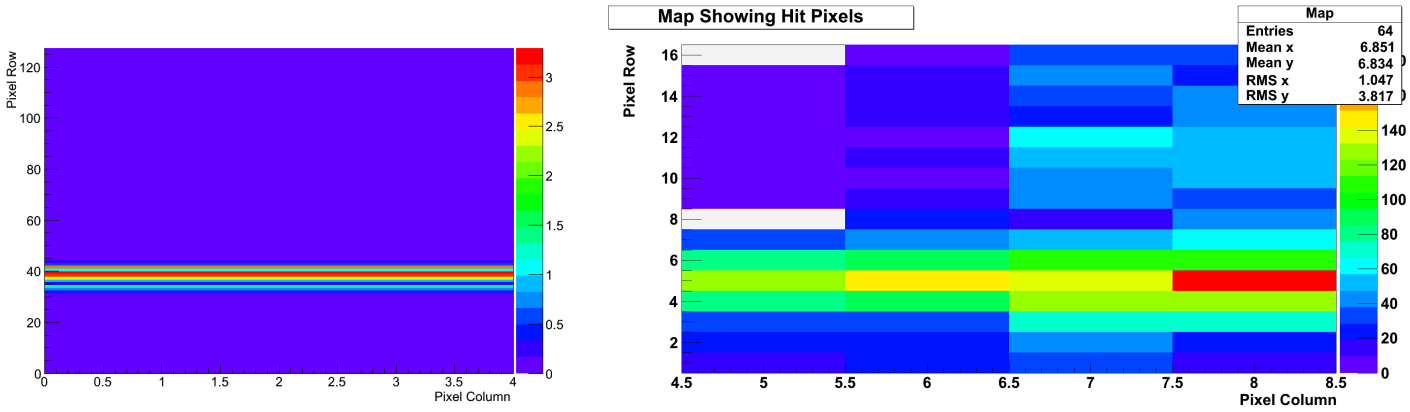

(a) (b)

Figure 4.27: Comparison between Simulated, a), and Observed, b), data for $\theta_p = 6°$. The Simulated data splits the PMT surface into 128 pixels for greater resolution.

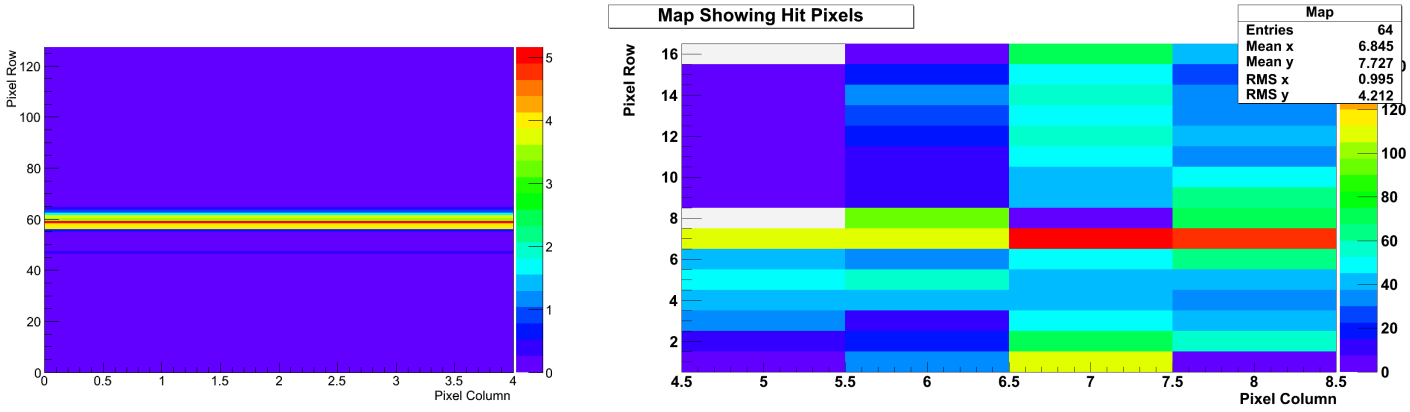

(a) (b)

Figure 4.28: Comparison between Simulated, a), and Observed, b), data for $\theta_p = 10°$.

agreement.

Observed in Figures 4.23 and 4.24 is a degradation of signal quality below $\theta_p = 6°$. The Observed data was taken in 0.5° intervals and the Simulated data taken at 0.25° intervals. The data were compared at 5.5°, Figure 4.29.

Both the Observed data, Figure 4.29(b), and the Simulated data, Figure 4.29(a), show signal splitting replacing the clear peaks, though the observed data shows a more extreme effect. As the simulation closely echos observation at previously tested settings it was used to restrict the angle range in which the splitting first occurs. As can be seen in Figure 4.30 the splitting is not present to the same extent at $\theta_p = 5.75°$.

A comparison for perpendicular incidence begins to highlight the limitations of the produced lightguide prototype, Figure 4.31. The Simulated data shows a clear spread across the lower section of the PMT however not to the same extent as the Observed data, which is spread over the whole PMT surface. It is important to note that the Simulated data retains a peak, albeit with a lower absolute value, at Row 1. This contrasts with the Observed data which shows no single peak and a large spread, covering 1/4 of the PMT

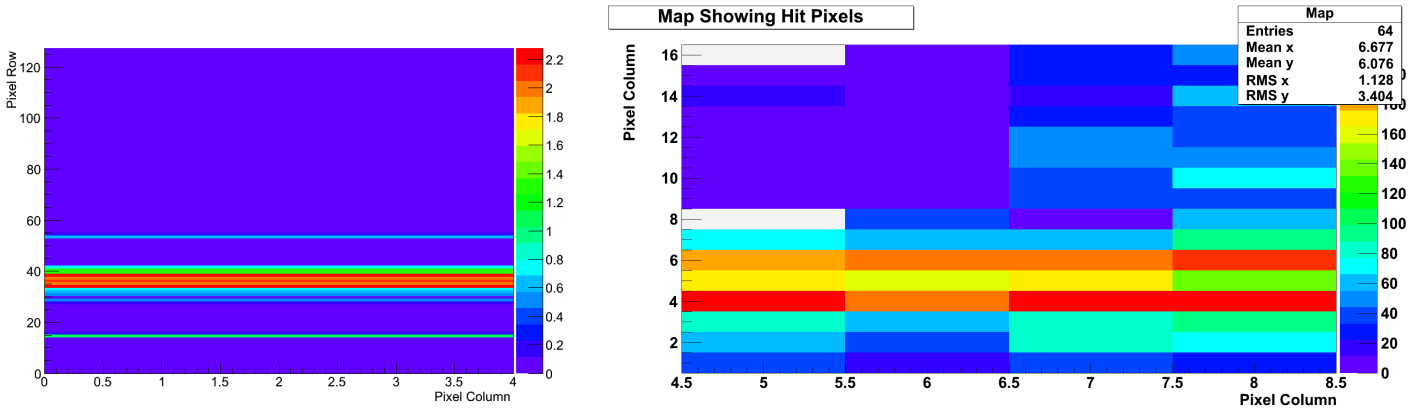

(a) (b)

Figure 4.29: Comparison between Simulated, a), and Observed, b), data for $\theta_p = 5.5°$.

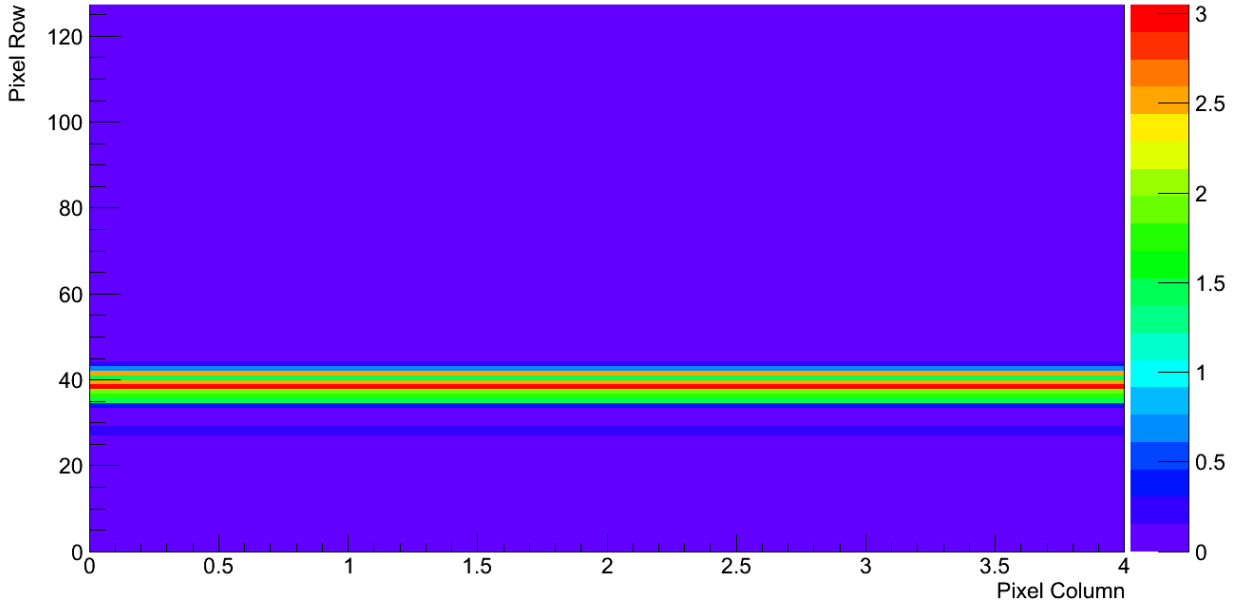

Figure 4.30: The Simulated data for $\theta_p = 5.75°$. The splitting effect visible in Figure 4.29 is not present in this data.

surface.

The last comparison is drawn between the data at $\theta_p = 1.5°$. The Observed data, Figure 4.32(b), shows the entire surface of the PMT having elevated signal levels with a small peak region along Row 3, especially in columns 7 and 8. The Simulated data, Figure 4.32(a), shows a series of strips but, as in Figure 4.31(a), a peak remains. This peak is clearly below the area of the PMT surface that is occupied by Row 3 in common with the perpendicular case.

The lower bound for FLG focussing arises from a the Čerenkov cone produced by a particle incident at $\theta_p = 5°$ and the Total Internal Reflection condition fulfilled. The critical angle for fused silica is $\theta_{crit} \approx 41°$ and the Čerenkov angle for $\beta = 1$ is $\theta_c \approx 49°$. Therefore a $\beta \approx 1$ particle incident upon the radiator in

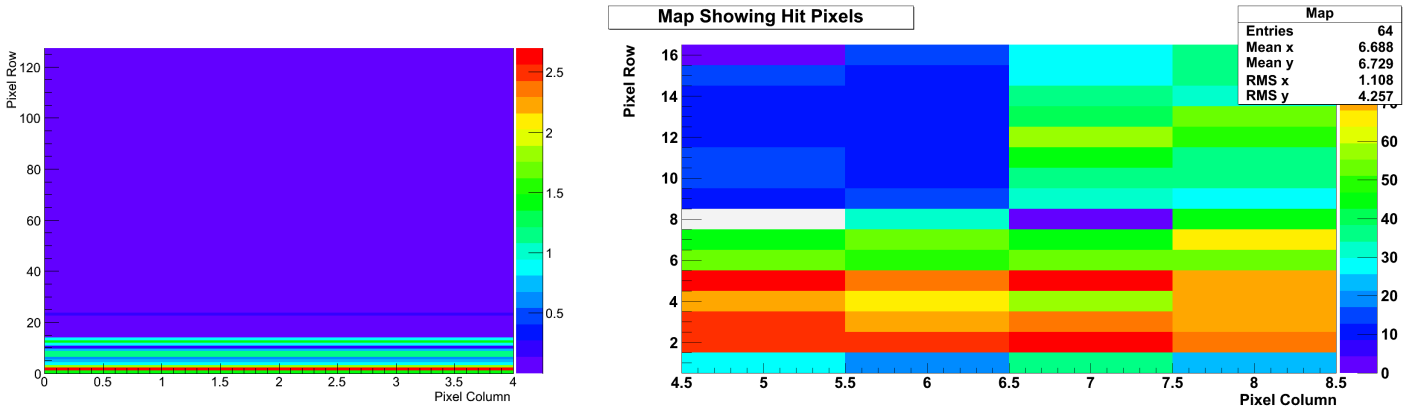

(a) (b)

Figure 4.31: Comparison between Simulated, a), and Observed, b), data for $\theta_p = 0°$.

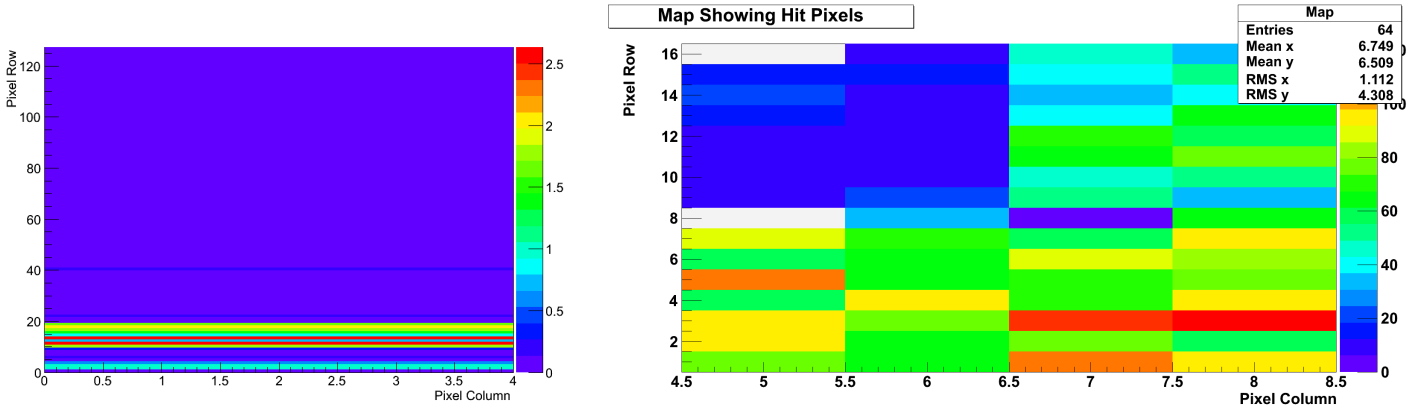

(a) (b)

Figure 4.32: Comparison between Simulated, a), and Observed, b), data for $\theta_p = 1.5°$.

the Advanced Prototype will produce light within the operating range of the FLG well below $\theta_p = 5°$. This would be true of a lightguide constructed of fused silica, and is not a concern for the final FLDD as the beampipe cut-away ensures no particles will strike the radiator at $\theta_p < 5°$.

The most simplistic explanation of both signal splitting and the discrepancies between observed and simulated data is that the issues with the production of the FLG detrimentally affect performance. The focussing surface was designed to translate the angle range found at the entrance to a fused silica lightguide. A PMMA version will required a different focussing surface to both cover the angles present before focussing and also utilise the full PMT surface. The resulting deviation of light onto the support walls on the side and bottom of the FLG cause "splash back" which strikes the the PMT surface.

As Zemax had recreated the features of the observed data accurately it was used to postulate the performance of a FLG constructed from Suprasil as designed. First the clean signal settings from Figures 4.27 and 4.28 were tested using the Suprasil lightguide and they show clean peaks with very little splitting, as for the PMMA case, Figure 4.34.

To check the performance of a Suprasil FLG the setting was also tested at $\theta_p = 5°$, Figure 4.35. This is

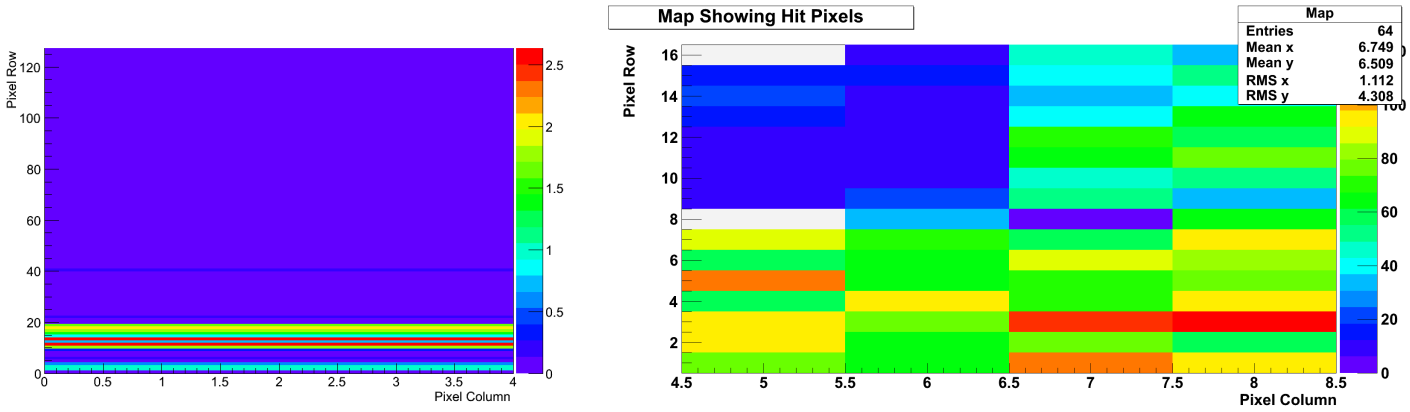

(a) (b)

Figure 4.33: Comparison between Simulated, a), and Observed, b), data for $\theta_p = 1.5°$.

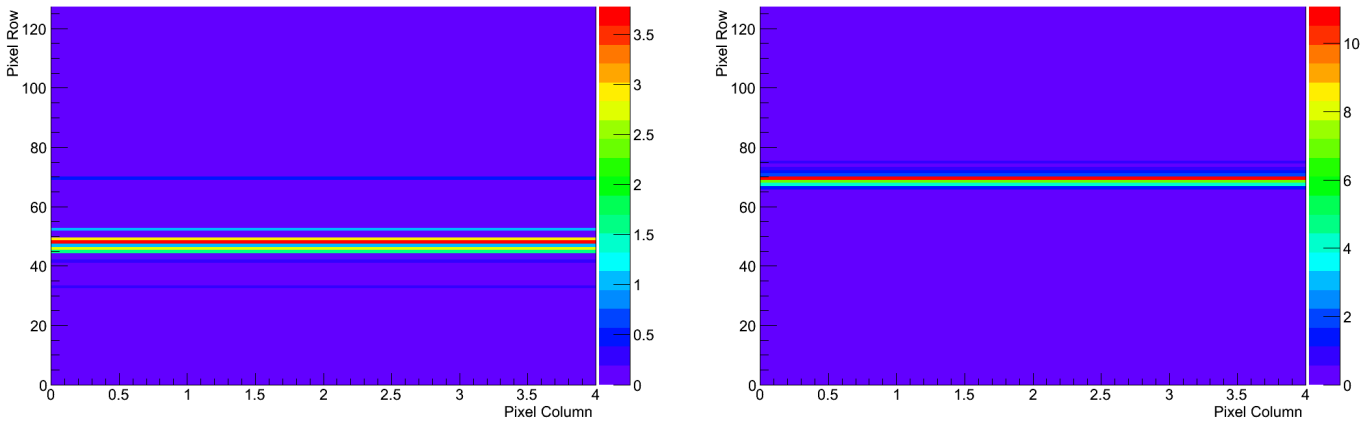

(a) (b)

Figure 4.34: Simulated data with a Suprasil lightguide for $\theta_p = 6°$, a), and 10°, b).

the minimum polar angle present in the final FLDD design and also the angle at which higher momentum particles are more likely to be found. The splitting effect that was present in the PMMA lightguide remains when the material is changed.

As the splitting effect was present within the expected range of angles in the final FLDD and with a Suprasil lightguide a second mechanism for production was postulated: The presence of photons propagating with a wide range of azimuthal angles in the same lightguide causes additional angles to be present. As the simulation was carried out with discrete azimuthal angle bands there are discrete bands present upon the detector. Within the observed data the azimuthal component forms a continuum of equal probability and so signal is spread over a great section of the surface. To test this a set-up with perpendicular incidence was Simulated, as this would be outwith the angle range for which the FLDD is designed, Figure 4.36.

The Simulated data with no azimuthal component, Figure 4.36(a) shows no signal, with bands of minimum intensity residual from the plotting algorithm. However the data with 15° azimuthal components shows an obvious signal. To investigate this further the Simulation was also carried out for azimuthal angles of 5° and

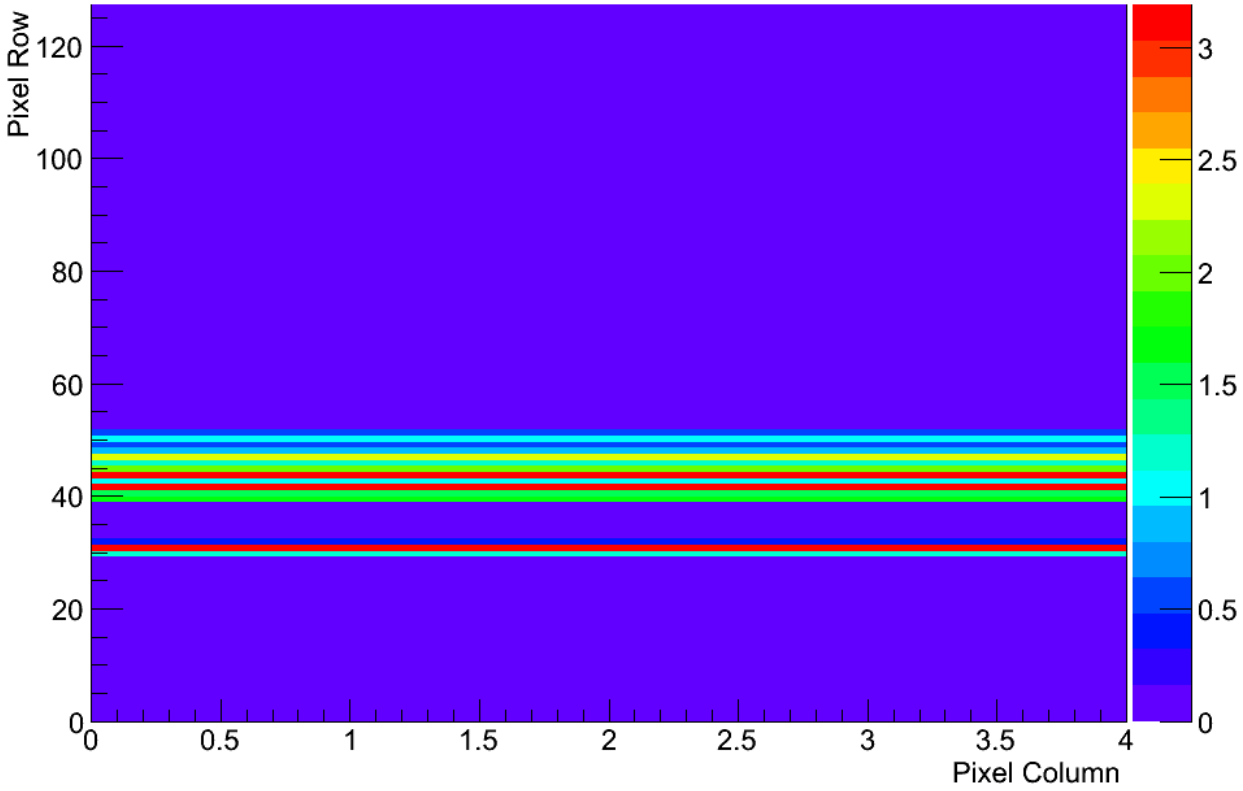

Figure 4.35: Simulated data with a Suprasil lightguide at $\theta_p = 5°$.

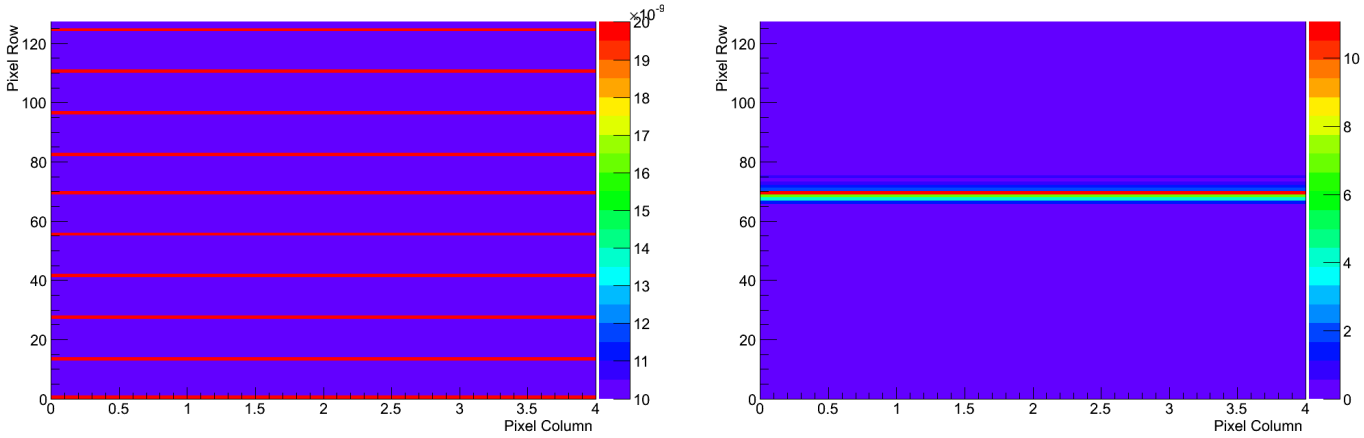

(a) (b)

Figure 4.36: Simulated data with a Suprasil lightguide for $\theta_p = 0°$ and photons with no azimuthal component, a), and with the 15° azimuthal component, b).

10°, Figure 4.37.

As for the case with no azimuthal component there is no signal present on the PMT surface as a result of photons emitted due to a $\beta = 1$ particle perpendicularly incident upon the radiator. It is clear that the

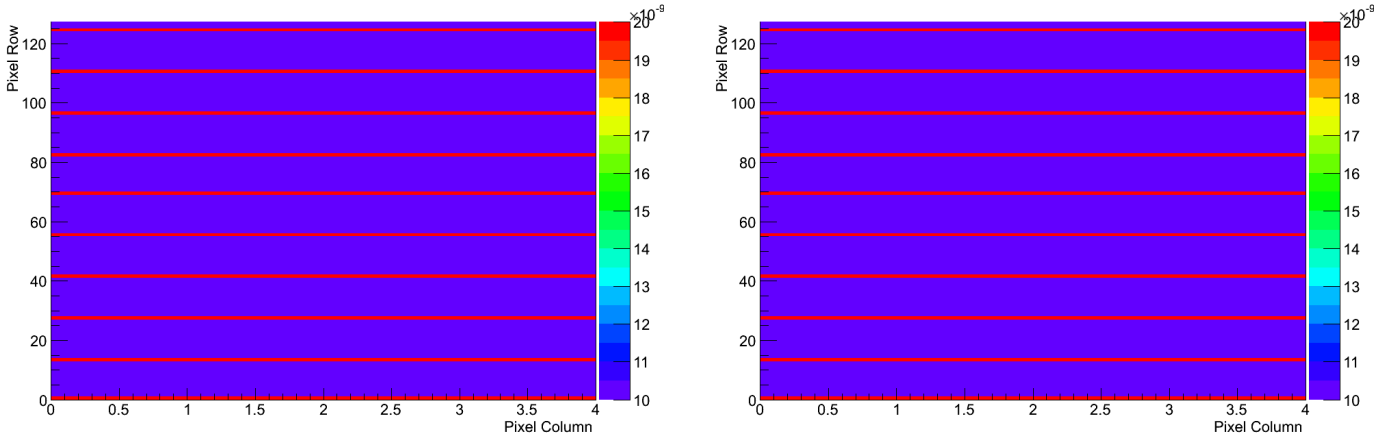

(a) (b)

Figure 4.37: Simulated data with a Suprasil lightguide for $\theta_p = 0°$ and photons with with a 5° azimuthal component, a), and a 10° component, b).

observed data in Figure 4.36(b) is directly resulting from the azimuthal component. The circumstances under which this will occur will be present in the final FLDD will be for particles incident within the 93.30 mm of the rim. As Čerenkov photons are emitted with equal probability around the cone, such azimuthal conditions will be present irrespective of initial particle momentum.

The path taken by light within the Advanced Prototype set-up is shown in Figure 4.38. It is clear that the case of no azimuthal component shows no light passing beyond the focussing surface of the FLG, Figure 4.38(a), but light makes it to the focal plane when a component of 15° is introduced, Figure 4.38(b).

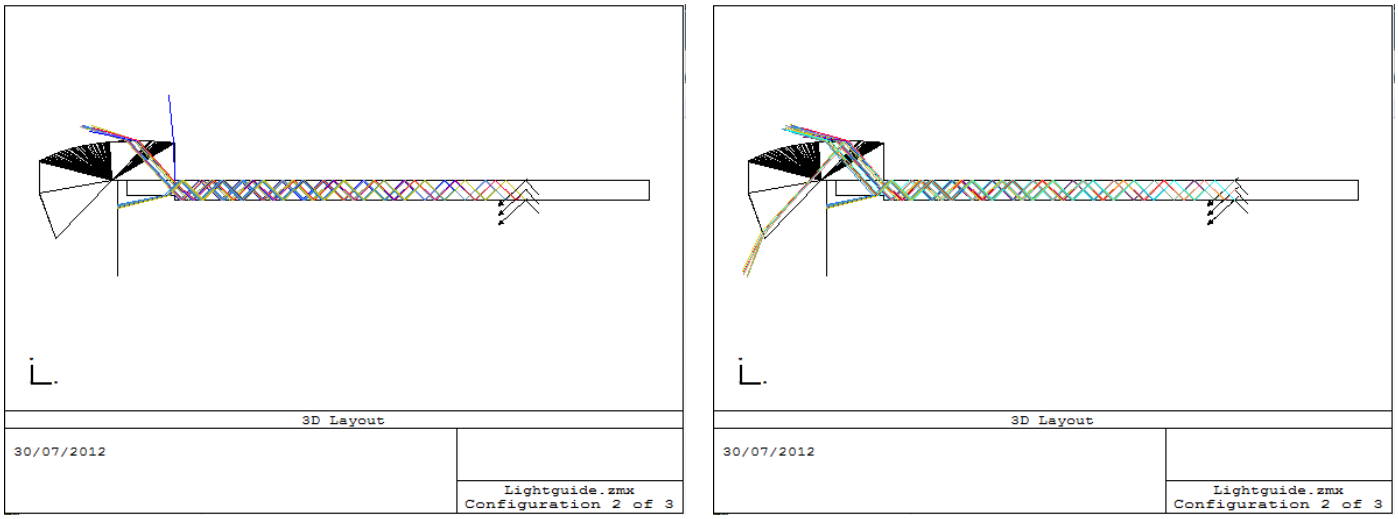

(a) (b)

Figure 4.38: Ray tracing diagrams for the full Advanced Prototype set-up within Zemax. The presence of light on the focal plane is clear in the $\phi \leq 15^{circ}$ case, b), but not present at all in the non-azimuthal case, a).

As the photon propagation vector changes with the addition of azimuthal components, so does the projection

of the vector along the optical axis for which the FLG is designed. The resulting focussing is therefore altered as the azimuthal angle changes. If the photons enter the lightguide with similar azimuthal trajectory components they will be focused onto the same section of the PMT surface and the effect will result in an offset from the position expected for a give θ_c. Knowledge of the photon impact position of a given event allows for this offset to be accounted for. This does not solve the issue when a wide range of azimuthal angles are present in the same lightguide.

This could achieved either through a complete redesign of the FLG component itself, sacrificing radial precision for increase stability to non-radial photons. Such an optimisation would present significant challenges, ostensibly in the definition of a suitable function of merit to be minimised or maximised. Any design would also have to be subject to production capabilities, limiting the options for such an optimisation.

An alternative solution would be to eliminate reflections from the sides of the FLG, thereby stopping the non-radial photons from reaching the photon detector. Such a solution would eliminate any photons which strike the side walls indiscriminately, thus eliminating all photons entering off-radial lightguides and severely curtailing the ability of the FLDD to sample the Čerenkov cone projection.

Another second alternative is to eliminate discreet LiF and FLG components and to replace them with 128 "keystone" or wedge-shaped replacements. This eliminates all side walls in favour of a toroidal solution. This solution would, like the discreet FLG solution above, be of high technical difficulty and require extensive study for optimisation.

The performance of the Advanced prototype set-up for Pion/Kaon separation given particles with $\theta_p = 5°$ and $p = 4.5\,GeV/c$, assuming the removal of azimuthal uncertainty, is given in Figure 4.39. The resolution required to separate these two particles, which are at the upper momentum limit for the FLDD, is $1/64$ th of the surface of the $51 \times 51\,mm^2$ PMT surface. It is currently envisaged to use a 32 Row PMT, implying that either a further element to the FLG redesign or a PMT with a 64×64 anode matrix is required.

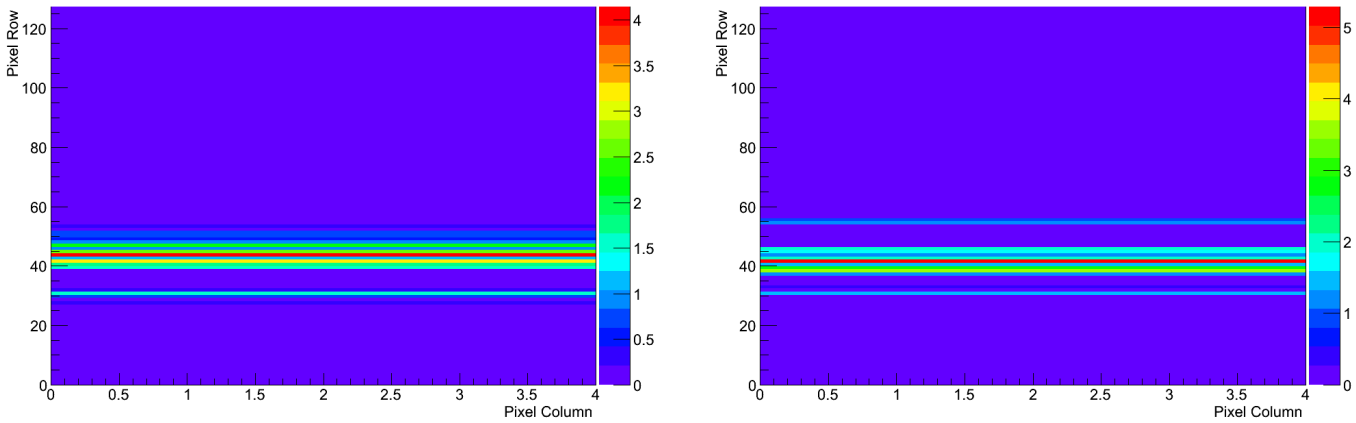

(a) (b)

Figure 4.39: Simulated PMT response for Pions, a), and Kaons, b), incident at $\theta_p = 5°$ and with $p = 4.5\,GeV/c$.

This does not detract, however, from the success of the Advanced Prototype test campaign. By showing a strong correlation between the Simulation and Data from the T9 test beam time it is clear that the assembly of the prototype and small systematic offsets within the experimental execution were not crucial to the detector performance. Such an outcome should extrapolate to the final FLDD and shift the burden of difficulty with its design to that of the FLG design itself.

It would be beneficial for the FLG to be "over-engineered", such that there is room on the focal plane for angles outside those predicted by the absolute dynamic range required of the detector. This should be done for angles both above and below the maximum and minimum of those within the dynamic range. This will ensure that all angles within the dynamic range of the detector can be focused, and no information is lost, allowing for small systematic alignment miscalculations within the assembly of the FLDD.

The drop in absolute resolution resulting from such a solution, in favour of robustness, can be partially overcome by studying the efficiency of each of the PMTs to be used. This then allows the response of each of the PMTs to be fitted and this fitting to weighting to improve the resolution potentially beyond that of the simple conformal mapping. This technique can also be used for a perfectly aligned and optimised solution to further improve the FLDD detection efficiency.

Chapter 5

Summary & Conclusion

The refinement of theoretical predictions of the Strong nuclear force and the fundamental particles which experience it is a very active area of modern physics research. Particles comprising a quark-antiquark pair of the same flavour are the simplest possible hadronic systems. Amongst these the heavy quarkonia, comprising Charm-antiCharm or Bottom-antiBottom pairs, offer states predicted to have narrower widths than those found with lower rest mass quarks. The increased mass also reduces the relativistic corrections required within theoretical predictions. As Charm quarks are the less massive than Bottom quarks they require less centre-of-mass energy at production. $\bar{\text{P}}$ANDA will study Charmonium in unprecedented detail.

The $\bar{\text{P}}$ANDA experiment will use the High Energy Storage Ring (HESR), a racetrack-type accelerator, at the FAIR facility at GSI to provide a beam of cooled antiprotons. The antiprotons will annihilate with a proton target housed within the $\bar{\text{P}}$ANDA detector. The detector is split into two section, a Target Spectrometer immediately surrounding the target, and a Forward Spectrometer to detector particles produced with large Lorentz boosts in the downstream direction of the beam.

Within the Target spectrometer 2 geometries are used to achieve full angular coverage: a barrel-type configuration in the central region and and endcap configuration. The PID for the target spectrometer will be performed by two Čerenkov detectors based on the Detection of Internally Reflected Čerenkov radiation (DRIC) principle. In the central region a barrel detector will be constructed, with the system being read out on the upstream side of the internal target. In the endcap a DRIC detector in a novel disc configuration is proposed.

The Focussing Lightuide Disc DIRC (FLDD) is one proposed design for the endcap disc DIRC, Figure 1.10. The disc will be approximated with a 128-sided polygon of fused silica which will lead to a unique hardware-based Chromatic Dispersion correction element constructed from Lithium Fluoride and then to a focussing lightguide (FLG) which maps the angle of propagation onto the surface of a position sensitive PMT. For such a novel system each section must be properly tested to ensure it performs as predicted and that the design is valid for performing to the requirements of the $\bar{\text{P}}$ANDA physics programme. As such a stepwise approach to prototype development was employed, starting with the testing of the Chromatic Dispersion correction element.

Chromatic dispersion is one of the largest contributions to the uncertainty in measured Čerenkov angle in

all DIRC detection systems. The dispersion arises at production of Čerenkov radiation as a result of the frequency dependence of the Refractive Index of the radiator material. The dispersion cannot be avoided and so must be mitigated through subsequent detector design. The FLDD proposes a cuboid block of Lithium Fluoride to achieve this mitigation. The verification of this effect is central to this thesis.

After testing the observed spread in photon propagation angle within the FLDD design was compared to the predicted case, Table 5.1.

Table 5.1: The measured angles after being recorded on the CCD with geometric calculations included. All angles are measured with respect to the normal to the external surface of Block 2.

Material	Predicted $\Delta\theta_f$ (rad)	Measured $\Delta\theta_f$ (rad)
Fused Silica	$0.011155 \pm 3.146 \times 10^{-5}$	$0.0111 \pm 3.8 \times 10^{-4}$
Lithium Fluoride	$0.001761 \pm 4.024 \times 10^{-6}$	$0.0021 \pm 3.7 \times 10^{-4}$

Although subject to large uncertainties the observed data and predicted data are in agreement. As the observed data was taken using a system constructed of several sub-components it shows that the reduction in angular spread is robust to real world assembly tolerances. As the FLDD envisages 122 such LiF blocks this robustness is crucial to the success of the design.

The FLG element is designed on the principle of parallel-to-point optics, mapping photon propagation angle into a given point on the PMT surface, Figure 1.13. The position on the PMT surface is therefore a direct measure of the angle of propagation of the photon which struck it. The reduction in uncertainty on this angle σ_θ caused by Chromatic dispersion is therefore equivalent to the reduction in angular spread $\Delta\theta_f$. An improvement as shown in Table 5.1 will result in an improvement in σ_{θ_c}, the uncertainty on Čerenkov angle. Assuming an this uncertainty stems purely from Chromatic dispersion gives and uncertainty which varies with the number of independent photons observed during the reconstruction of θ_c as shown in Figure 2.9.

The final observed σ_{θ_c} will include a contribution from Multiple Scattering of $\sim 1.721 \times 10^{-3}\, rad$ which is of the order of that contributed by Chromatic Dispersion with a LiF corrective element. As such further improvement in the Chromatic Dispersion will have an increasingly limited effect without reducing multiple scattering, a factor inherent to the radiator material.

The performance of the LiF element justifies its inclusion in the design of the FLDD.

The second stage of the prototype development was to test the assumptions about photon production. A simple experiment counting the number of produced photons within a test bar of Suprasil 1, a fused silica radiator candidate material, was carried out. The Set-up consisted of the radiator bar, with reflection dampening on the sidewalls, and a 2-inch traditional photomultiplier tube. The set-up was rotated through a number of polar angle settings and the number of observed photons recorded, Figure 3.8.

The simulations of the set-up were carried out to investigate the impact of the reflection dampening on the observed photon yield. After fitting the resulting data it was possible to estimate the effective absorption factor of the sidewalls of the detector, Figure 3.15. The result was an effective absorption factor $\eta \approx 0.27$. This was significantly below the expected value and it was found to occur as a result of poor optical contact

between the foam rubber and the radiator bar.

The simulation accurately reproduced the observed geometric behaviour of the system however, and the remaining offsets were a result of systematic misalignment between the beam axis and the normal to the radiator bar surface, to losses sustained during coupling between PMT and the bar and to the reduced Quantum Efficiency of the PMT itself. The data show that the simulations of the system were an accurate representation of the performance of the Suprasil radiator.

The final stage of the prototype development was a combination of the radiator, LiF component, example FLG and a position sensitive PMT, Figure 4.1. The system was placed in a beam of mixed hadrons and rotated to cover the range of Polar angles covered in the final FLDD design. The movement of the signal over the surface of the PMT gives an indication to the performance of the FLG.

An optical ray-trace simulation of the set-up using the Zemax framework was constructed. All components were accurately modelled within this set-up and using the data extracted from previous experiments. The results of the simulated showed excellent agreement with the observed data, with both showing photons striking the same distance up the PMT surface for the same polar angle setting. This confirmed that the set-up was not significantly offset from the beam axis and also that the FLG performance could be accurately understood within the framework.

Peaks present at significantly different positions to one another were shown to result from the the photon angles being lower than the minimum for which the lightguide was designed and from the presence of a large variation in photon azimuthal angle within the same lightguide. The latter of these proves to be a major obstacle in design of the FLG component. As can be seen from Figure 5.1 the presence of azimuthal photons at certain polar angles can explain why signal was seen when it would be expected that all light escapes from the FLG focussing surface.

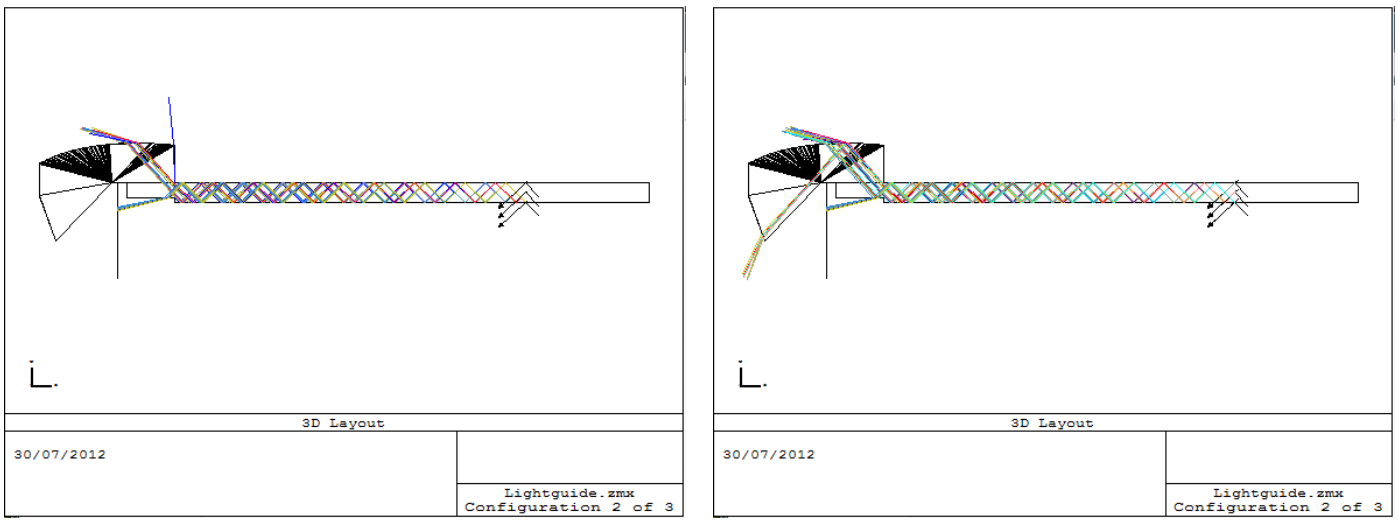

(a) (b)

Figure 5.1: Ray tracing diagrams for the full Advanced Prototype set-up within Zemax. The presence of light on the focal plane is clear in the $\phi \leq 15°$ case, b), but not present at all in the non-azimuthal case, a).

The design of the FLG component works well when the photons entering do not carry this azimuthal com-

ponent. This would be true of photons emitted from particles striking the disc at low polar angles. These particles are also most likely to have the highest momentum and so be the particles where successful positive PID is hardest. In the case of a purely radial photon set, the response on the PMT surface for a Pion and a Kaon both with $p = 4.5\,GeV/c$, is shown in Figure 5.2.

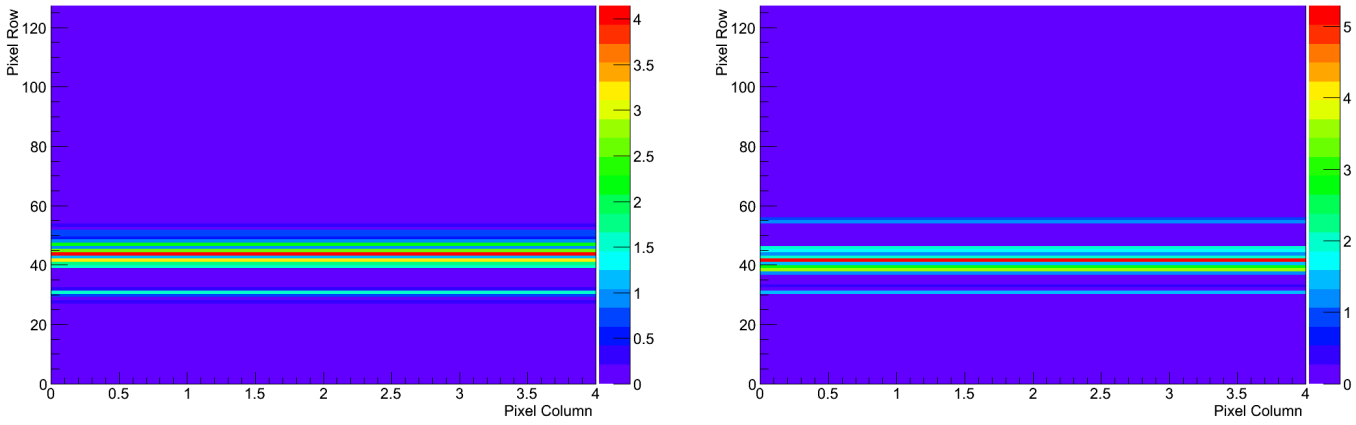

(a) (b)

Figure 5.2: Simulated PMT response for Pions, a), and Kaons, b), incident at $\theta_p = 5°$ and with $p = 4.5\,GeV/c$.

The signals are separated by 2 Channels of the 128 present within the simulation. The required pixel pitch is therefore $x = 0.79\,mm$ per pixel, or to split the $51\,mm$ surface into 64 channels. This is double the spatial resolution currently proposed. The presence of azimuthal photons will degrade the performance as they will produce signals from the same event as radial photons but in different positions. Such an effect will require to be minimised before any final FLDD design is approved.

This thesis has presented a systematic approach to prototype design and testing for the Focussing Lightguide Disc DIRC. Central to the performance of the FLDD is the novel hardware-based chromatic dispersion correction element. The experimental verification of the efficacy of Lithium Fluoride in combination with the fused silica to achieve a reduction in dispersion was the primary aim of this prototype development. The verification shown in Chapter 2 is the first time such a hardware based system has been demonstrated and represents a major success in the design of the FLDD.

The verification of the assumptions made on photon production and transport within the chosen radiator, Chapter 3, in combination with the confirmation of the performance of the LiF component allowed for the development of the Advanced Prototype, combining key elements of the FLDD in a single system. The study of the Advanced Prototype, Chapter 4, was accurately described in terms of its optical performance using the assumptions proven in this thesis. The accurate reproduction of observed effects by a simple optical model also further proved that the Lithium Fluoride component will satisfactorily reduce the Chromatic Dispersion present in the radiator. The results of this simulation also show that the design in its current form does not perform to the standard required for use in the $\bar{\text{P}}$ANDA endcap.

To design such a component requires a function which can map the position of photon emission from the

surface of the LiF block and the direction with which the photon propagates onto the a focal plane. It must do so in a way that the distance from the bottom of the focal plane reflects a change in photon propagation angle with reference to the surface of the radiator disc.

Two mutually exclusive systems may solve this. The first is to link the discrete lightguides and LiF blocks into toroidal sections and to then redesign the focussing surface in a way which allows for the fullest range of photon angles. Such a design would be difficult and must strike a compromise between perfect radial photons, which originate from the highest momentum particles, and the presence of a large azimuthal spread in photons from hits striking closer to the rim of the disc.

The second is to allow a second degree of freedom within the focussing surface. The current design is constant across the width of the lightguide allowing for radial focussing irrespective of the position with which the photon enters the LiF block, and hence lightguide. By allowing the height above the entrance window of the surface to vary not just along the length of the lightguide, but also over the width, the surface can address for the changes in azimuthal propagation. This design would compromise between azimuthal correction and allowing focussing for radial photons.

Any new lightguide designs will require to be utilised in similar development and testing process to that undertaken in this thesis before their efficacy can be understood.

In spite of the successes of the prototype development campaign for the Focussing Lightguide Disc DIRC it is therefore clear that extensive further study into the Focussing Lightguide element must be carried out before the FLDD performance reaches that required for use in the $\bar{\text{P}}$ANDA detector.

References

[1] The $\bar{\text{P}}$ANDA Collaboration, arXiv:0903.3905v1 (2009)

[2] J. -E. Augustin et al., Discovery of a Narrow Resonance in e^+e^- Annihilation Phys. Rev. Lett. 33, 1406 - 1408 (1974)

[3] J. Aubert et al, Experimental Observation of a Heavy Particle J Phys. Rev. Lett. 33, 1404-1406 (1974)

[4] K Nakamura, Phys. G: Nucl. Part. Phys. 37 075021 (2010)

[5] S. L. Glashow, J. Iliopoulos, and L. Maiani, Phys. Rev. D 2, 1285-1292 (1970)

[6] S Berko, and H N Pendleton, Annual Review of Nuclear and Particle Science Vol. 30: 543-581 (1980)

[7] K.K. Seth, The European Physical Journal A - Hadrons and Nuclei, 2003, Volume 18, Numbers 2-3, Pages 563-565

[8] M. Ablikim et al. BESIII Collaboration Phys. Rev. Lett. 104, 132002 (2010)

[9] J.L.Rosner et al., CLEO Collaboration Phys. Rev. Lett. 95, 102003 (2005)

[10] S. Uehara et al., BELLE Collaboration Phys. Rev. Lett. 96, 082003 (2005)

[11] S. U. Chung et al., Phys. Rev. D 65, 072001 (2002)

[12] E. I. Ivanov et al., Phys. Rev. Lett. 86, 3977 (2001)

[13] J. Kuhn et al., Phys. Lett. B595, 109 (2004)

[14] M. Lu et al., Phys. Rev. Lett. 94, 032002 (2005)

[15] A. Abele et al., Phys. Lett. B423, 175 (1998)

[16] J. Reinnarth, Nucl. Phys. A692, 268c (2001)

[17] A. Abele et al., Phys. Lett. B446, 349 (1999)

[18] S. U. Chung and E. Klempt, Phys. Lett. B563, 83 (2003)

[19] K. Juge, J. Kuti, and C. Morningstar, Phys. Rev. Lett. 90, 161601 (2003)

[20] C. Bernard et al., Phys. Rev. D56, 7039 (1997)

[21] C. Bernard et al., Nucl. Phys. (Proc. Suppl.) B73, 264 (1999)

[22] K. Juge, J. Kuti, and C. Morningstar, Phys. Rev. Lett. 82, 4400 (1999)

[23] Z.-H. Mei and X.-Q. Luo, Int. J. Mod. Phys. A18, 5713 (2003), hep-lat/0206012

[24] C. Morningstar and M. Peardon, Phys. Rev. D60, 34509 (1999)

[25] A. Bertin et al., Phys. Lett. B361, 187 (1995).

[26] A. Bertin et al., Phys. Lett. B385, 493 (1996)

[27] A. Bertin et al., Phys. Lett. B400, 226 (1997)

[28] C. Cicalo et al., Phys. Lett. B462, 453 (1999).

[29] F. Nichitiu et al., Phys. Lett. B545, 261 (2002)

[30] R. Maier for the HESR Consortium, Proceedings of the 2011 Particle Accelerator Conference (2011)

[31] The $\bar{\text{P}}$ANDA Collaboration, *Technical Design Report for the PANDA Target*
Internal Publication (2012)

[32] The $\bar{\text{P}}$ANDA Collaboration, *Technical Design Report for the: PANDA Micro Vertex Detector*
arXiv:1207.6581v1 (2012)

[33] The $\bar{\text{P}}$ANDA Collaboration, *Technical Design Report for the: PANDA Straw Tube Tracker*
arXiv:1205.5441v2 (2012)

[34] The $\bar{\text{P}}$ANDA TPC-GEM Collaboration, *Technical Design Study for the PANDA Time Projection Chamber*
arXiv:1207.0013v1 (2012)

[35] The $\bar{\text{P}}$ANDA Collaboration, *Technical Design Report for the PANDA Solenoid and Dipole Spectrometer Magnets*
arXiv:0907.0169v1 (2009)

[36] The $\bar{\text{P}}$ANDA Collaboration, *Technical Design Report for PANDA Electromagnetic Calorimeter (EMC)*
arXiv:0810.1216v1 (2008)

[37] The $\bar{\text{P}}$ANDA Collaboration, *Technical Design Report for: PANDA Forward Spectrometer Calorimeter (FSC)*
Internal Publication (2012)

[38] The $\bar{\text{P}}$ANDA Collaboration, *Technical Design Report for: PANDA Muon Detector system.*
Internal Publication (2012)

[39] P.A.Čerenkov, Phys. Rev. 52, 378-379 (1937)

[40] P. Glässel, Nuclear Instruments and Methods in Physics Research A 433 17-23 (1999)

[41] J. Seguinot, T. Ypsilantis, Nucl. Instr. and Meth. 142 377 (1977)

[42] David W.G.S. Leith, Nuclear Instruments and Methods in Physics Research A 494 389-401 (2002)

[43] K. Föhl, Nuclear Instruments and Methods in Physics Research A 639 311-314 (2011)

[44] M.J. Charles, R. Forty, Nuclear Instruments and Methods in Physics Research A 639 173-176 (2011)

[45] Peter Schönmeier et al., Nuclear Instruments and Methods in Physics Research A 595 108-111 (2008)

[46] E.N.Cowie et al., Nuclear Instruments and Methods in Physics Research A 639 181-184 (2011)

[47] The BaBar Collaboration, Nuclear Instruments and Methods in Physics Research A 538 281-357 (2005)

[48] M.Hoek at al, Nuclear Instruments and Methods in Physics Research A 595 190-193 (2008)

[49] A. Lehmman et al., Nuclear Instruments and Methods in Physics Research A 639 144-147 (2011)

[50] Pellin, Ph. and Broca, André, Astrophysical Journal 10 337 (1899)

[51] Philip E. Ciddor, Applied Optics, Vol. 35, Issue 9, pp. 1566-1573 (1996)